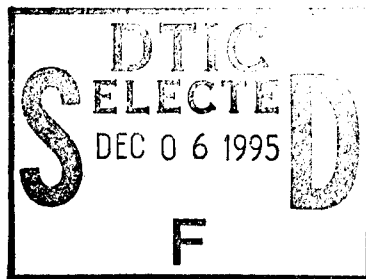


AFIT/GAE/ENY/95D-13



MACH 2.9 INVESTIGATION INTO THE FLOW  
STRUCTURE IN THE VICINITY OF  
A WRAP-AROUND FIN

THESIS

Richard Edwin Huffman, Jr.  
Second Lieutenant, USAF

AFIT/GAE/ENY/95D-13

19951201 006

DTIC QUALITY INSPECTED 8

Approved for public release; distribution unlimited

The views expressed in this thesis are those of the author and do not reflect the official policy or position of the Department of Defense or the U. S. Government.

AFIT/GAE/ENY/95D-13

MACH 2.9 INVESTIGATION INTO THE FLOW  
STRUCTURE IN THE VICINITY OF  
A WRAP-AROUND FIN

THESIS

Presented to the Faculty of the Graduate School of Engineering  
of the Air Force Institute of Technology  
Air University  
In Partial Fulfillment of the  
Requirements for the Degree of  
Master of Science in Aeronautical Engineering

Richard Edwin Huffman, Jr., BSAAE  
Second Lieutenant, USAF

December, 1995

Approved for public release; distribution unlimited

### *Acknowledgements*

I would like to thank my mentor and advisor, Maj Tom Buter. His perspective and encouragement added a great deal. I am forever indebted. Thanks go to Maj Buter's partner and my co-advisor, Dr Rodney Bowersox. His wealth of experience in hot-wire testing was invaluable. I also wish to thank Mr Carl Tilmann, a fellow student, whom was always willing to give me a hand. Additionally, I thank Mr Greg Abate of Wright Laboratories Armament Directorate for providing the resources to produce this work.

Any school doing quality experimental work owes gratitude to its technical support staff. In particular, I would like to thank Mr Jay Anderson and Mr Andy Pitts. Their experience and ability to "get it done right" was truly Sierra Hotel. At the AFIT model shop, Mr Tim Hancock deserves all the credit for construction. I gave him a sheet of doodles - and he built a polished model. His work will be truly missed at AFIT. Additionally, Mrs Kris Larsen, Mr Tony Schooler and Mr Tim Fox, who provided the computer support, deserve thanks for putting up with my endless requests to restore the data I had accidentally deleted.

And to my wife of a year and eight months, to whom I owe all of my inspiration. Her love and patience gave me a light at the end of the tunnel.

Accession For	
NTIS CRA&I	<input checked="" type="checkbox"/>
DTIC TAB	<input type="checkbox"/>
Unannounced	<input type="checkbox"/>
Justification .....	
By .....	
Distribution /	
Availability Codes	
Dist	Avail and/or Special
A-1	

Richard Edwin Huffman, Jr.

## *Table of Contents*

	Page
Acknowledgements . . . . .	ii
List of Figures . . . . .	vi
List of Tables . . . . .	ix
List of Symbols . . . . .	x
Abstract . . . . .	xii
I. Introduction . . . . .	1-1
1.1 Problem Statement . . . . .	1-1
1.2 Background . . . . .	1-3
1.3 Objectives . . . . .	1-5
1.4 Outline . . . . .	1-5
II. Experimental Apparatus and Methodology . . . . .	2-1
2.1 Mach 2.9 Facility . . . . .	2-1
2.2 Wrap-Around Fin Model . . . . .	2-7
2.3 Flow Visualization . . . . .	2-10
2.4 Pressure and Temperature Measurements . . . . .	2-13
2.5 Hot-Film Anemometry . . . . .	2-13
2.6 Data Acquisition . . . . .	2-16
III. Data Reduction . . . . .	3-1
3.1 Data Sample Reduction . . . . .	3-2
3.2 Pressure Probes . . . . .	3-3

	Page
3.3 Hot-Film Probes . . . . .	3-3
3.3.1 Calibration . . . . .	3-5
3.3.2 General Theory . . . . .	3-6
3.3.3 Coordinate Transformation . . . . .	3-7
3.3.4 Single Overheat Analysis . . . . .	3-9
3.3.5 Separation of Turbulence Variables . . . . .	3-12
IV. Results and Discussion . . . . .	4-1
4.1 Inlet Plane . . . . .	4-1
4.2 Blending Region . . . . .	4-5
4.3 Wrap-Around Fin Region . . . . .	4-7
4.3.1 Fin-Body Juncture . . . . .	4-9
4.3.2 Bow Shock Region . . . . .	4-10
4.3.3 Tip Region . . . . .	4-20
4.4 Turbulence Measurements . . . . .	4-20
V. Conclusions and Recommendations . . . . .	5-1
5.1 Conclusions . . . . .	5-1
5.2 Recommendations . . . . .	5-2
Appendix A. Error Analysis . . . . .	A-1
A.1 Measurement Errors . . . . .	A-1
A.2 Error Propagation . . . . .	A-3
A.2.1 Mean Flow . . . . .	A-3
A.2.2 Turbulent Flow . . . . .	A-5
A.2.3 Separation of Variables . . . . .	A-6
Appendix B. Nozzle Coordinates . . . . .	B-1
Bibliography . . . . .	BIB-1

	Page
Vita . . . . .	VITA-1

## *List of Figures*

Figure	Page
1.1. USAF Basic WAF Research Model (WL-TR-94-7015) . . . . .	1-3
2.1. Nozzle and Test Sections with WAF Model . . . . .	2-1
2.2. Coordinate System Axes . . . . .	2-2
2.3. Vacuum Pump System . . . . .	2-3
2.4. Plenum Chamber . . . . .	2-3
2.5. Flow Straightener . . . . .	2-4
2.6. Tunnel Layout - Upstream Section . . . . .	2-4
2.7. Mach 2.9 Nozzle . . . . .	2-5
2.8. Schematic of AFIT Mach 2.9 Test Facility with WAF Model . .	2-5
2.9. Mach Contours at the Test Section Inlet . . . . .	2-6
2.10. Compressible TKE Contours at the Test Section Inlet . . . . .	2-7
2.11. Blending Function . . . . .	2-8
2.12. WAF Model . . . . .	2-8
2.13. WAF model Orthographic View . . . . .	2-9
2.14. WAF Model in Test Section Ceiling . . . . .	2-9
2.15. Test Section Floor . . . . .	2-10
2.16. Shadowgraph Schematic . . . . .	2-11
2.17. Optical Grade Glass Windows . . . . .	2-11
2.18. Schlieren Schematic . . . . .	2-12
2.19. Pitot Probe . . . . .	2-14
2.20. Cone-Static Pressure Probe . . . . .	2-14
2.21. U-V Cross-Wire Hot-Film Probe Schematic (TSI, 1987) . . . . .	2-15
2.22. U-W Cross-Wire Hot-Film Probe Schematic (TSI, 1987) . . . . .	2-16
2.23. Hot-Film, Y-Z Cutting Plane Locations . . . . .	2-17



Figure	Page
2.24. Traverse Slide (Unislide Inc., Units in Inches) . . . . .	2-18
2.25. Traverse Stand . . . . .	2-19
4.1. Reference Coordinate System . . . . .	4-1
4.2. Inlet Plane Mass-Flux Contours . . . . .	4-2
4.3. Inlet Seam Shock/Expansion Pattern . . . . .	4-2
4.4. Secondary-Flow at Inlet . . . . .	4-3
4.5. Inlet Mach Contours . . . . .	4-4
4.6. Composite Shadowgraph Image of WAF Model . . . . .	4-5
4.7. Composite Schlieren Photograph of WAF Model . . . . .	4-6
4.8. Density Contours of Blending Region . . . . .	4-6
4.9. Reversed Knife-Edge Schlieren of WAF Model . . . . .	4-7
4.10. Comparison of Shock Intensity with Spanwise Mass-Flux Contours	4-8
4.11. Overall Shock Structure . . . . .	4-9
4.12. Magnified View of Shadowgraph Near the WAF . . . . .	4-9
4.13. Shock Structure at Fin-Body Junction . . . . .	4-10
4.14. Blunt Fin, Fin-Juncture Flow (Fomison,1986) . . . . .	4-11
4.15. Thin Fin, Fin-Juncture Flow (Fomison,1986) . . . . .	4-11
4.16. Oil Flow Visualization on the WAF Model, Concave Side . . . .	4-11
4.17. Oil Flow Visualization on the WAF Model, Convex Side . . . . .	4-12
4.18. Cartoon of the Vortex Structure about the Fin . . . . .	4-12
4.19. Bow Shock Structure . . . . .	4-13
4.20. Mach Number Contours . . . . .	4-14
4.21. Mach Number Progression . . . . .	4-15
4.22. Concave Mach Contour Map . . . . .	4-16
4.23. Convex Mach Contour Map . . . . .	4-17
4.24. Mass-Flux Contour Map . . . . .	4-18
4.25. Streamlines About the WAF . . . . .	4-19

Figure	Page
4.26. Static Pressure Contours . . . . .	4-21
4.27. Comparison with Inviscid Numerical Solution (AIAA 96-0190) .	4-22
4.28. Secondary-Flow Streamlines at WAF Tip . . . . .	4-23
4.29. Secondary-Flow Mass-Flux Vectors at WAF Tip . . . . .	4-24
4.30. Flow Angle About Y-Axis . . . . .	4-25
4.31. Flow Angle About Z-Axis . . . . .	4-25
4.32. Turbulent Kinetic Energy Comparisons . . . . .	4-26
5.1. Side-Mounted WAF Model and Probe Stations of Interest . . . .	5-3
5.2. Normal Wire Probe Stations . . . . .	5-4
B.1. Mach 2.9 Nozzle Coordinates . . . . .	B-1

# *List of Tables*

Table	Page
2.1. Measured Wire Resistances, $R_w$ . . . . .	2-15
2.2. Reference Positions . . . . .	2-17
2.3. Measured Probe Flexing . . . . .	2-20
2.4. Calibration Constants . . . . .	2-21
4.1. Tunnel Inflow Conditions . . . . .	4-4
A.1. Measured Error Bounds . . . . .	A-3
A.2. Freestream Conditions . . . . .	A-4
A.3. Mean Flow Error Bounds . . . . .	A-5
A.4. Turbulent Flow Error Bounds . . . . .	A-6
A.5. Variable Separation Error Bounds . . . . .	A-7
B.1. Nozzle Coordinates (Top) . . . . .	B-2
B.2. Nozzle Coordinates (Bottom) . . . . .	B-3

## *List of Symbols*

Symbol	Definition	Units
$K_c$	= Compressible turbulent kinetic energy	$\frac{m^2}{s^2}$
$M$	= Mach number	non-dimensional
$Nu$	= Nusselt number	non-dimensional
$p$	= Pressure	Pa
$r$	= Fin radius of curvature, 1.59cm	m
$R$	= Gas constant	$\frac{m^2}{s^2 K}$
$Re$	= Reynolds number, $\rho_\infty u_\infty \ell / \mu_\infty$	non-dimensional
$Re_e$	= Effective Reynolds number	non-dimensional
$R_o$	= Mass-flux ratio, $\overline{\rho v} / \overline{\rho u}$	non-dimensional
$R_{ref}$	= Hot-wire resistance at reference temperature	$\Omega$
$R_w$	= Hot-wire operating resistance	$\Omega$
$T$	= Static temperature	K
$T_t$	= Total temperature	K
$u, v, w$	= Cartesian velocities	$\frac{m}{s}$
$x, y, z$	= Cartesian coordinates	m
$\alpha$	= $T/T_t = [1 + \frac{1}{2}(\gamma - 1)M^2]^{-1}$ , Speed of Sound, $\sqrt{\gamma RT}$	non-dimensional $\frac{m}{s}$
$\beta$	= $(\gamma - 1)\alpha M_\infty^2$	$\frac{m}{s}$
$\gamma$	= Ratio of specific heats, 1.4 for air	non-dimensional
$\phi$	= Flow angle about y-axis	radians
$\mu$	= Molecular viscosity	$\frac{Kg}{ms}$
$\nu$	= Molecular kinematic viscosity, $\mu/\rho$	$\frac{m^2}{s}$
$\theta$	= Flow angle about z-axis	radians
$\rho$	= Density	$\frac{Kg}{m^3}$
$\tau_{ij}^T$	= Turbulent shear stress tensor components	$\frac{Kg}{ms^2}$

*Subscripts*

$e$	=	Equilibrium, effective
$ref$	=	Reference
$t$	=	Total or turbulent
$w$	=	Wall, wire
$\infty$	=	Freestream

*Superscripts*

$T$	=	Turbulent
$()'$	=	Reynolds fluctuating component
$()''$	=	Favré fluctuating component
$\overline{()}$	=	Reynolds averaged component
$\widetilde{()}$	=	Favré averaged component

*Abstract*

A ceiling-mounted semi-cylindrical model containing a single wrap-around fin (WAF) was tested in the AFIT Mach 2.9 test facility. Flow visualization using oil-flow streaklines, schlieren images and shadowgraph photography revealed a  $\lambda$ -shock at the fin-body juncture and the development of an asymmetric bow-shock about the fin. Quantitative measurements were taken with a  $10^\circ$  cone-static pressure probe, a Pitot pressure probe and two cross-wire hot-film probes (u-v and u-w components, respectively). Measurements were made at cutting-planes from the inlet of the test section to aft of the model, with emphasis placed in the vicinity of the WAF. Results include cutting-plane profiles and contours of mean and turbulent fluctuations of the primitive and conserved flow variables. It was found that the incompressible turbulent fluctuating quantities are equally as descriptive of the flow structure in the fin's vicinity as the compressible turbulence fluctuations. The asymmetric bow-shock was found to be an inviscid phenomenon which was stronger on the concave side than the convex side and of diminishing strength at the tip with no bleeding effects over the tip.

# MACH 2.9 INVESTIGATION INTO THE FLOW STRUCTURE IN THE VICINITY OF A WRAP-AROUND FIN

## *I. Introduction*

### *1.1 Problem Statement*

Current military design emphasis has been placed on low observable properties for advanced fighter aircraft. To reduce the intensity of radar return signatures of airframes, researchers are investigating the use of internal weapon stowage and decreasing the use of sharp corners. A design solution to these problems is to utilize wrap-around fins (WAFs) on the missiles carried by these aircraft. A WAF is a lift or control surface which has the same curvature of the cylinder to which it is mated. The key feature of a WAF is that when stowed it fits flush with the cylinder surface.

Wrap-around finned missiles (with stowed fins) can be stored in a compartment of less volume than a missile body of the same size which utilizes straight, non-folding fins. With WAF missiles employed, an airframe can carry more missiles in the volume previously used by the straight fin missiles. Alternatively, the airframe can use the internal volume savings for fuel or avionics. Wrap-around fin missiles simplify the design of the airframe housing and launching equipment on airframes which integrate the weapon in partial submersion. Partial submersion WAF designs avoid difficulties associated with fin-fuselage contact. An additional feature of the WAF missile is that the fin stowed configuration has a lower radar return due to the loss of the fin-body juncture. Therefore, a low observables benefit is achieved by using WAF missiles on external pylons for current operational aircraft. While

missile and airframe designers are interested in WAFs for the previously mentioned benefits, there are interesting features of WAF missile designs.

There are three key differences between WAF missiles and straight-finned munitions: WAFs experience a rolling moment reversal near Mach 1, a coupling between pitch and yaw, and a possible dynamic instability associated with undesirable side moments. These WAF performance characteristics are coupled to the flow structure about the fin. At the time of this publication, a detailed characterization of the flowfield in the vicinity of a WAF has not been made. This study represents an attempt to experimentally address this void in the literature.

A natural first step in looking at the WAF flowfield is to eliminate the influence of other fins. The present effort considers a single WAF attached to a partial cylinder, based on the dimensions of the USAF basic research missile (BRM) model. The fin is placed at  $0^\circ$  angle-of attack to create a baseline case. However, the "real world" missile effects are not entirely removed. The WAF is mounted to half of a semi-cylinder, to place the fin out of the natural boundary layer of the tunnel while providing for the investigation of the curvature effects associated with missile-fin junctures.

An additional goal of this research is to provide information of value to computational fluid dynamics (CFD) research. To that end, conventional hot-wire anemometry measurements provide the necessary mean flow and turbulence information required to validate numerical efforts. Great care is taken in detailing the upstream conditions of the flowfield, to enable numerical duplication and expansion of this work. Additionally, the influence of turbulence and compressibility issues on numerical simulation is examined. It is the intent of the author that this information will help guide further experimental and numerical research in this area.



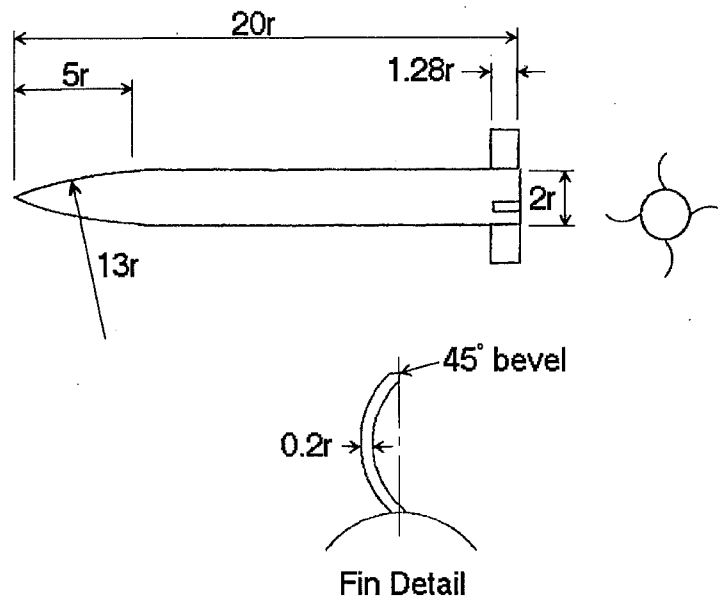


Figure 1.1 USAF Basic WAF Research Model (WL-TR-94-7015)

## 1.2 Background

WAFs find uses in many military applications - from tube launched munitions for the Army and Navy, to internally stowed weapons in the Air Force. These multiple applications produce an array of WAF designs to study. The WAF chosen for this design is one patterned after the BRM (7). Figure 1.1 shows the pattern of the BRM with a wrap-around fin. The BRM differs from the WAF model by a straight fin with the same planform area.

Numerous experimental tests are accomplished in instrumented ballistic ranges (75, 41, 10, 12, 71, 11, 68). The majority of these tests cover the subsonic and transonic flight regime (75, 41, 10, 12, 11). These tests show a roll moment reversal near Mach 1.0, a coupling between yaw and pitch and a potential for side moments leading to undesirable dynamic instabilities. The supersonic experiments tend to show a loss of static stability near Mach 4.0 (71). Although these range experiments

provide valuable design information, the facilities are not designed for detailing the flow structure of the WAF.

Some wind tunnel tests on WAFs have been conducted (8, 47). In the paper by Kretzschmar, et al. (47), the focus was on designing lift and control surfaces and not of flowfield description. Abate and Hathaway (8) provided very useful information on the surface structure of the missile with multiple WAFs. Lacking from the sum of these previous experiments was information pertaining to the characteristics of the shock structure about the WAF and turbulence information near the WAF.

Numerical simulations were performed on missile configurations with a view toward characterizing the shock structure (9, 25, 54, 70). The study of the Hypersonic Applied Research Technology (HART) missile showed a pressure bleeding effect over its straight fins at angle-of-attack (54). The remaining studies were performed on wrap-around fins and did not model turbulence.

Settles and Dodson (61) have defined criteria necessary in experimental data gathering for CFD research in supersonic turbulent shock-boundary layer interaction. A characteristic of this flowfield associated with the WAF configuration tested is the shock/boundary-layer interaction near the juncture of two curved surfaces. Therefore, these criteria provide appropriate guidance for the current research effort. Using their criteria, Settles and Dodson have identified a number of high-quality experimental datasets suitable for CFD research into turbulence model validation. Each of these experiments are supersonic "building-block" experiments containing turbulence information. Some studies in the database have considered the interaction between straight fins and flat plates (43, 37, 49). The current study represents an incremental advance over typical shock generation schemes by introducing surface curvature effects. The primary emphasis of creating these criteria is the need to numerically simulate the experimental environment. To that end, this effort contains a rigorous treatment of the conditions at the inlet to the test section. Additionally, the uncertainties associated with the current study are defined and quantified.

### *1.3 Objectives*

The goals of this experimental study are two-fold. The primary goal is to experimentally characterize the mean and turbulent flowfield in the vicinity of a wrap-around fin. The shock structure is determined, using a myriad of flow visualization techniques; shadowgraph imagery, schlieren photography and oil-flow surface streaklines. Additionally, mean flow quantities and turbulence information are measured by Pitot, cone static pressure and cross-wire hot-film anemometers in the flowfield about the WAF. An alternate goal is to provide this information in a useful form for validation of numerical turbulence modeling.

### *1.4 Outline*

This section provides a road map of the chapters which follow. In Chapter II, the facility for this experiment was detailed along with the methodology of hot-wire measurements, shadowgraph and schlieren photography, and oil-flow streakline visualization. The process used in the reduction of measured voltages to valuable information about the primitive and conserved flow variables is detailed Chapter III. The results of the flowfield survey are presented in Chapter IV. Finally, Chapter V provides a series of the conclusions and suggests the direction for future efforts.

Additional information is included in the appendices. Appendix A details the uncertainty in measurements and the effect of these uncertainties on the results. Appendix B provides the coordinates of the AFIT Mach 2.9 Test Facility's converging-diverging nozzle.

## II. Experimental Apparatus and Methodology

This chapter details the equipment and techniques used to perform the experimentation of this thesis.

### 2.1 Mach 2.9 Facility

The AFIT Mach 2.9 test facility is an intermittent high pressure blow-down tunnel with downstream evacuation. The tunnel is located in Building 640, Room 148 on Wright-Patterson AFB, Area B. This facility features a run time of 30 seconds with an evacuation time of 6 to 10 minutes. Each test section measures  $6.35 \times 6.35 \times 33.02\text{cm}$ . Figure 2.1 is a photo of the nozzle and the two removable test sections.

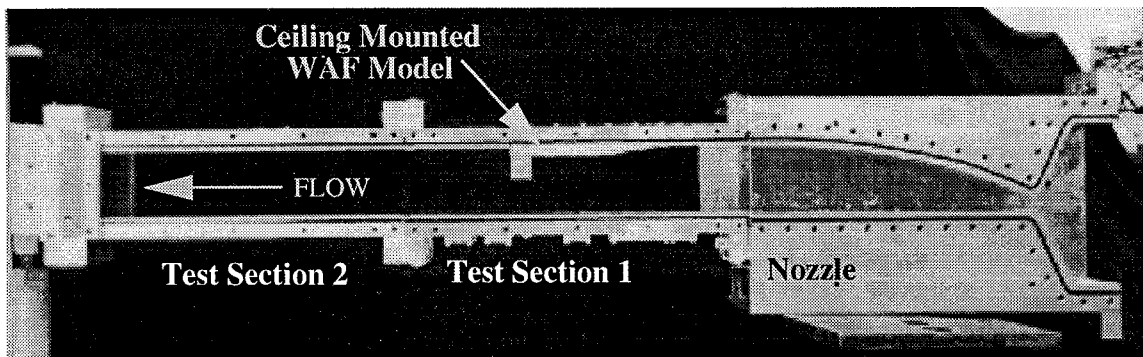


Figure 2.1 Nozzle and Test Sections with WAF Model

The coordinate system applied throughout this thesis was the hot-film coordinate system. The origin for this system was defined to be at the nozzle throat on the floor's port side (looking downstream). The x-axis runs longitudinally downstream and the y-axis is positive up. The z-axis runs horizontally towards the starboard wall (facing downstream) - thus completing the right-handed orthogonal triad. Figure 2.2 locates the coordinate axes at the origin.

The vacuum tanks (with a volume of  $\sim 16\text{m}^3$ ) are evacuated by one Stokes Microvac Pump - model 212-11, and two IPP Evacuation Vacuum Pumps - model FW-EV-PI each powered by a Reliance XE Dutymaster A/C motor requiring 5.6kW.

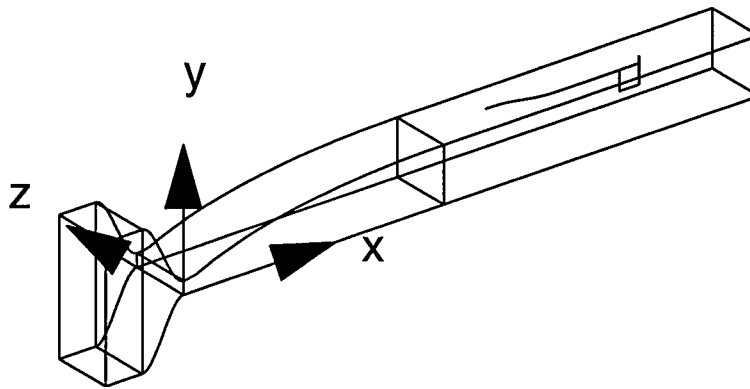


Figure 2.2 Coordinate System Axes

The minimum vacuum achievable is  $\sim 2\text{mmHg}$ , though a typical run required only  $10\text{mmHg}$ . Figure 2.3 shows the vacuum pump system.

The high pressure air is delivered at  $6.8\text{atm}$  from the house air supply, which is powered by two Atlas Copco GAU 807 compressors delivering  $0.45 \frac{\text{Kg}}{\text{s}}$ . The moisture is removed from the air by two Pioneer R500A refrigeration-type air dryers. The air flows to the tunnel from the compressors and dryers by  $\sim 150\text{m}$  of  $7.62\text{cm}$  diameter cast iron pipe. Due to a pressure drop during the course of a tunnel run, the pressure is regulated by a Leslie Regulator Valve class GPK-1, size 2 – which is controlled by the Fairchild Pressure Regulator System model HP 190A. The air passes through the pressure regulator into the plenum chamber and flow straightener, which are shown in Figures 2.4 and 2.5 - respectively. The plenum and flow straightener are connected to the nozzle in Figure 2.6.

The air flow is accelerated through a two-dimensional converging-diverging nozzle as described in Figure 2.7. The coordinates originate from the throat on the tunnel floor. Nozzle coordinates are tabulated in Appendix B.

At this point, the flow enters sequentially through two removable test sections and into the vacuum tanks by way of an adjustable diffuser. Figure 2.8 is a schematic of the facility.

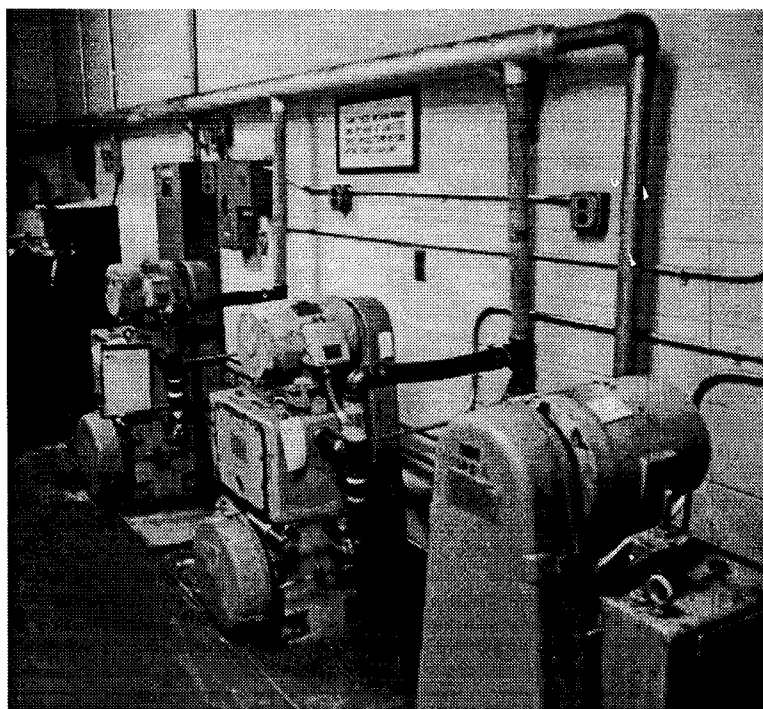


Figure 2.3 Vacuum Pump System

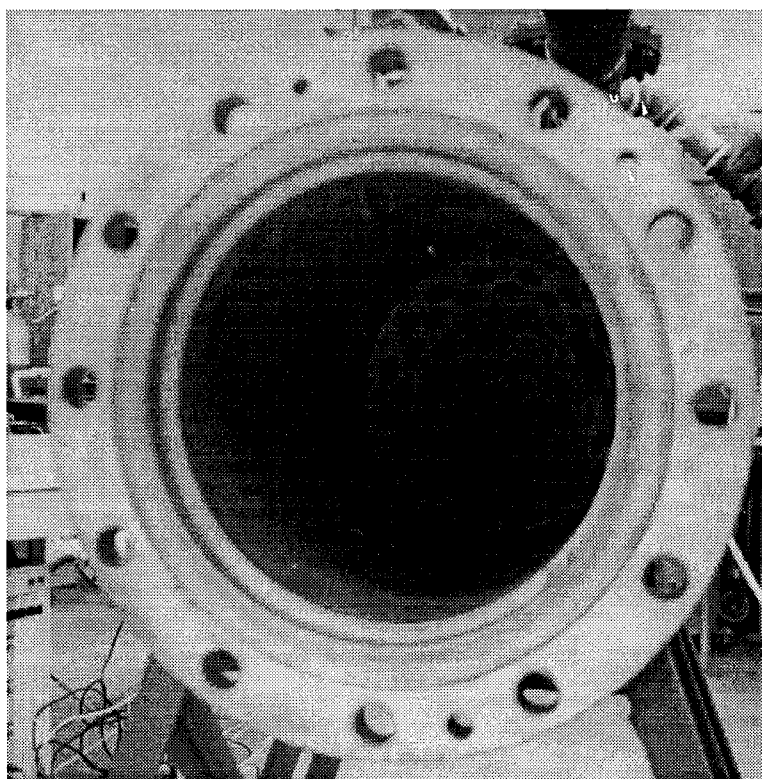


Figure 2.4 Plenum Chamber

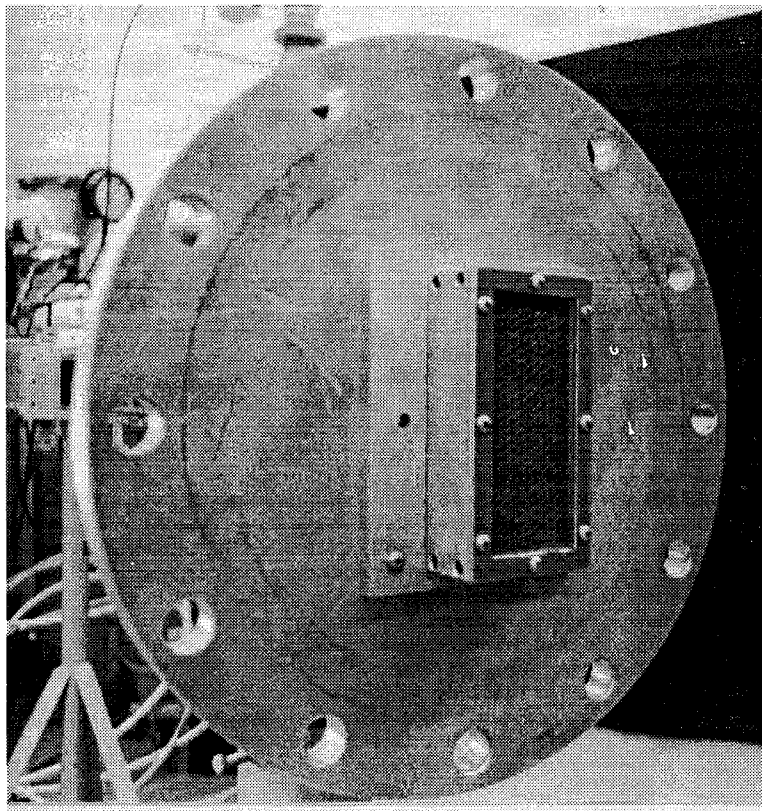


Figure 2.5 Flow Straightener

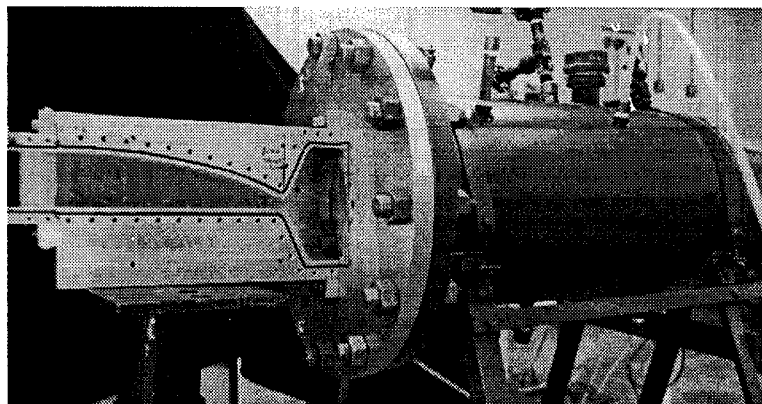


Figure 2.6 Tunnel Layout - Upstream Section

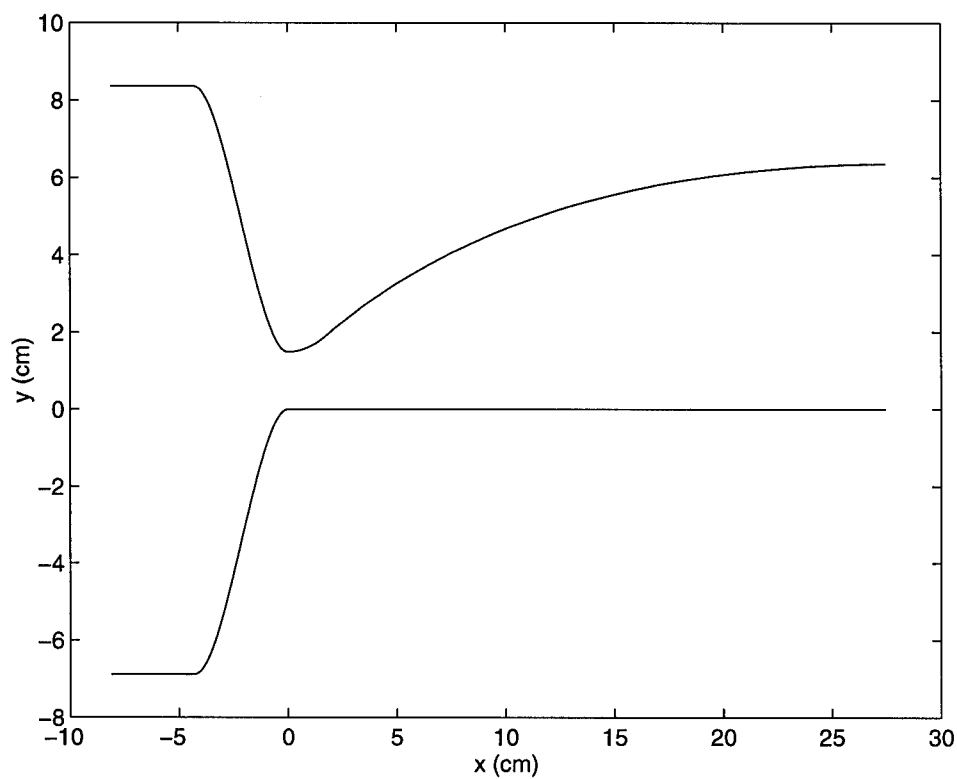


Figure 2.7 Mach 2.9 Nozzle

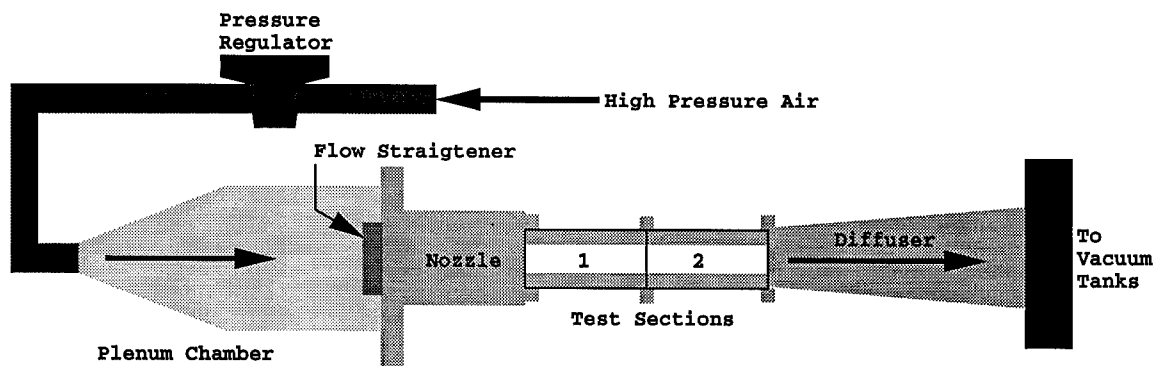


Figure 2.8 Schematic of AFIT Mach 2.9 Test Facility with WAF Model



At the entrance to the test section, the freestream Mach number is 2.85 with a standard deviation of 1.27% and a measurement uncertainty of 1.8%. Figure 2.9 is a contour plot of the Mach number at the inlet to the test section. Note the Cartesian coordinates are non-dimensionalized by the fin radius.

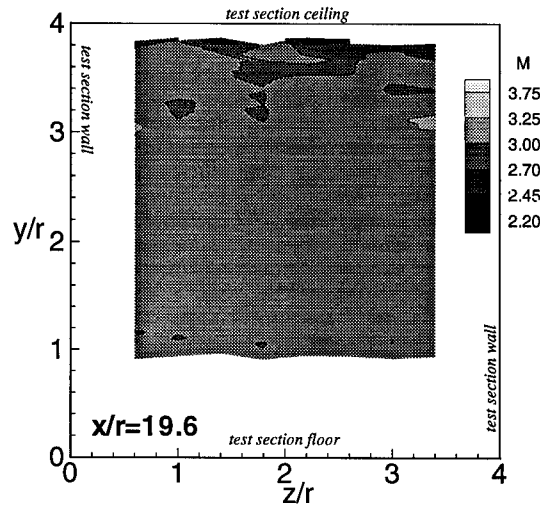


Figure 2.9 Mach Contours at the Test Section Inlet

The boundary layer thickness is 5.3mm (based on 95% of  $M_\infty$ ) at a distance 31.1cm from the throat - just downstream of the test section entrance - with an uncertainty of 4.1% in measured position. The settling chamber operates nominally with a total pressure and total temperature of 2.07atm and 297K, yielding a freestream Reynolds number of  $1.70 \times 10^7/\text{m}$ . The freestream turbulence (defined as the square root of two-thirds the non-dimensional compressible turbulent kinetic energy (TKE) (74)) is 0.8% with a standard deviation of 0.2%. The compressible turbulent kinetic energy at the test section entrance is shown in Figure 2.10.

The uncertainties related to the documentation of measured freestream quantities are explained in Appendix A.

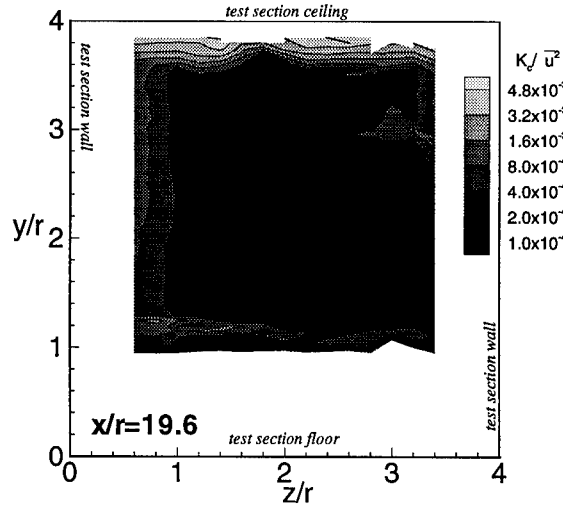


Figure 2.10 Compressible TKE Contours at the Test Section Inlet

## 2.2 Wrap-Around Fin Model

The WAF model is a cylinder of the fin radius blended to the removable test section ceiling at a peak height of 0.79cm. The cylinder is 8.14cm in length with the single fin placed at the downstream base. Upstream, the cylinder is blended to the tunnel floor with a polynomial spline which ensures second order continuity. The blending function (Figure 2.11) is translated into physical coordinates in Equation 2.1.

$$\begin{aligned}
 \zeta &= 6\eta^5 - 15\eta^4 + 10\eta^3 \\
 \eta &= 0.2\frac{z}{r} - 4.296, \quad 21.48 \leq \frac{z}{r} \leq 26.48 \\
 \frac{h}{r} &= \sqrt{1.0 - (\frac{z}{r} - 2.0)^2} - 0.5, \quad 1.134 \leq \frac{z}{r} \leq 2.866 \\
 \frac{y}{r} &= 4.0 - \frac{h}{r}\zeta
 \end{aligned} \tag{2.1}$$

The blending region is 7.94cm long and starts 34.10cm from the nozzle throat. The fin has a thickness of 0.32cm, a span of 2.25cm and a chord length of 2.03cm. The leading edge and tip of the fin are beveled at 45°. Figure 2.12 is a perspective view of the WAF model in the test section ceiling. Figure 2.13 is an orthographic drawing

with dimensions - a detail of the WAF model. The model is then inserted into a test section ceiling as shown in Figure 2.14.

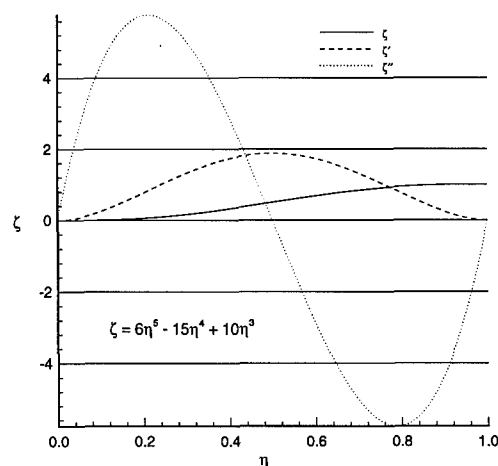


Figure 2.11 Blending Function

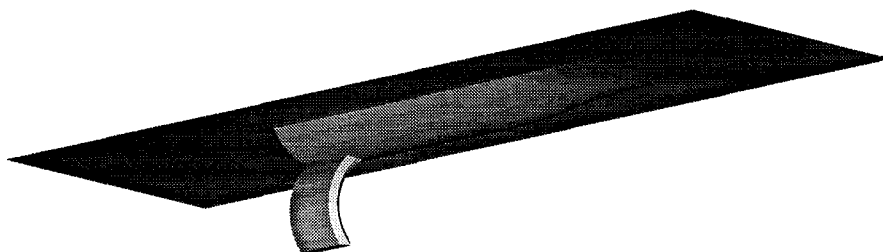


Figure 2.12 WAF Model

The floor of the test section was designed with a series of interchangeable plugs. The plugs were 5.08cm wide and 0.64cm thick with the ends rounded by a 0.32cm radius. These plugs allowed the 0.64cm diameter probe sleeve to move across the floor in the z-axis. A large plug measuring 5.08 × 3.81cm contained a slot 2.54cm long and 0.64cm wide - with all corners rounded by a 0.32cm radius. The probe

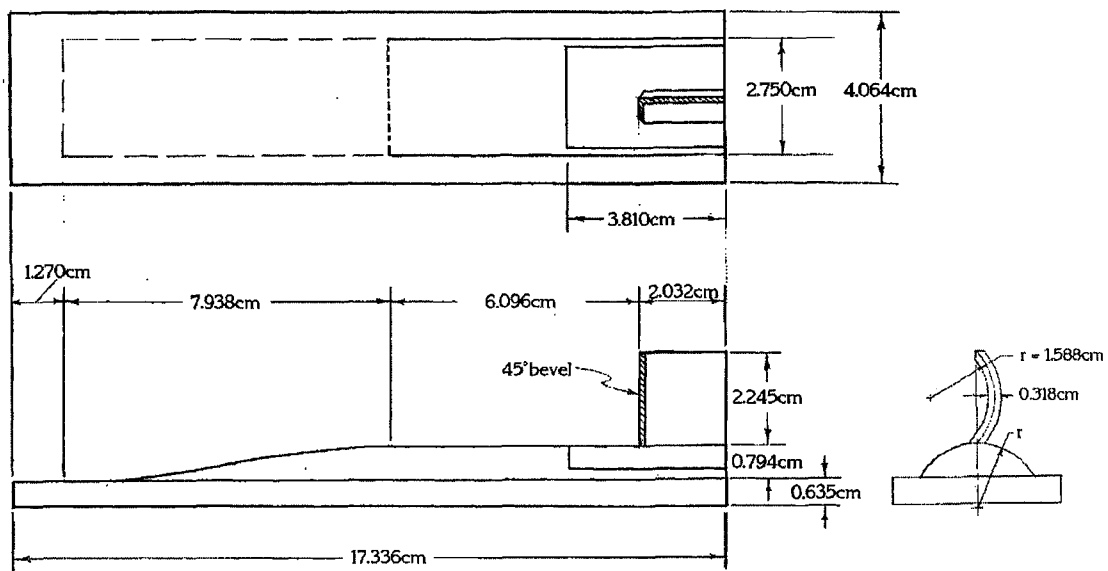


Figure 2.13 WAF model Orthographic View

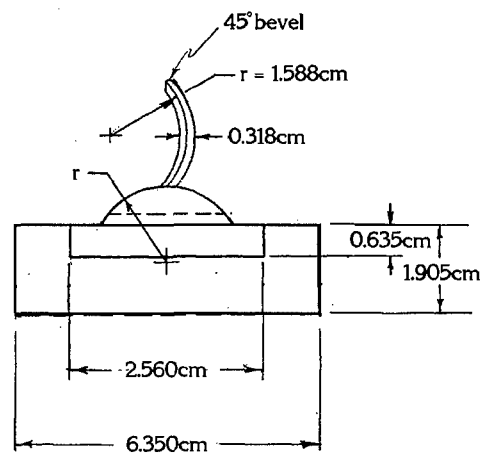


Figure 2.14 WAF Model in Test Section Ceiling

sleeve can slide across the y-axis near the fin (during operation the sleeve is secured by a pressure plate). Figure 2.15 is a photo of the test section floor and removable plugs.

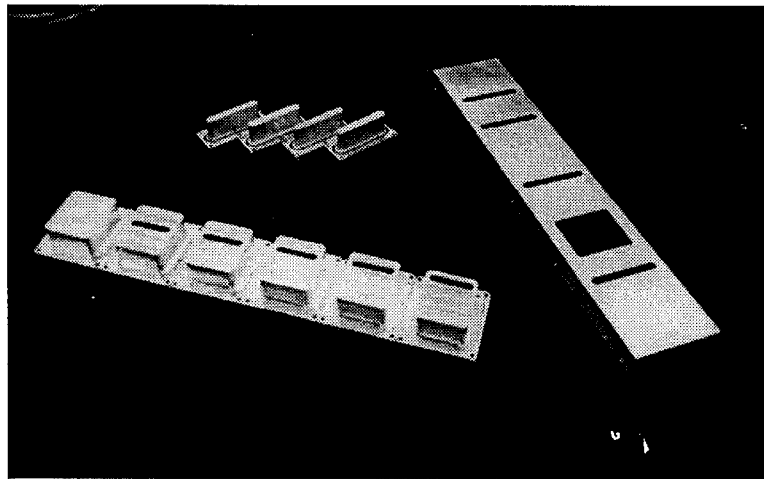


Figure 2.15 Test Section Floor

### *2.3 Flow Visualization*

Shadowgraphs and schlieren images were taken using Xenon Corporation model 437B nanopulser, with a spark duration of 10 nanoseconds, as a light source (6). The images were recorded on Polaroid type 57 high speed instant black and white film. For shadowgraphs, the light source was aimed away from the test section to be reflected back by a 1.524m focal length mirror - placed 1.524m from the center of the test section. It can be shown that the intensity of a shadowgraph correlates to the second order gradient of index of refraction in the plane normal to the light beam (32). The index of refraction is related linearly to the density of the medium the light passes through. Figure 2.16 is a schematic of the shadowgraph setup. Photos were taken through both the Plexiglas and the optical grade glass. The optical grade shadowgraphs were of much higher quality than the Plexiglas photos. Figure 2.17 shows the optical grade glass walls installed on the first test section.

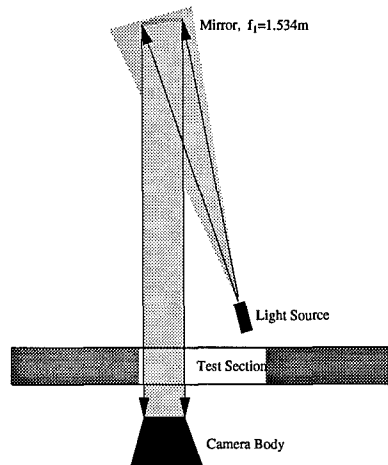


Figure 2.16 Shadowgraph Schematic

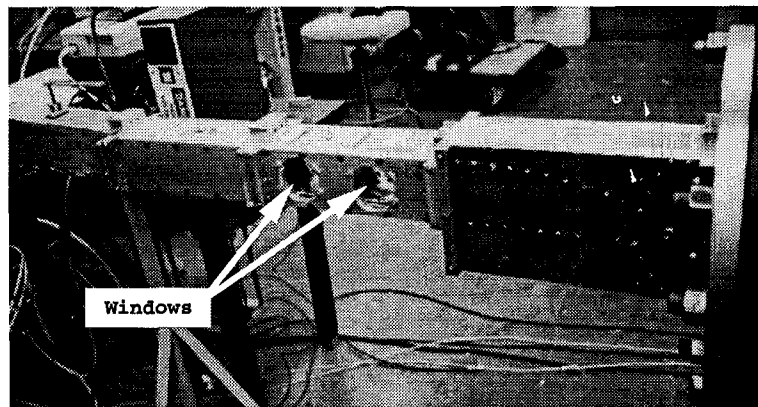


Figure 2.17 Optical Grade Glass Windows

The schlieren setup introduces another concave mirror, with 1.534m focal length - as well as a knife edge. The light passing through the test section from the shadowgraph is now focused and half of the image is blocked by the knife edge at the focal point. The image is then reflected by a flat mirror and focused through a lens - to cope with space limitations. The intensity of the recorded schlieren image is equivalent to the gradient of density normal to the knife edge (32). Therefore, a knife edge positioned horizontally will display the vertical density gradient. Rotating the knife edge  $180^\circ$  will produce the negative image. Figure 2.18 is the schlieren setup.

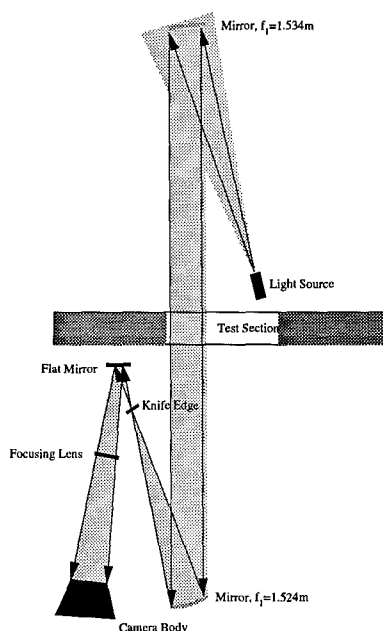


Figure 2.18 Schlieren Schematic

Both photographic systems were aligned using an air-bubble torpedo level. First the test section was leveled. Then the mirrors were bore-sighted using an Oriel He-Ne gas laser model 79255 producing a 0.48mm diameter linearly-polarized beam with a wavelength of 632.8nm and a power of 0.5mW (3). No focusing was needed for the shadowgraph. However, the schlieren was focused by using the light source to read an overhead transparency on a ground-glass plate inserted in the camera body. The transparency was suspended in the center of the tunnel test section through one of the removable plugs.

Surface streakline patterns were visualized using an oil mixture of stamp ink and Dow Corning 200 Fluid, 1000 cSt. General purpose cleaning fluid was used to mix the ink and oil. For these runs, the WAF model was placed in the test section floor - to keep the oil from dripping off before the test. The oil mixture was applied to the cylinder, floor and fin. Then the tunnel was run for 15 to 20 seconds. The results were photographed after the tunnel had stopped - allowing for the removal of the walls. The tunnel unstart caused negligible changes to the observed flow patterns.

#### *2.4 Pressure and Temperature Measurements*

All pressure measurements were made by Endevco pressure transducers. These transducers measure gauge pressure. The ambient pressure was measured at the beginning and end of a series of runs - about every two hours - on a Wallace & Tiernan model 233111 absolute pressure gauge. The Pitot pressure in the test section was measured with a Pitot probe, Figure 2.19. The cone-static pressure was measured with a cone-static probe which had a  $10^\circ \pm 0.03^\circ$  semi-vertex angle as seen in Figure 2.20. The probe pressure was measured by an Endevco model 8510C-15. The signal was processed through an Endevco model 4423 signal conditioner and powered by an Endevco model 4225 power supply. The voltage output was displayed on an HP 3446A digital multimeter. Just downstream of the flow straightener, the plenum pressure is measured through a Pitot tube with an Endevco pressure transducer, model 8510C-100 and is reported by an Endevco pressure display unit, model 4428A. The plenum temperature was measured by an Omega K type thermocouple and displayed on an Omega model 15B display unit (5).

#### *2.5 Hot-Film Anemometry*

Constant temperature cross-wire hot-film anemometry measurements were used in the majority of the flowfield analysis. The employed system consisted of the TSI IFA100 Intelligent Flow Analyzer which contained three model 150 constant tem-



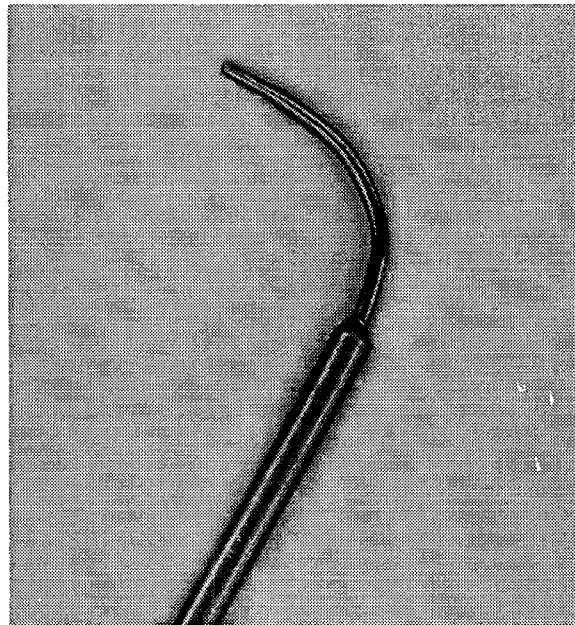


Figure 2.19 Pitot Probe

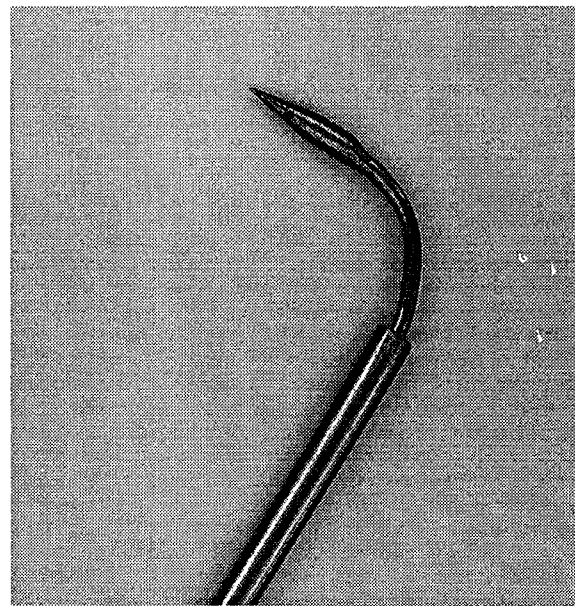


Figure 2.20 Cone-Static Pressure Probe

perature anemometers with a series resistance ( $R_s$ ) of  $50\Omega$ . Two anemometers were used, each attached to one channel of the cross-wire probe. The two cross-wire probes used were the model 1243-20 (u-v plane) and 1243AN-20 (u-w plane) hot-film probes. Each probe has a similar configuration, differing only by the orientation of the wires. The wires were actually made of a thin film of platinum  $51\mu\text{m}$  in diameter and 1mm long. The measured resistances of the ‘wire’ and attached cable are summarized in Table 2.1

Table 2.1 Measured Wire Resistances,  $R_w$

Probe Serial Number	Channel 1 ( $\Omega$ )	Channel 2 ( $\Omega$ )
934011	5.898	5.822
934012	6.088	6.184
944011	6.880	6.887
934012	6.010	6.898

Overheat ratios of  $\sim 2.0$  were set by an external breadboard and high quality resistors, in combinations of  $1\Omega$  and  $10\Omega$ . Great care was taken in placement of the resistors on the breadboard in an attempt to reduce inductance and resulting oscillatory behavior. The cross-wire probes were seated in a TSI two-sensor probe support for placement into the tunnel. Figures 2.21 and 2.22 are schematics of the u-v and u-w hot-film probes, respectively.

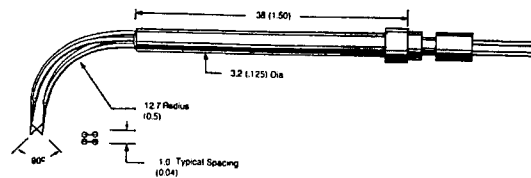


Figure 2.21 U-V Cross-Wire Hot-Film Probe Schematic (TSI, 1987)

To properly determine the flowfield properties, the hot-film response must be calibrated. The calibration was accomplished by placing the probe in the test section at a point of known Mach number and varying the Reynolds number. The calibration point for this study was at the center of the test section and 31.12cm downstream

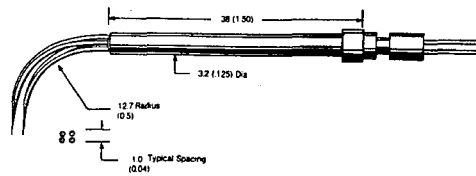


Figure 2.22 U-W Cross-Wire Hot-Film Probe Schematic (TSI, 1987)

of the nozzle throat. The Mach number used in calibration was 2.9. (The measured Mach number at the calibration point was 2.83, a 2.4% difference.) The Reynolds number was varied by adjustments to the plenum pressure. A curve fit was obtained by least squares regression relating the wire voltage from the anemometer to the local Reynolds number. A more detailed mathematical explanation of the calibration technique is found in Chapter III.

## 2.6 Data Acquisition

Quantitative measurements were made at 165 individual stations throughout the test section. These stations formed y-z cutting planes. Each station was referred to by two reference positions. The first reference was the non-dimensional position  $\frac{z}{r}$ . The second, and more interesting, reference was to the non-dimensional position  $\frac{x}{r}$ . The latter reference position was the distance from the nozzle throat to the plane in which the unflexed hot-film probe is located. Note that the Pitot and cone-static probes were actually longer than the hot-film probe, by 6.35mm. The difference in lengths resulted in a determination of Mach number which was located upstream of the hot-film probe measurements made from the same station. This difference in position was accounted for in the region near the fin, where the pressure probes were aligned to the hot-film probe. However, the measurements made upstream of the fin implicitly assumed a small change in pressure over the distance between pressure probe and hot-film probe tips. Figure 2.23 shows the y-z cutting planes formed by the hot-film tip, which include flex effects. The  $\frac{x}{r}$  reference position is found by extrapolating the position in Figure 2.23 down to the floor. The reference positions

( $\frac{x}{r}$ ) associated with Pitot, cone-static and hot-film probe tips corresponding to each cutting plane in Figure 2.23 are detailed in Table 2.2.

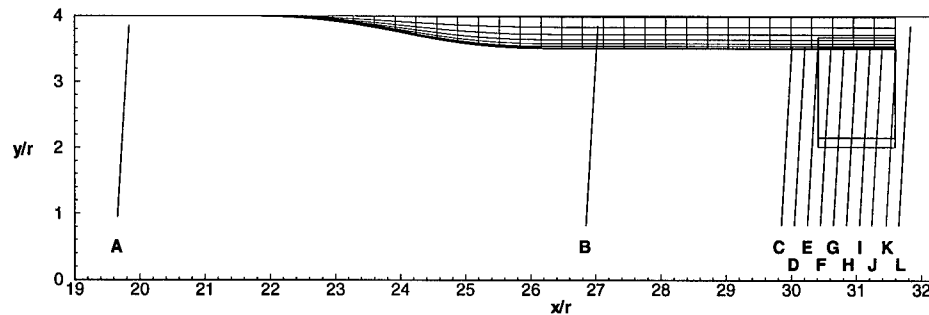


Figure 2.23 Hot-Film, Y-Z Cutting Plane Locations

Table 2.2 Reference Positions

Reference Letter	Unflexed Cross-Wire Probe Position (Reference)	Unflexed Pressure Probe Position
	$\frac{x}{r}$	$\frac{x}{r}$
A	19.6	19.2
B	26.8	26.4
C	29.8	29.4
D	30.0	29.6
E	30.2	29.8
F	30.4	30.0
G	30.6	30.2
H	30.8	30.4
I	31.0	30.6
J	31.2	30.8
K	31.4	31.0
L	31.6	31.2

The flowfield was mapped by attaching a particular probe to a custom made traverse stand pictured in Figure 2.25. The stand has a Unislide Assemblies series A2500 traverse slide with a thread pitch of 40 per 2.54cm (Figure 2.24). To digitally record the traverse position, a Linear Displacement Voltage Transducer (LDVT) was attached between the moving slide and the traverse stand. The LDVT was pow-

ered from a Hewlett Packard 6205C Dual DC Power Supply. The output from the LDVT was run through the LDVT Signal Conditioner model 1000-0012 to produce the recorded voltage. The traverse slide assembly can be adjusted manually, or by computer with the help of a stepper motor and Arrick Robotics model MD-2 Dual Stepper Motor Driver. The driver was controlled by Microsoft's Quick BASIC software and subroutines provided from Arrick Robotics on a Compaq Deskpro 80386DX running at 25MHz.

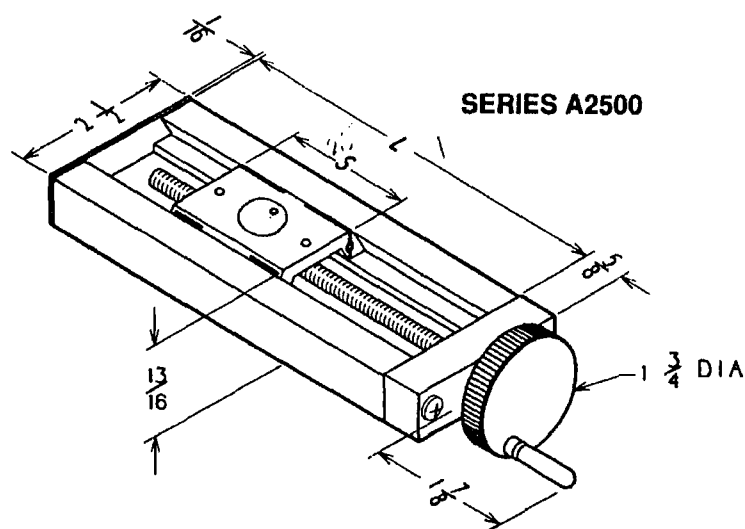


Figure 2.24 Traverse Slide (Unislide Inc., Units in Inches)

Before starting the tunnel, the traverse was positioned to put the probe 0.254cm away from the ceiling of the tunnel. This small gap provided a measure of safety to keep the probes from brushing the ceiling during tunnel operation, as the probe flexes back as the flow rushes past. Probe position was determined by 'sighting' through two matching grid patterns - one affixed to each Plexiglas tunnel wall. As the tunnel was run, the flexing of the probe was very noticeable. Measurements were made to determine the flexing of the probe, the results from which are presented in Table 2.3. Also, since the cross-wire probes determine velocity information, the flex angle of the u-v was required (the flex of the u-w probe had an insignificant effect on the

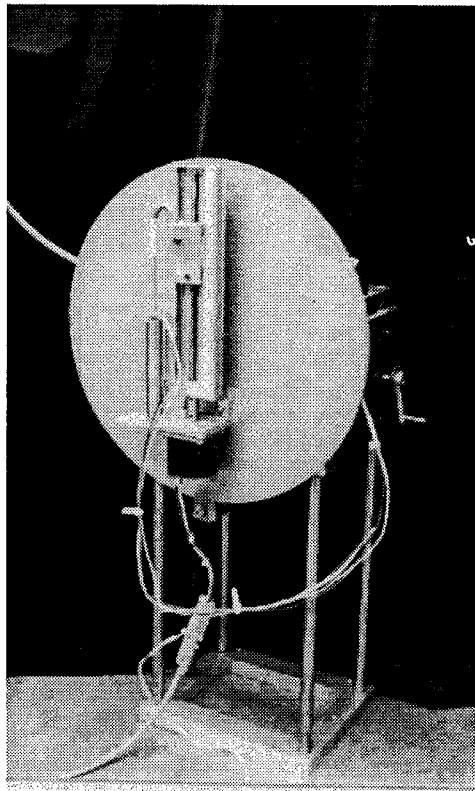


Figure 2.25 Traverse Stand

angle each wire made to the flow). The flex angle of the u-v probe was determined to be 2.86°.

Table 2.3 Measured Probe Flexing

Probe	$\frac{\Delta y}{y}$	$\frac{\Delta x}{y}$
Pitot	1.00%	7.25%
Cone-Static	1.00%	5.00%
Cross-Wire	2.25%	6.25%

The general strategy applied to mapping the flowfield was to insert a probe into one of the slots in the tunnel floor and take measurements with the traverse in motion. The traverse speed was  $0.19 \frac{\text{cm}}{\text{s}}$ . The freestream flow speed at the entrance to the test section was  $608.1 \frac{\text{m}}{\text{s}}$ . Therefore, the traverse speed introduced only negligible errors to the data acquisition. Taking data while the traverse was in motion allowed almost the entire test section, 4.5cm, to be covered in one tunnel run - greatly speeding the acquisition process. At the end of one tunnel run, the probe would be positioned 0.32cm away from the previous position within the slot on the tunnel floor. This process was repeated until the entire plane was covered. The mapping of every plane was accomplished with one probe, before moving onto the next probe. For example, the Pitot probe was used to map the tunnel before proceeding onto the cone-static probe and cross-wire probes. This strategy was altered slightly for hot-film mapping. The calibration was done at the beginning or end of a mapping plane. Since the probe had to be removed to exchange slots in the tunnel floor, the probe was placed at the calibration point for one calibration run and then placed in the next slot in the sequence. The calibration procedure was determined to be acceptable given the variation in calibration coefficients between runs was negligible as seen in Table 2.4.

The plenum pressure, probe pressure, or hot-film voltage and position were recorded on a Nicolet MultiPro digital acquisition (D/A) unit containing four model 120 digital acquisition boards - each capable of sampling four channels at 1MHz.

Table 2.4 Calibration Constants

Probe Serial Number	Channel 1			Channel 2		
	Overheat Ratio	a	b	Overheat Ratio	a	b
943011	2.00	0.178	-0.292	2.01	0.172	-0.360
	2.00	0.173	-0.235	2.01	0.166	-0.303
943012	2.01	0.174	-0.316	1.97	0.179	-0.397
	2.01	0.175	-0.316	1.97	0.181	-0.432
	2.01	0.176	-0.270	1.98	0.181	-0.379
	2.01	0.183	-0.290	1.98	0.182	-0.406
	2.01	0.184	-0.330	1.98	0.183	-0.431
	2.01	0.183	-0.323	1.98	0.179	-0.409
944011	2.00	0.149	-0.343	2.00	0.160	-0.355
	2.00	0.149	-0.357	2.00	0.164	-0.378
	2.00	0.151	-0.362	2.00	0.158	-0.369
	2.00	0.156	-0.367	2.00	0.160	-0.371
	2.00	0.154	-0.389	2.00	0.162	-0.384
	2.00	0.149	-0.394	2.00	0.166	-0.406
	1.99	0.160	-0.428	2.00	0.161	-0.409
	1.99	0.158	-0.413	2.00	0.159	-0.377



The D/A unit was controlled by Microsoft Windows software running on a Zenith 80486DX 33MHz personal computer. The plenum pressure, Pitot and cone-static pressure and position from the LDVT were sampled at 200Hz, while the anemometer voltages were sampled at 10kHz. A faster sampling rate was desired for the hot-film probes; however, the D/A unit would only store 256Kbytes of data. At 10kHz, 26.2 seconds of data could be stored. The traverse required 23.4 seconds to span the tunnel. Therefore, a faster sampling rate would require multiple runs to span one line of data. 159 individual lines of data were mapped in this experiment, requiring almost 1300 tunnel runs and 250 hours of tunnel time - which constrained the sampling rate to 10kHz. Since the Nyquist frequency of this sampling rate is 5kHz, no spectral decomposition was performed and the data was not background filtered at 60Hz.

### *III. Data Reduction*

Though the Navier-Stokes equations govern the motion of Newtonian fluids, modifications have been made to the Navier-Stokes equations to account for the wide range of length and time scales associated with turbulent flowfields. In such, approximate forms of the primitive variables, such as velocity, density, pressure and temperature, can be split into two terms

$$Q = \overline{Q} + Q'$$

Typically, the first term is a time averaged quantity and the second term is the fluctuation about the mean value. From this variable separation, the Reynolds-averaged Navier-Stokes (RANS) equations are formed. However, the mean and fluctuating values obtained from hot-wire anemometry do not directly correlate to the variables used in RANS (with the exception of Reynolds turbulent shear stress). Significant manipulations (the scope of this chapter) are required to produce the normalized fluctuations common to RANS analysis.

CFD applications typically involve the use of conservative variables, such as mass-flux and energy. CFD tasks use mass-weighted time averaging, which is related to RANS variables by

$$\begin{aligned} Q &= \tilde{Q} + Q'' \\ \tilde{Q} &= \frac{\rho \overline{Q}}{\bar{\rho}} \\ \overline{Q''} &= -\frac{\rho' \overline{Q'}}{\bar{\rho}} \end{aligned}$$

These relationships are the basis of the Favré-averaged Navier-Stokes (FANS) equations. It is important to note that hot-wire results must also be manipulated to provide data of value for CFD. The separation of variables into RANS and FANS form requires the use of controversial assumptions and the omission of higher order terms. These simplifying assumptions degrade the accuracy of the results. Nonethe-

less, these results are intended to give CFD analysts a comparison for many of the variables which they generate.

This chapter examines the method used to reduce data obtained via the Pitot pressure probe, cone-static pressure probe, u-v and u-w hot-film cross-wire probes. Mean flow information such as density, pressure, and velocity magnitude are derived from the pressure probes. The hot-film cross-wire probes determine velocity vectors and turbulence values in a form which are manipulated to be useful for comparative analysis to CFD.

### 3.1 Data Sample Reduction

Up to 25 Megabytes of data was collected per run of the wind tunnel. Running the wind tunnel 1300 times produced a prohibitively large amount of data for analysis. To avoid wasting scarce computer resources, the relevant information from these data files was collected and stored. The technique used to extract the relevant information follows. Mean values of large samples were used to reduce both pressure and hot-film records. The mean is determined by

$$\bar{x} = \frac{1}{N} \sum_{i=1}^N x_i \quad (3.1)$$

where  $N$  is the sample size and  $x$  is the recorded information. Additionally, the fluctuation information from hot-film samples was found with the following relations

$$\overline{x'^2} = \frac{1}{N-1} \sum_{i=1}^N (x_i - \bar{x})^2 \quad (3.2)$$

$$\overline{x'y'} = \frac{1}{N-1} \sum_{i=1}^N (x_i - \bar{x})(y_i - \bar{y}) \quad (3.3)$$

where the former equation is the variance and the latter equation is the covariance between two variables,  $x$  and  $y$ . These sample reduction techniques reduced a total 900 Megabytes of collected data to 11 Megabytes of stored information.

### 3.2 Pressure Probes

The measurement of total pressure behind a normal shock, combined with the measurement of static pressure behind a shock created from a  $10^\circ$  cone, allows determination of the local Mach number in a given flow. The total pressure behind a normal shock ( $P_{t2}$ ) is measured directly, using a Pitot probe. The static pressure behind a shock from a  $10^\circ$  cone ( $P_{cs}$ ) is measured using a  $10^\circ \pm 0.03^\circ$  cone-static probe. Through the manipulation of results from (44, 14) and normal shock relations, the following curve fit was generated by Bowersox (18)

$$\frac{1}{M} = -0.052976 + 4.6840\xi - 18.6786\xi^2 + 50.7006\xi^3 - 54.1577\xi^4 \quad (3.4)$$

where

$$\xi = \frac{P_{t1} P_{cs}}{P_{t2} P_{t1}}$$

Note that the plenum pressure ( $P_{t1}$ ) is introduced to minimize the differences between the two separate tunnel runs required to get the Pitot and cone-static probe data. It has been found for flow angles less than  $6.0^\circ$  that the errors in Mach number are less than 0.3. Also note that Equation 3.4 is valid for Mach numbers in the range from 1.5 to 4.4 and has a standard deviation of 0.06%.

### 3.3 Hot-Film Probes

This section examines multiple overhear (MOH) hot-wire data reduction of Bowersox (17, 18) as an intermediate step to obtaining the single overhear (SOH) reduction equations.

The constant temperature hot-wire anemometer records the voltage required to maintain the wire at a constant known temperature. The power required to maintain this temperature is equivalent to the heat transfer,  $q_w$ , between the hot-wire and the surrounding flow. The Nusselt number, the non-dimensional heat transfer coefficient,

can be related to the heat transfer from the wire by

$$\text{Nu} = \frac{q_w}{\pi k L (T_w - T_e)}$$

where  $k$  is the coefficient of thermal conductivity for the fluid,  $L$  is the wire length,  $T_w$  is the wire temperature and  $T_e$  is the equilibrium temperature or the temperature the unheated wire would approach under these specific flow conditions. The wire temperature is calculated from

$$T_w = T_{ref} + \frac{1}{\tau_{cr} R_{ref}} (R_w - R_{ref}) \quad (3.5)$$

where  $T_{ref}$  is the reference temperature,  $\tau_{cr}$  is the temperature coefficient of resistance (0.0024/K) and  $R_{ref}$  is the reference wire resistance at  $T_{ref}$ . The wire heat transfer rate is equal to the power supplied to the hot-film, or

$$q_w = \mathcal{E}_w i_w = i_w^2 R_w$$

where  $\mathcal{E}_w$  is the wire voltage,  $i_w$  is the current supplied to the hot-wire and  $R_w$  is the wire resistance. The wire current can be related to the wire voltage by

$$i_w = \frac{\mathcal{E}_w}{R_w + R_s + R_L}$$

where  $R_s$  and  $R_L$  are the series and lead resistances, respectively. The coefficient of thermal conductivity is determined from the following curve fit (in  $\frac{W}{mK}$ )

$$k = -5.30377 \cdot 10^{-4} + 1.02108 \cdot 10^{-4} T_t - 4.70285 \cdot 10^{-8} T_t^2 + 1.30279 \cdot 10^{-11} T_t^3$$

The final problem with determining the Nusselt number is the difficulty of measuring the equilibrium temperature. However, where the effective Reynolds number is greater than 20, the difference between  $T_e$  and  $T_t$  is less than 3.0%. This error

can be eliminated if total temperature is consistently substituted for equilibrium temperature in both calibration and data reduction. With the above manipulations in place, the Nusselt number can be found by the following equation

$$\text{Nu} = \frac{\mathcal{E}_w^2 R_w}{\pi k L (T_w - T_t)(R_w + R_s + R_L)^2} \quad (3.6)$$

*3.3.1 Calibration.* It has been determined experimentally that Kings Law, the functional relationship between Nusselt number and effective Reynolds number for incompressible flow, is also an acceptable relationship for compressible flow (45). Kings Law takes the following functional form

$$\text{Nu} = a\sqrt{\text{Re}_e} + b \quad (3.7)$$

The effective Reynolds number is defined in terms of the cosine law by Spangenburg (66) as

$$\text{Re}_e = \frac{\rho U d}{\mu} \cos \phi$$

where  $\rho$  is the freestream density,  $U$  is the magnitude of the velocity,  $d$  is the hot-wire's diameter, and  $\phi$  is the sweep angle of the hot-wire with respect to the flow. To calibrate the hot-film probe, the probe is placed under known conditions and the mass flow is changed by varying total pressure. Mass flow is related to known conditions by a manipulation of isentropic flow and normal shock relations to yield

$$\rho U = P_{t2} M \sqrt{\frac{\gamma}{R T_t} \left(1 + \frac{\gamma - 1}{2} M^2\right)} \left(\frac{2}{(\gamma + 1) M^2}\right)^{\frac{\gamma}{\gamma - 1}} \left(\frac{\gamma + 1}{2\gamma M^2 - \gamma - 1}\right)^{\frac{1}{\gamma - 1}}$$

where  $P_{t2}$  is the total pressure behind a normal shock (Pitot pressure),  $M$  is the Mach number,  $R$  is the gas constant for air and  $\gamma$  is the ratio of specific heats for

air. Viscosity is determined from Sutherland's Law

$$\mu = \frac{1.458 \cdot 10^{-6} T_t^{\frac{3}{2}}}{T_t + 110.40} \quad (3.8)$$

The remaining unknowns in Equation 3.6 are  $a$  and  $b$ , which are determined by linear least squares regression.

**3.3.2 General Theory.** Combining the relationship for Nusselt number (Equation 3.6), Kings Law (Equation 3.7) and substituting for viscosity and thermal conductivity with their turbulent counterparts yields *the thermal anemometry response equation*

$$\frac{\mathcal{E}_w^2}{C_o} = \left(\frac{T_t}{T_o}\right)^{n_k} \left[ a \sqrt{\text{Re}_{e_o}} \left(\frac{T_t}{T_o}\right)^{-n_\mu/2} + b \right] (T_w - T_t) \quad (3.9)$$

where the following relationships are used

$$\begin{aligned} k_t &= k_o \left(\frac{T_t}{T_o}\right)^{n_k}, & n_k &= 0.89, & T_o &= 600K, & k_o &= 45.6 \cdot 10^{-3} \frac{W}{mK} \\ \mu_t &= \mu_o \left(\frac{T_t}{T_o}\right)^{n_\mu}, & n_\mu &= 0.77, & \mu_o &= 30.3 \cdot 10^{-6} \text{Pas} \end{aligned}$$

$$C_o = \frac{(R_w + R_s + R_L)^2}{R_w} \pi L k_o$$

$$\text{Re}_{e_o} = \frac{\rho U d}{\mu_o} \cos \phi$$

Replace  $\mathcal{E}_w$ ,  $\text{Re}_{e_o}$ , and  $T_t$  by their mean and fluctuating components, using the Binomial Theorem, and retain only the first order terms, to obtain

$$\frac{\overline{\mathcal{E}_w^2}}{C_o} = \left(\frac{\overline{T_t}}{T_o}\right)^{n_k} \left[ a \sqrt{\overline{\text{Re}_{e_o}}} + b \right] (T_w - \overline{T_t}) \quad (3.10)$$

Solving for  $\frac{\mathcal{E}_w'}{\mathcal{E}_w}$  the *thermal anemometry fluctuation equation* is given by

$$\frac{\mathcal{E}_w'}{\mathcal{E}_w} = f \left( \frac{\text{Re}_{eo}'}{\text{Re}_{eo}} \right) + g \left( \frac{T_t'}{\overline{T_t}} \right) \quad (3.11)$$

where the *hot-wire sensitivities* for constant temperature anemometry are

$$f = \frac{1}{4} \left( 1 + \frac{b}{a\sqrt{\text{Re}_e}} \right)^{-1} \quad \text{and} \quad g = \frac{-\overline{T_t}}{2(T_w - \overline{T_t})} + \frac{n_k}{2} - f n_\mu \quad (3.12)$$

Squaring Equation 3.11 and averaging yields

$$f_i^2 \overline{\left( \frac{\text{Re}_{eo}'}{\text{Re}_{eo}} \right)^2} + 2f_i g_i \overline{\left( \frac{\text{Re}_{eo}'}{\text{Re}_{eo}} \frac{T_t'}{\overline{T_t}} \right)} + g_i^2 \overline{\left( \frac{T_t'}{\overline{T_t}} \right)^2} = \overline{\left( \frac{\mathcal{E}_w'}{\mathcal{E}_w} \right)_i^2} \quad (3.13)$$

Three overheat ratios are required to solve for the three turbulence terms. The covariance equation is obtained by multiplying Equation 3.11 by itself with each equation representing a separate wire response. Averaging the result provides

$$\begin{aligned} \overline{\left( \frac{\mathcal{E}_w'}{\mathcal{E}_w} \right)_1 \left( \frac{\mathcal{E}_w'}{\mathcal{E}_w} \right)_2} &= f_1 f_2 \overline{\left( \frac{\text{Re}_{eo}'}{\text{Re}_{eo}} \right)_1 \left( \frac{\text{Re}_{eo}'}{\text{Re}_{eo}} \right)_2} + g_1 g_2 \overline{\left( \frac{T_t'}{\overline{T_t}} \right)} \\ &\quad + f_1 g_2 \overline{\left( \frac{\text{Re}_{eo}'}{\text{Re}_{eo}} \frac{T_t'}{\overline{T_t}} \right)_1} + f_2 g_1 \overline{\left( \frac{\text{Re}_{eo}'}{\text{Re}_{eo}} \frac{T_t'}{\overline{T_t}} \right)_2} \end{aligned} \quad (3.14)$$

**3.3.3 Coordinate Transformation.** The response of the cross-wires is independent of Mach number for  $M \sin \phi \geq 1$ . The effective Reynolds number must be transformed to tunnel coordinates through oblique shock relations

$$\begin{Bmatrix} \text{Re}_n \\ \text{Re}_t \end{Bmatrix} = \begin{bmatrix} \cos \phi & \sin \phi \\ -\sin \phi & \cos \phi \end{bmatrix} \begin{Bmatrix} \text{Re}_x \\ \text{Re}_y \end{Bmatrix} \quad (3.15)$$



The effective Reynolds number becomes

$$\begin{aligned} \text{Re}_e^2 &= \text{Re}_n^2 + k_c^2 \text{Re}_t^2 \\ &= A_1 \text{Re}_x^2 + 2A_2 \text{Re}_x \text{Re}_y + A_3 \text{Re}_y^2 \end{aligned} \quad (3.16)$$

where  $A_i$  are given by

$$\begin{aligned} A_1 &= \cos^2 \phi + k_c^2 \sin^2 \phi \\ A_2 &= (1 - k_c^2) \cos \phi \sin \phi \\ A_3 &= k_c^2 \cos^2 \phi + \sin^2 \phi \end{aligned} \quad (3.17)$$

and  $k_c$  is

$$k_c = \frac{\overline{\rho_1}}{\rho_2} k \quad (3.18)$$

where  $k = \text{fcn}(L/d)$ . For this experiment,  $L/d = 19.61$ , which relates to  $k \approx 0.50$ . However, since the flow angles variance is small between calibration and data recording ( $\pm 10.0^\circ$ ),  $k$  was set to zero in both calibration and reduction. This was done consistently to calibration and data reduction, thus minimizing the associated error.

Replacing  $\text{Re}_{e_o}$ ,  $\text{Re}_{x_o}$  and  $\text{Re}_{y_o}$  by their mean and fluctuating components, applying the binomial theorem, and using

$$\begin{aligned} R_o &= \frac{\overline{\text{Re}_{y_o}}}{\overline{\text{Re}_{x_o}}} = \overline{\rho v} / \overline{\rho u} \\ B_1 &= \frac{A_1}{B_3} \\ B_2 &= \frac{A_2}{B_3} \\ B_3 &= A_1 + 2A_2 R_o \end{aligned} \quad (3.19)$$

the following can be shown

$$\overline{\text{Re}_{e_{oj}}} = \overline{\text{Re}_{x_o}} \sqrt{B_{3j}} \quad (3.20)$$

and

$$\left( \frac{\text{Re}_{e_o}'}{\overline{\text{Re}_{e_o}}} \right)_j = B_{1j} \left( \frac{\text{Re}_{x_o}'}{\overline{\text{Re}_{x_o}}} \right) + B_{2j} \left( \frac{\text{Re}_{y_o}'}{\overline{\text{Re}_{x_o}}} \right) \quad (3.21)$$

where the index  $j$  sums over the two wires on the cross-wire probe. Solving this set of equations and transforming into  $x$  and  $y$  components

$$\overline{Re_{x_o}}^{-2} = \frac{\overline{Re_{e_{o1}}}^2/A_{21} - \overline{Re_{e_{o2}}}^2/A_{22}}{A_{11}/A_{21} - A_{12}/A_{22}}$$

$$\overline{Re_{y_o}} = \frac{1}{2\overline{Re_{x_o}}} \frac{\overline{Re_{e_{o1}}}^2/A_{11} - \overline{Re_{e_{o2}}}^2/A_{12}}{A_{21}/A_{11} - A_{22}/A_{12}}$$

Squaring Equation 3.21 and averaging results in Equations 3.22 and 3.23. Note that  $D_1 = (B_{21}/B_{11} - B_{22}/B_{12})$  and  $D_2 = (B_{11}/B_{21} - B_{12}/B_{22})$ .

$$\overline{\left(\frac{Re_{x_o}'}{\overline{Re_{x_o}}}\right)^2} = \frac{1}{D_2^2} \left[ \frac{1}{B_{21}^2} \overline{\left(\frac{Re_{e_o}'}{\overline{Re_{e_o}}}\right)_1^2} - \frac{2}{B_{21}B_{22}} \overline{\left(\frac{Re_{e_o}'}{\overline{Re_{e_o}}}\right)_1 \left(\frac{Re_{e_o}'}{\overline{Re_{e_o}}}\right)_2} + \frac{1}{B_{22}^2} \overline{\left(\frac{Re_{e_o}'}{\overline{Re_{e_o}}}\right)_2^2} \right] \quad (3.22)$$

$$\overline{\left(\frac{Re_{y_o}'}{\overline{Re_{x_o}}}\right)^2} = \frac{1}{D_1^2} \left[ \frac{1}{B_{11}^2} \overline{\left(\frac{Re_{e_o}'}{\overline{Re_{e_o}}}\right)_1^2} - \frac{2}{B_{11}B_{12}} \overline{\left(\frac{Re_{e_o}'}{\overline{Re_{e_o}}}\right)_1 \left(\frac{Re_{e_o}'}{\overline{Re_{e_o}}}\right)_2} + \frac{1}{B_{12}^2} \overline{\left(\frac{Re_{e_o}'}{\overline{Re_{e_o}}}\right)_2^2} \right] \quad (3.23)$$

Multiplying two forms of Equation 3.21 together – one for each hot-wire response – then averaging the resulting equation, results in the covariance response, Equation 3.24.

$$\overline{\left(\frac{Re_{x_o}'}{\overline{Re_{x_o}}} \frac{Re_{y_o}'}{\overline{Re_{x_o}}}\right)} = \frac{1}{2B_{11}B_{21}} \left[ \overline{\left(\frac{Re_{e_o}'}{\overline{Re_{e_o}}}\right)_1^2} - B_{11}^2 \overline{\left(\frac{Re_{x_o}'}{\overline{Re_{x_o}}}\right)^2} + B_{21}^2 \overline{\left(\frac{Re_{y_o}'}{\overline{Re_{x_o}}}\right)^2} \right] \quad (3.24)$$

To analyze the results from the u-w hot-film probe, replace  $v$  by  $w$ , replace  $y$  with  $z$  and change the sign of the sine terms in the transformation matrix.

**3.3.4 Single Overheat Analysis.** Sensitivity to total temperature fluctuation is generally negligible for hot-wires operating at high overheat ratios ( $\frac{R_w}{R_{ref}} \geq 2.0$ ). The AFIT Mach 2.9 test facility has been found to maintain total temperature fluctuation below about 2.0% (52, 24, 51). The following section describes the analysis method used for SOH measurements.

The Strong Reynolds Analogy is used to correct for the total temperature sensitivity of the probe. When total-temperature fluctuations are neglected, Morkovin (57) states that the temperature fluctuation can be represented by

$$\frac{T'}{\bar{T}} = -(\gamma - 1)M^2 \left( \frac{u'}{\bar{u}} + R_o \frac{v'}{\bar{u}} \right) \quad (3.25)$$

Bowersox (17) postulates that when  $Pr \neq 1$  and  $T'_t \neq 0$  then the temperature fluctuations can be represented by

$$\frac{T'}{\bar{T}} = -\kappa(\gamma - 1)M^2 \left( \frac{u'}{\bar{u}} + R_o \frac{v'}{\bar{u}} \right) \quad (3.26)$$

where  $\kappa$  ranges from 0.3 to 0.5. Defining  $\theta = -\kappa(\gamma - 1)M^2$ , where  $R_o^2\theta \ll 1$  and  $R_o^2\theta^2 \ll 1 - \theta$ , then

$$\frac{u'}{\bar{u}} = \frac{1}{1 - \theta} \left[ \frac{(\rho u)'}{\bar{\rho u}} + R_o \frac{(\rho v)'}{\bar{\rho u}} \right] \quad (3.27)$$

$$\frac{v'}{\bar{u}} = \frac{R_o}{1 - \theta} \frac{(\rho u)'}{\bar{\rho u}} + \frac{(\rho v)'}{\bar{\rho u}} \quad (3.28)$$

The total temperature fluctuation has become a function of the mass-flux

$$\frac{T'_t}{\bar{T}_t} = \frac{\beta + \alpha\theta}{1 - \theta} \left[ \frac{(\rho u)'}{\bar{\rho u}} + R_o \frac{(\rho v)'}{\bar{\rho u}} \right] \quad (3.29)$$

Setting  $k_c = 0$  results in an alteration of the transformation coefficients  $A_i$

$$\begin{aligned} A_1 &= \cos^2 \phi \\ A_2 &= \cos \phi \sin \phi \\ A_3 &= \sin^2 \phi \end{aligned} \quad (3.30)$$

Inserting the assumption that  $\frac{T'_t}{\bar{T}_t} = 0$  alters Equations 3.13 and 3.14 as follows

$$\overline{\left( \frac{\text{Re}_{e_o}'}{\bar{\text{Re}_{e_o}}} \right)^2} = \frac{1}{f_i^2} \overline{\left( \frac{\mathcal{E}_w}{\bar{\mathcal{E}_w}} \right)^2}_i \quad (3.31)$$

$$\overline{\left(\frac{\text{Re}_{e_o}'}{\text{Re}_{e_o}}\right)}_1 \overline{\left(\frac{\text{Re}_{e_o}'}{\text{Re}_{e_o}}\right)}_2 = \frac{1}{f_1 f_2} \overline{\left(\frac{\mathcal{E}_w'}{\mathcal{E}_w}\right)}_1 \overline{\left(\frac{\mathcal{E}_w'}{\mathcal{E}_w}\right)}_2 \quad (3.32)$$

Bowersox, Miller and McCann (17, 52, 24, 51) have determined experimentally that the data reduction is unaffected by neglecting the Strong Reynolds Analogy. Therefore,  $\kappa$  is set to 1.0 which implies  $\beta = -\alpha\theta$ . The above assumptions are applied and reduce the transformation to

$$\begin{bmatrix} f_1^2 B_{11}^2 & 2f_1^2 B_{11} B_{21} & f_1^2 B_{21}^2 \\ f_2^2 B_{12}^2 & 2f_2^2 B_{12} B_{22} & f_2^2 B_{22}^2 \\ f_1 f_2 B_{11} B_{12} & f_1 f_2 (B_{11} B_{22} + B_{12} B_{21}) & f_1 f_2 B_{21} B_{22} \end{bmatrix} \begin{Bmatrix} \overline{\left(\frac{\text{Re}_{x_o}'}{\text{Re}_{x_o}}\right)}^2 \\ \frac{\overline{\text{Re}_{x_o}'} \overline{\text{Re}_{y_o}'}}{\overline{\text{Re}_{x_o}} \overline{\text{Re}_{x_o}}} \\ \overline{\left(\frac{\text{Re}_{y_o}'}{\text{Re}_{x_o}}\right)}^2 \end{Bmatrix} \quad (3.33)$$

$$= \begin{Bmatrix} \overline{\left(\frac{\mathcal{E}_w'}{\mathcal{E}_w}\right)}_1^2 \\ \overline{\left(\frac{\mathcal{E}_w'}{\mathcal{E}_w}\right)}_2^2 \\ \overline{\left(\frac{\mathcal{E}_w'}{\mathcal{E}_w}\right)}_1 \overline{\left(\frac{\mathcal{E}_w'}{\mathcal{E}_w}\right)}_2 \end{Bmatrix}$$

Or substituting the results from Equations 3.31 and 3.32 into Equations 3.22, 3.23 and 3.24 yields

$$[S_{ij}]^{-1} \begin{Bmatrix} \overline{\left(\frac{\mathcal{E}_w'}{\mathcal{E}_w}\right)}_1^2 \\ \overline{\left(\frac{\mathcal{E}_w'}{\mathcal{E}_w}\right)}_2^2 \\ \overline{\left(\frac{\mathcal{E}_w'}{\mathcal{E}_w}\right)}_1 \overline{\left(\frac{\mathcal{E}_w'}{\mathcal{E}_w}\right)}_2 \end{Bmatrix} = \begin{Bmatrix} \overline{\left(\frac{\text{Re}_{x_o}'}{\text{Re}_{x_o}}\right)}^2 \\ \frac{\overline{\text{Re}_{x_o}'} \overline{\text{Re}_{y_o}'}}{\overline{\text{Re}_{x_o}} \overline{\text{Re}_{x_o}}} \\ \overline{\left(\frac{\text{Re}_{y_o}'}{\text{Re}_{x_o}}\right)}^2 \end{Bmatrix} = \begin{Bmatrix} \overline{\left(\frac{(\rho u)'}{\rho u}\right)}^2 \\ \frac{\overline{(\rho u)'} \overline{(\rho v)'}}{\overline{\rho u} \overline{\rho u}} \\ \overline{\left(\frac{(\rho v)'}{\rho u}\right)}^2 \end{Bmatrix} \quad (3.34)$$

where  $[S_{ij}]^{-1}$  is

$$\begin{bmatrix} \frac{1}{D_2^2 B_{21}^2 f_1^2} & \frac{1}{D_2^2 B_{22}^2 f_2^2} & \frac{1}{D_2^2 B_{21} B_{22} f_1 f_2} \\ \frac{1}{2B_{11} B_{21} f_1^2} \left( \frac{B_{21}^2}{B_{11}^2 D_1^2} - \frac{B_{11}^2}{B_{21}^2 D_2^2} + 1 \right) & \frac{1}{2B_{11} B_{21} f_2^2} \left( \frac{B_{21}^2}{B_{12}^2 D_1^2} - \frac{B_{11}^2}{B_{22}^2 D_2^2} \right) & \frac{1}{B_{11} B_{21} f_1 f_2} \left( \frac{B_{21}^2}{B_{11} B_{12} D_1^2} - \frac{B_{11}^2}{B_{21} B_{22} D_2^2} \right) \\ \frac{1}{D_1^2 B_{11}^2 f_1^2} & \frac{1}{D_1^2 B_{12}^2 f_2^2} & \frac{1}{D_1^2 B_{11} B_{22} f_1 f_2} \end{bmatrix}$$

**3.3.5 Separation of Turbulence Variables.** One of the key features of cross-wire anemometry is that the Reynolds turbulent shear stress can be directly measured as the negative of the mass-flux correlation term combined with the density fluctuation as shown below (20)

$$\frac{\tau_{xy_T}^r}{\rho u^2} = -\frac{(\rho u)' (\rho v)'}{(\rho u)^2} + R_o \overline{\left( \frac{\rho'}{\rho} \right)^2} \quad (3.35)$$

The density fluctuation cannot be directly measured from the cross-wire probe, and must be reduced by neglecting pressure and temperature fluctuations. Since this term is squared and multiplied by  $R_o$ , it is negligible. Therefore an error in density fluctuation caused by the assumptions used in data reduction will only produce a very small error in Reynolds turbulent shear stress.

Additional relationships for separation of conservative hot-wire variables into primitive turbulence variables are

$$\frac{\rho'}{\bar{\rho}} = \frac{1}{\alpha + \beta} \left[ \beta \left( \frac{(\rho u)'}{\bar{\rho} u} + R_o \frac{(\rho v)'}{\bar{\rho} u} \right) - \frac{T_t'}{\bar{T}_t} + \alpha \frac{p'}{\bar{p}} \right] \quad (3.36)$$

$$\frac{u'}{\bar{u}} = \frac{(\rho u)'}{\bar{\rho} u} - \frac{\rho'}{\bar{\rho}} \quad (3.37)$$

$$\frac{v'}{\bar{u}} = \frac{(\rho v)'}{\bar{\rho} u} - R_o \frac{\rho'}{\bar{\rho}} \quad (3.38)$$

where

$$\alpha = [1 + \frac{1}{2}(\gamma - 1)M^2]^{-1} \quad \text{and} \quad \beta = (\gamma - 1)\alpha M^2$$

Kistler (42) suggests  $p'$  is proportional to  $u'^2$ . Therefore,  $p'$  is neglected as it is like a second order term. Note that the pressure fluctuation is multiplied by  $\alpha$ , which is near  $\frac{1}{3}$  in the Mach regime of this study. This results in a small effect on the reduction of the density fluctuation. Bowersox and Schetz (20) have experimentally verified the validity of neglecting the effect of  $p'$  in hot-wire analysis for a Mach 4.0 free mixing layer. After neglecting  $T'_t$  and  $p'$ , Equation 3.37 reduces to

$$\frac{\rho'}{\bar{\rho}} = \frac{\beta}{\alpha + \beta} \left( \frac{(\rho u)'}{\bar{\rho} \bar{u}} + R_o \frac{(\rho v)'}{\bar{\rho} \bar{u}} \right) \quad (3.39)$$

Placing the previous three equations in terms of the already determined cross-wire conservative fluctuating terms, and noting that  $R_o \ll 1$  (neglecting third order terms) the incompressible fluctuation equations become

$$\sqrt{\overline{\left(\frac{\rho'}{\bar{\rho}}\right)^2}} = \frac{\beta}{\alpha + \beta} \sqrt{\overline{\left(\frac{(\rho u)'}{\bar{\rho} \bar{u}}\right)^2}} \quad (3.40)$$

$$\sqrt{\overline{\left(\frac{u'}{\bar{u}}\right)^2}} = \frac{\alpha}{\alpha + \beta} \sqrt{\overline{\left(\frac{(\rho u)'}{\bar{\rho} \bar{u}}\right)^2}} \quad (3.41)$$

$$\sqrt{\overline{\left(\frac{v'}{\bar{u}}\right)^2}} = \sqrt{\overline{\left(\frac{(\rho v)'}{\bar{\rho} \bar{u}}\right)^2} - 2R_o \frac{\alpha}{\alpha + \beta} \frac{(\rho u)'}{\bar{\rho} \bar{u}} \frac{(\rho v)'}{\bar{\rho} \bar{u}}} \quad (3.42)$$

After neglecting total temperature and pressure fluctuations, the cross-correlation terms are determined as follows

$$\frac{\overline{u'v'}}{\bar{u}^2} = \frac{1}{\alpha + \beta} \left[ \alpha \frac{(\rho u)'}{\bar{\rho} \bar{u}} \frac{(\rho v)'}{\bar{\rho} \bar{u}} - R_o \frac{\alpha^2}{\alpha + \beta} \overline{\left(\frac{(\rho u)'}{\bar{\rho} \bar{u}}\right)^2} \right] \quad (3.43)$$

$$\frac{\overline{\rho' u'}}{\bar{\rho} \bar{u}} = \frac{\alpha \beta}{(\alpha + \beta)^2} \overline{\left(\frac{(\rho u)'}{\bar{\rho} \bar{u}}\right)^2} \quad (3.44)$$

$$\frac{\overline{\rho' v'}}{\bar{\rho} \bar{u}} = \frac{\beta}{\alpha + \beta} \left[ \frac{(\rho u)'}{\bar{\rho} \bar{u}} \frac{(\rho v)'}{\bar{\rho} \bar{u}} - R_o \alpha \overline{\left(\frac{(\rho u)'}{\bar{\rho} \bar{u}}\right)^2} \right] \quad (3.45)$$

The Reynolds turbulent shear stress is then calculated by

$$\frac{\tau_{xy_T}^r}{\rho u^2} = \frac{\overline{u'v'}}{\bar{u}^2} - \frac{\overline{\rho'v'}}{\bar{\rho}\bar{u}} - R_o \frac{\overline{\rho'u'}}{\bar{\rho}\bar{u}} \quad (3.46)$$

This method of calculation is mathematically equivalent to Equation 3.35. However, it is provided as a determination of the errors generated in the process of separating the fluctuating variables.

The variables conserved in the Favré-averaged Navier-Stokes equations are available for comparison as well. The Favré variables are available by way of the following transformations

$$\tilde{u} = \overline{\rho u} / \bar{\rho} \quad (3.47)$$

$$\frac{\overline{u''}}{\tilde{u}} = - \frac{\overline{\rho' u'}}{\bar{\rho} \bar{u}} \quad (3.48)$$

$$\frac{\overline{v''}}{\tilde{u}} = - \frac{\overline{\rho' v'}}{\bar{\rho} \bar{u}} \quad (3.49)$$

$$\overline{\rho u'' v''} \approx \bar{\rho} \overline{u' v'} \quad (3.50)$$

The Favré form of the turbulent shear stress is related to cross-correlations in velocity by the following expression

$$\frac{\tau_{xy_T}^f}{\rho u^2} = - \frac{\overline{u' v'}}{\bar{u}^2} \quad (3.51)$$

## IV. Results and Discussion

This chapter details the results achieved from the mapping of the flowfield about the wrap-around fin (WAF). A coordinate system is defined from the nozzle throat, shown in Figure 4.1. All plots in this section are based on this coordinate system and are non-dimensionalized by the fin radius ( $r = 1.5875\text{cm}$ ).

### 4.1 Inlet Plane

The test section in which the WAF is tested is removable and is mated to the nozzle by a series of allen screws. Small seams are present between components of the tunnel, due to its modular design. These seams caused a series of weak shocks and expansions which travelled into the test section. Figure 4.2 are contours of the mass-flux in the streamwise direction, which shows a series of these shocks and expansions in the test section inlet. The mass-flux contours in this figure were closely spaced about the freestream mean to bring out the shock/expansion detail. A sketch of the inlet flow structure is shown in Figure 4.3. Although numerous shocks and expansions exist in the inlet, these structures were weak. The negligible secondary-flow created by these seams is shown in Figure 4.4 in the form of mass-flux vectors.

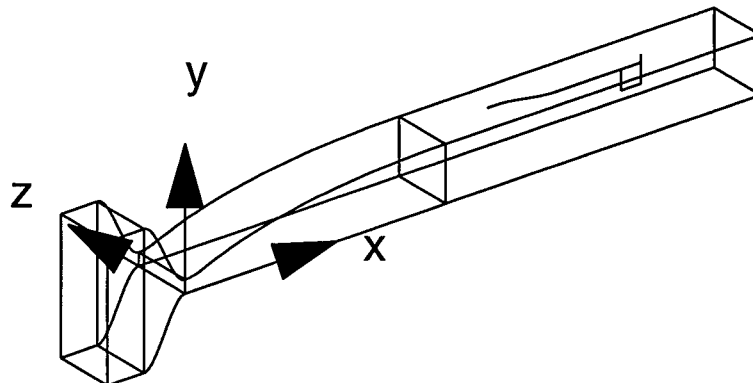


Figure 4.1 Reference Coordinate System



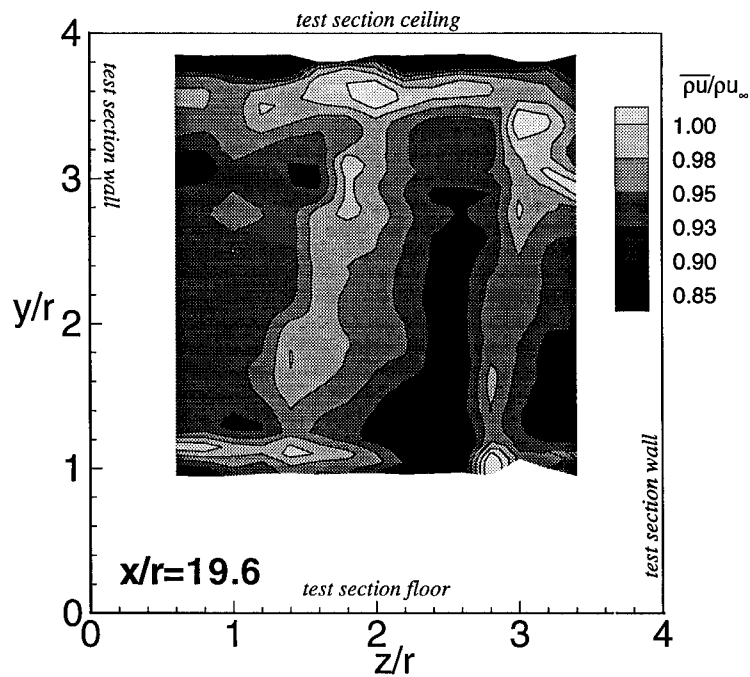


Figure 4.2 Inlet Plane Mass-Flux Contours

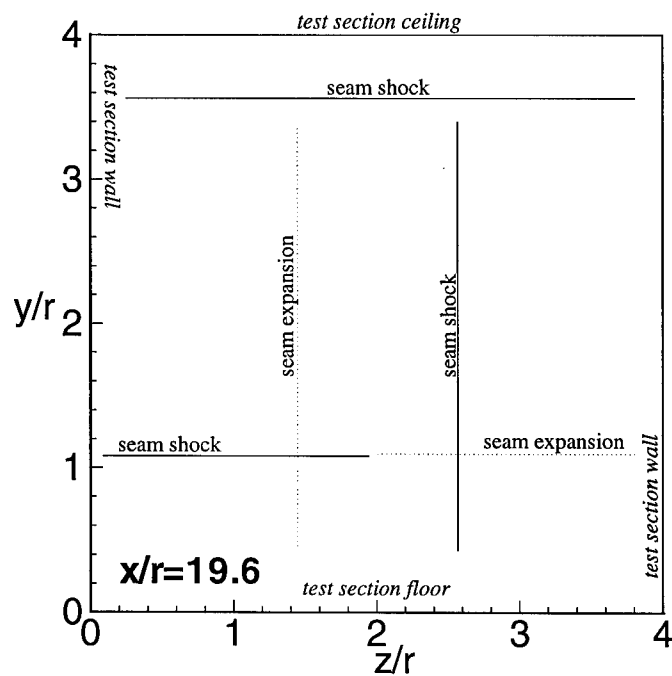


Figure 4.3 Inlet Seam Shock/Expansion Pattern

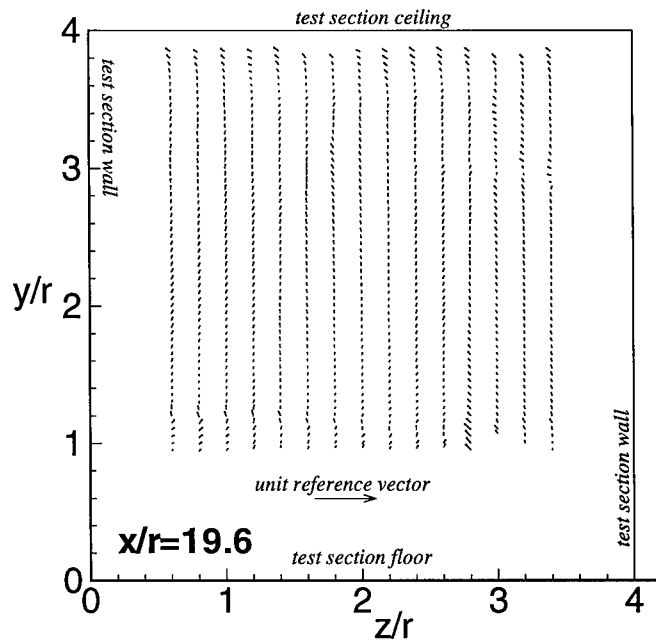


Figure 4.4 Secondary-Flow at Inlet

Note the mass-flux contours of Figure 4.2 are, in general, less than 1.0 when non-dimensionalized by the freestream reference mass-flux. The freestream values are defined based on plenum (settling chamber) conditions and the mean Mach number at the test section inlet. The variation in Mach number at the inlet to the test section is given in Figure 4.5. The mean Mach number is defined as the average of the Mach values obtained from the center quarter of the inlet plane ( $\frac{z}{r} = 19.6$ ). Then assuming the total temperature measured in the plenum to be the same value at the test section inlet, the freestream static temperature is determined. The static pressure is calculated using the freestream Mach number and the Pitot pressure. Using this information in concert with the equation of state for a perfect gas provides the freestream density. The freestream speed of sound is determined from the static temperature, which in turn yields the freestream flow speed. The freestream Reynolds number is then calculated. Table 4.1 summarizes the freestream and plenum conditions.

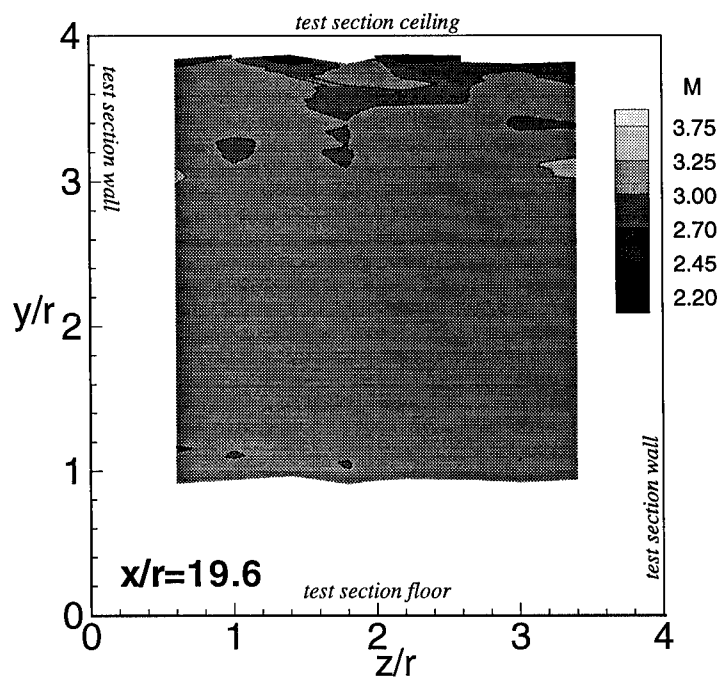


Figure 4.5 Inlet Mach Contours

Table 4.1 Tunnel Inflow Conditions

Condition	Value
$T_{t_{plenum}}$	297K
$P_{t_{plenum}}$	2.07atm
$T_{inlet}$	113K
$P_{inlet}$	0.065atm
$\rho_{inlet}$	$0.220 \frac{\text{Kg}}{\text{m}^3}$
$u_{inlet}$	$608 \frac{\text{m}}{\text{s}}$
$M_{\infty}$	2.85
$\text{Re}_{\infty}$	$1.70 \frac{1}{\text{m}}$

## 4.2 Blending Region

A truncated section of the model was designed based upon WAF missiles that are currently undergoing flight tests at the instrumented test range at Eglin Air Force Base. While a smaller scale missile of full configuration could have been tested in the AFIT supersonic test facility, the size of the smaller scale missile fins would have reduced the experimental mapping resolution. To simulate the full missile body, the aft section of the missile was blended to the tunnel ceiling. The length of the full missile cylinder was reduced by introducing a tapered region - designed to produce a weak shock coalescence. The coalescing shock is visible in the center of the shadowgraph of Figure 4.6 as the shock moving away from the WAF model (shown on the bottom of the photo).

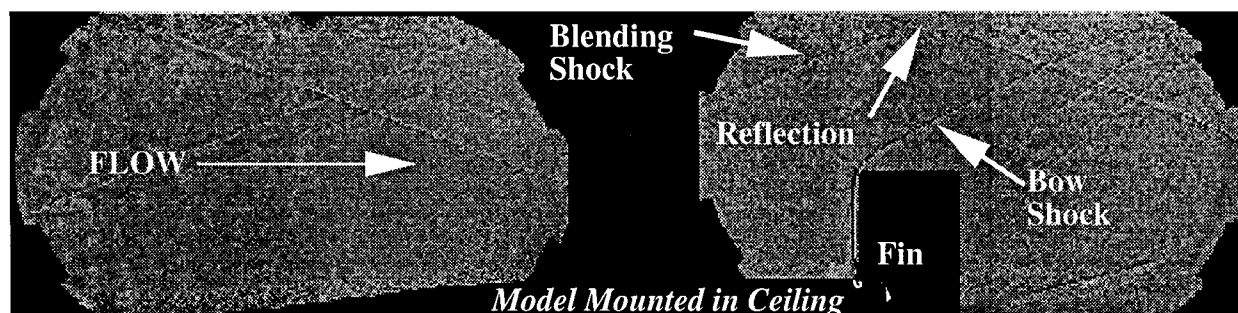


Figure 4.6 Composite Shadowgraph Image of WAF Model

Notice how the coalescing shock reflected off of the tunnel floor (shown on the top of the photo) in the schlieren image in Figure 4.7. Two-dimensional oblique shock theory was used to place the shock in this position. The location of the shock was downstream of oblique shock theory and the intensity of the shock was much less than theory due to a smooth blending region and three-dimensional relieving effects. The lower intensity shock results in minimal changes to the flow qualities.

Figure 4.8 shows the density field over a cutting plane in the center of the blending region. The lighter region spanning the test section was the coalescing shock formed from the blending forebody.

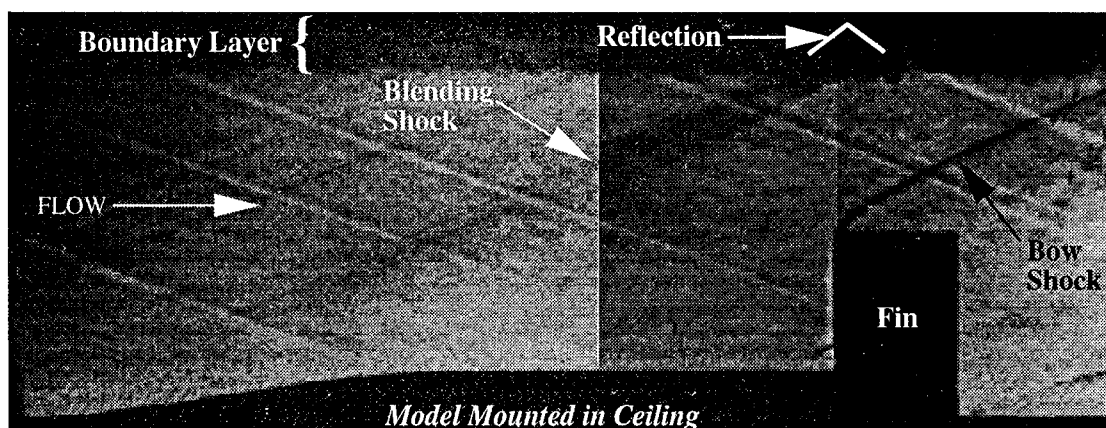


Figure 4.7 Composite Schlieren Photograph of WAF Model

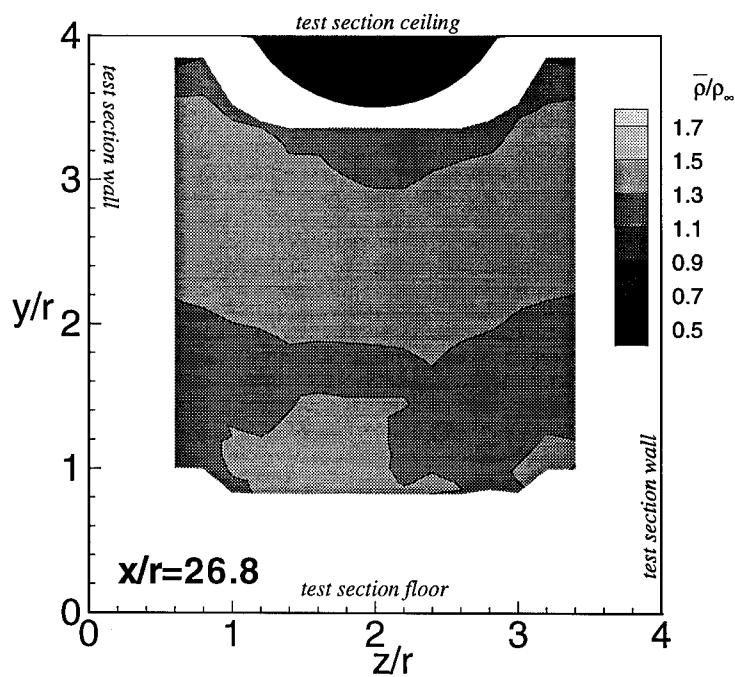


Figure 4.8 Density Contours of Blending Region

Reversing the knife edge in a schlieren image produces the negative of the previous image (Figure 4.7), as shown in Figure 4.9. This figure highlights the boundary layer on the tunnel floor (shown on the top of the photo). A series of shocks are also visible extending from the top of the photo downward. These weak disturbances are created by seams associated with removable plugs. In this schlieren image these seam shocks appear to be much stronger than the blending shock. However, measurements presented in Figure 4.10 indicate that the plug-seam shocks are of lower strength than the blending shock and are weaker than the bow shock. The relative intensity of the shocks is best visualized in the shadowgraph photo. Clearly the crisp and intense character of the bow shock suggests it provides the strongest influence on the WAF flowfield. The shock structure in the test section is summarized in Figure 4.11.

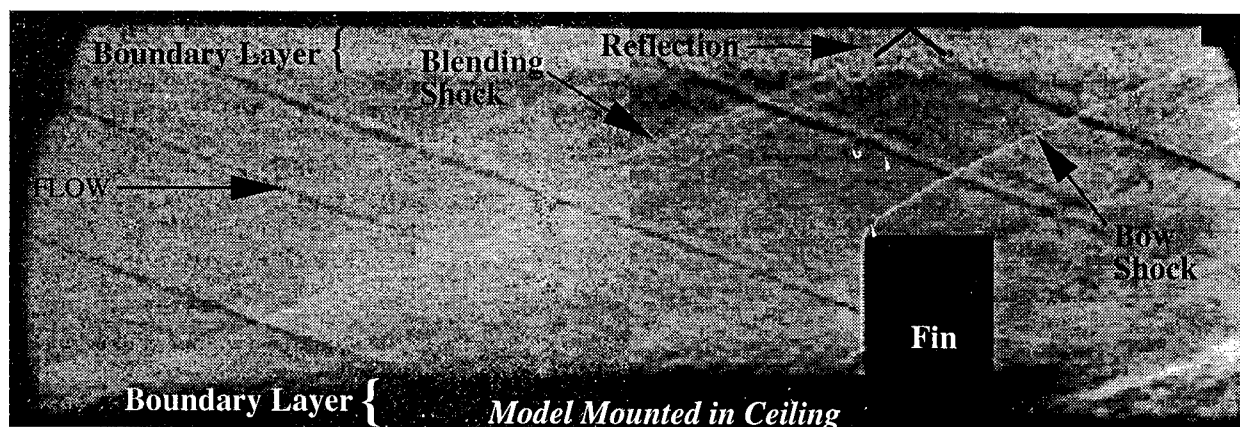


Figure 4.9 Reversed Knife-Edge Schlieren of WAF Model

### 4.3 Wrap-Around Fin Region

A majority of the data collection process for this experiment was involved in mapping the flowfield in close vicinity to the WAF. The hot-film probes used for this effort were very fragile. The probe was destroyed if it brushed against the model. When the tunnel was in operation, the hot-film probe would flex more than 1mm vertically (towards the model). To avoid probe contact, the probes were initially

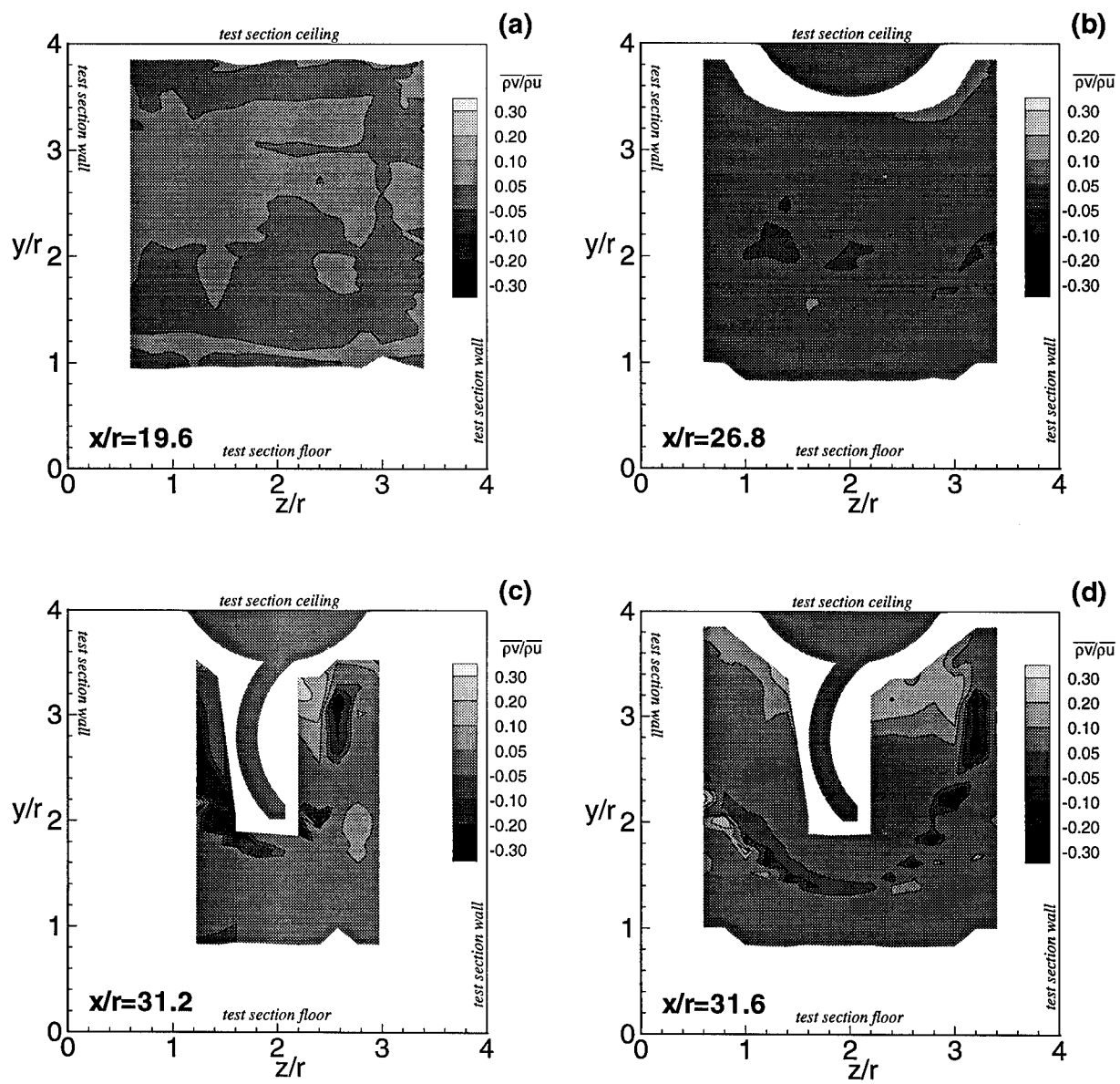


Figure 4.10 Comparison of Shock Intensity with Spanwise Mass-Flux Contours

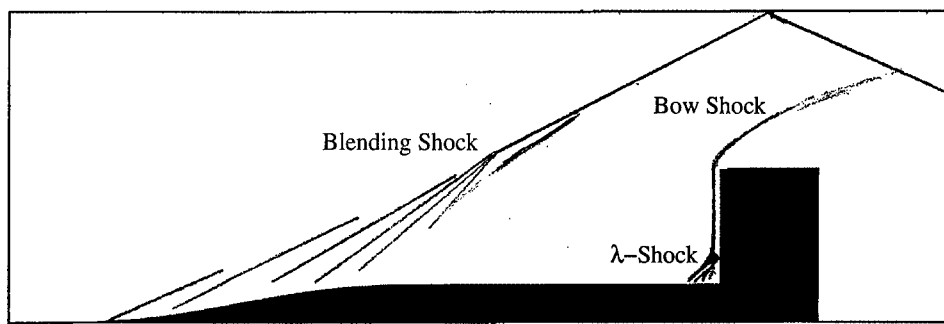


Figure 4.11 Overall Shock Structure

positioned at a minimum distance of 2mm from the model. This limitation made it impossible to examine the boundary layer near the WAF or the juncture of the WAF to the half-cylinder body.

*4.3.1 Fin-Body Juncture.* Despite the lack of quantitative measurements at the intersection of the fin to the forebody, a variety of qualitative measurements were made. A detailed shadowgraph image is shown in Figure 4.12. The  $\lambda$ -shock structure visualized in the shadowgraph has been seen in similar juncture studies (8, 77, 29). Figure 4.13 is a schematic of the flowfield at the fin-body juncture.

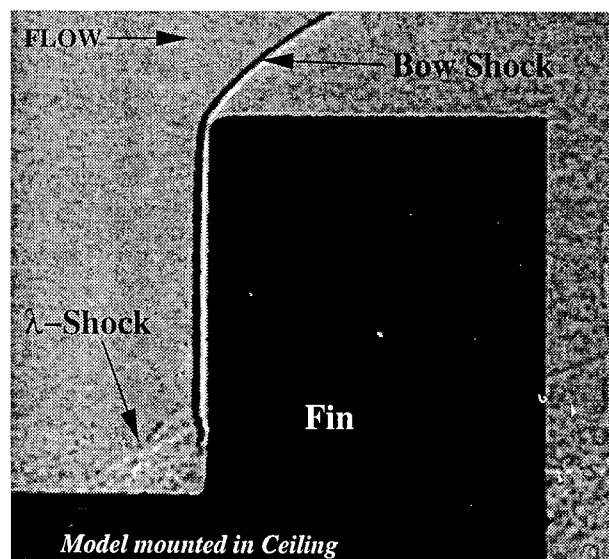


Figure 4.12 Magnified View of Shadowgraph Near the WAF



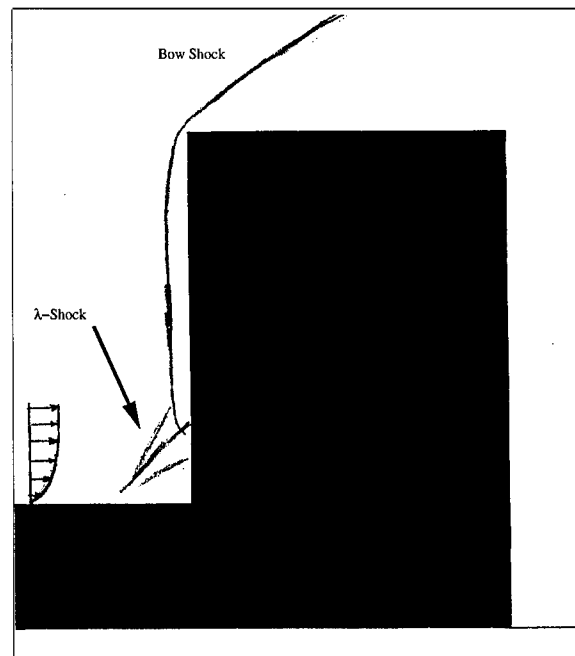


Figure 4.13 Shock Structure at Fin-Body Junction

Fomison (29) and Williams, Harloff and Gessner (77) looked at the vortex structure about fin-like junctures with flat plates as illustrated in Figures 4.14 and 4.15 from Fomison. Oil flow visualization techniques suggest that one vortex exists in the separation region under the  $\lambda$ -shock on the missile body. Figures 4.16 and 4.17 are photos taken of the oil-flow streakline visualization. Patterns seen in these photographs show the vortex on the convex side of the WAF being much farther away from the model centerline than the vortex on the concave side. The postulated vortex structure is diagrammed in Figure 4.18.

*4.3.2 Bow Shock Region.* The flowfield surrounding a WAF fin differs significantly from the flow structure present about straight fins. An asymmetric bow shock envelops the WAF as shown in Figure 4.19. The structure on the concave side of the fin is markedly different than the flow structure on the convex side. Figures 4.20 and 4.21 show this structure in Mach number contours progressing past the fin. The convex side of the fin is marked by a large, sweeping shock followed by an expansion. A series of contour composite-images provide a better overall description

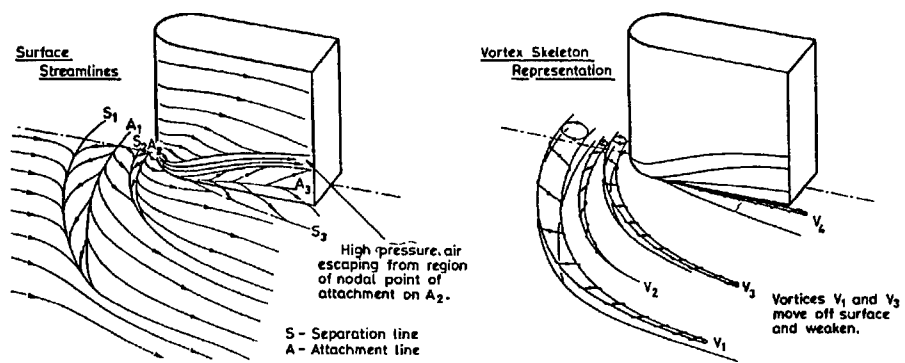


Figure 4.14 Blunt Fin, Fin-Juncture Flow (Fomison,1986)

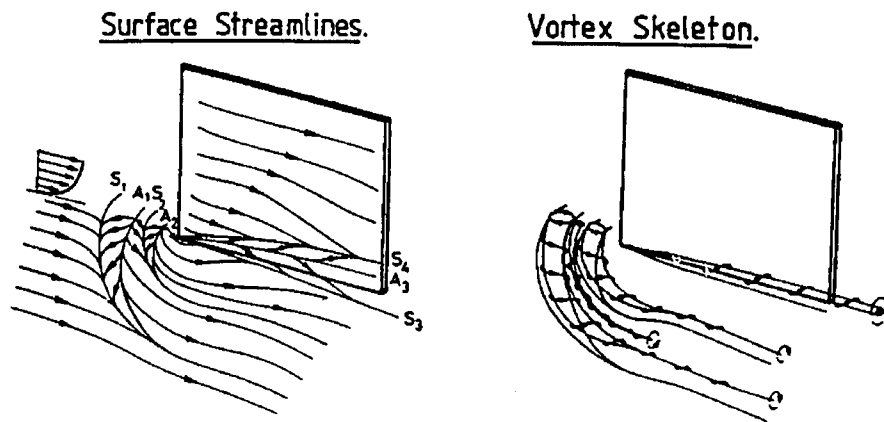


Figure 4.15 Thin Fin, Fin-Juncture Flow (Fomison,1986)

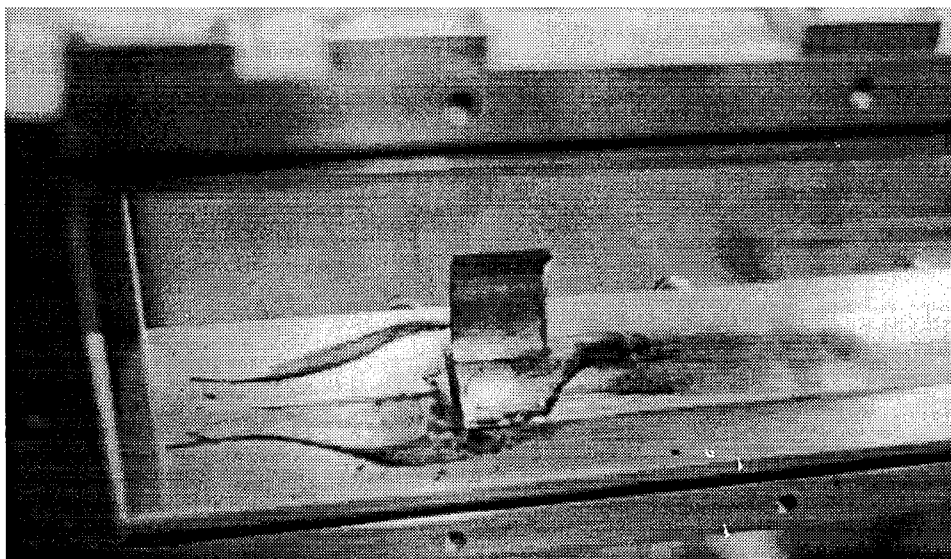


Figure 4.16 Oil Flow Visualization on the WAF Model, Concave Side

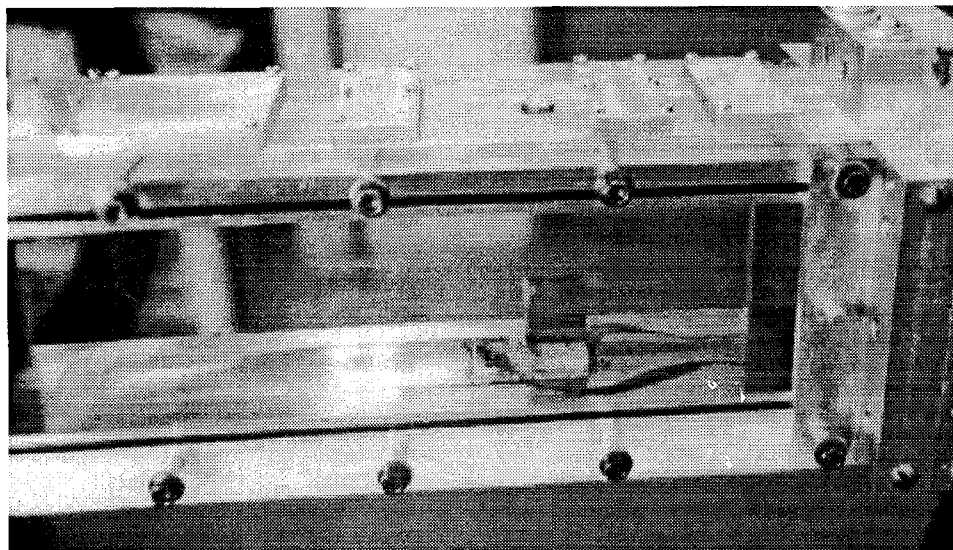


Figure 4.17 Oil Flow Visualization on the WAF Model, Convex Side

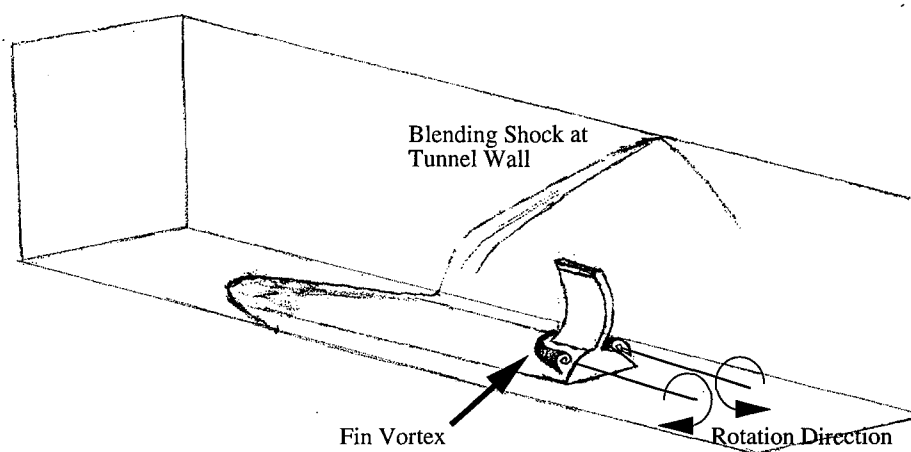


Figure 4.18 Cartoon of the Vortex Structure about the Fin

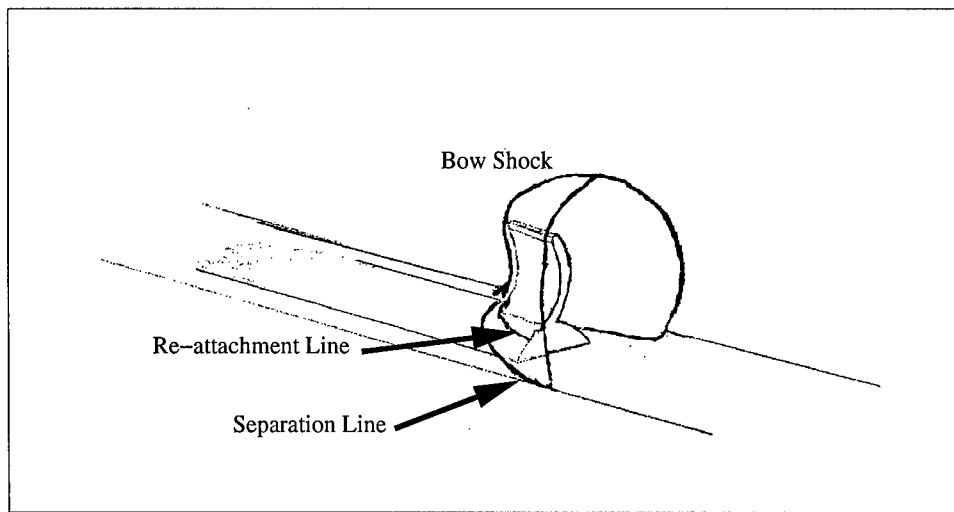


Figure 4.19 Bow Shock Structure

of the shock structure, shown in Figures 4.22, 4.23 and 4.24. Figure 4.22 shows how the Mach number drops on the compressive side of the fin, while the flow accelerates through the expansion in Figure 4.23. The bow-shock is shown from multiple cuts of mass-flux contours in Figure 4.24. Finally, vertical cutting planes of streamlines show the shock progression from the tip toward the base in Figure 4.25.

A numerical study by Abate and Cook (9) proposed that the convex side of the WAF expands the flow, while the concave side compresses the flow. The current experimental effort supports that conclusion. Figure 4.26 contours the static pressure in a progression of planes, moving downstream. The expansion shows up in subplot (d) vividly as the low pressure section running the length of the convex side of the fin. The compression of the concave side is illustrated in all of the subfigures as the elliptical high pressure region just outboard of the fin.

The shock on the concave side of the WAF stays very close to the WAF surface, while the shock on the convex side moves out of the probe mapping range quickly. Numerical studies of similar WAF configurations show good agreement with this structure (7, 9, 70). In particular, Tilmann (70) contains an inviscid numerical simulation of this WAF model run under similar freestream conditions. Figure 4.27 is a

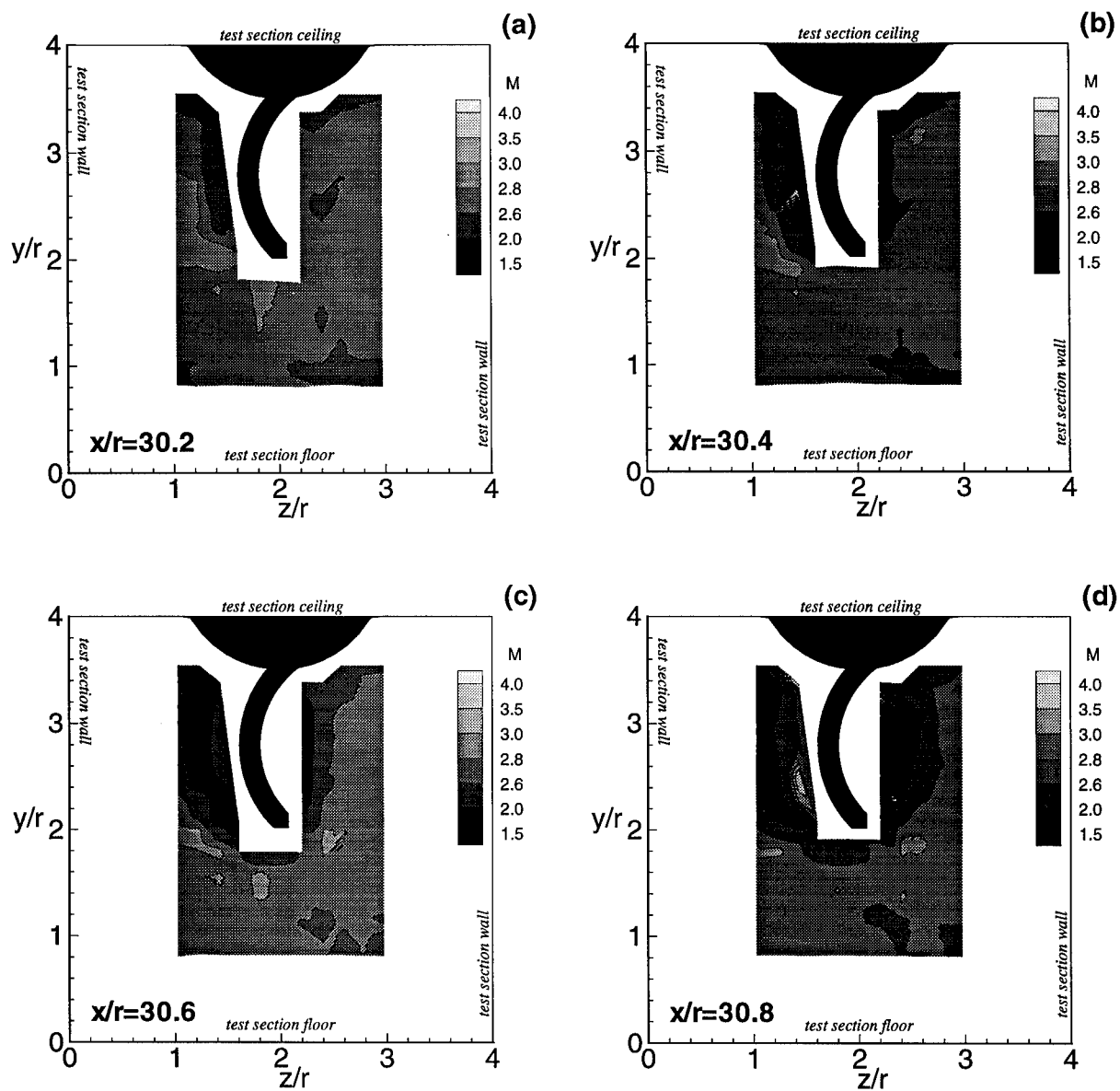


Figure 4.20 Mach Number Contours

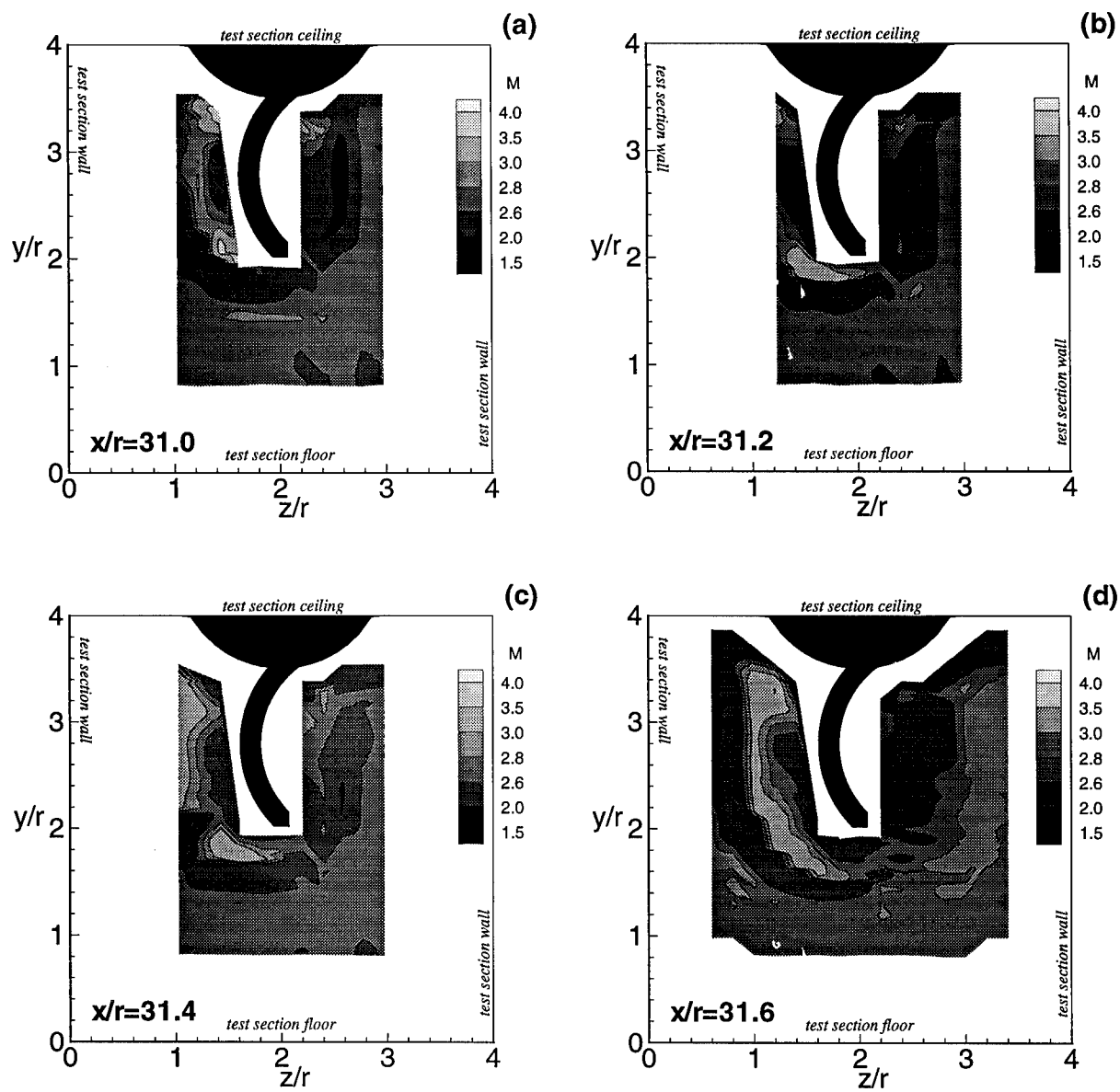


Figure 4.21 Mach Number Progression

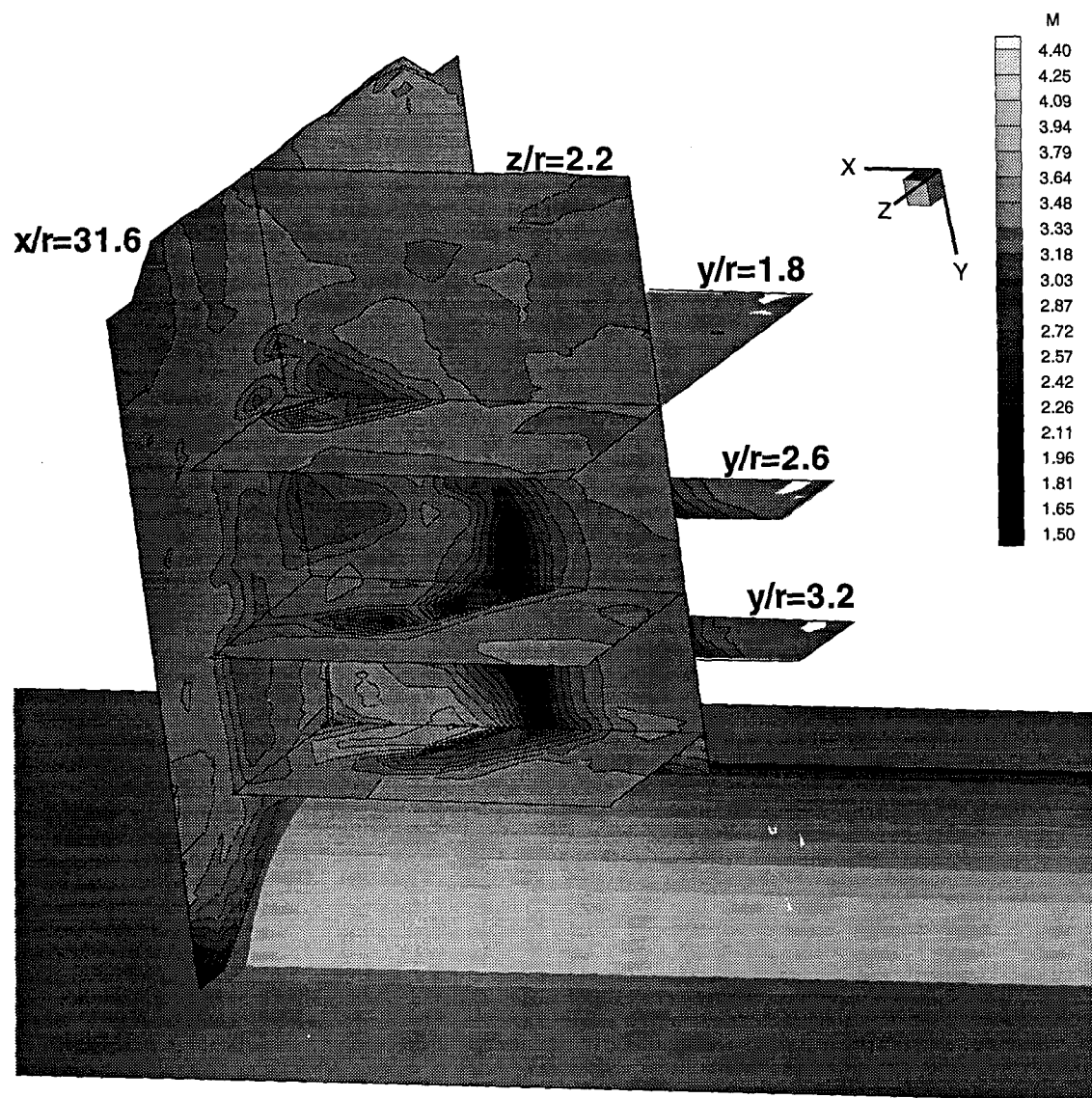


Figure 4.22 Concave Mach Contour Map

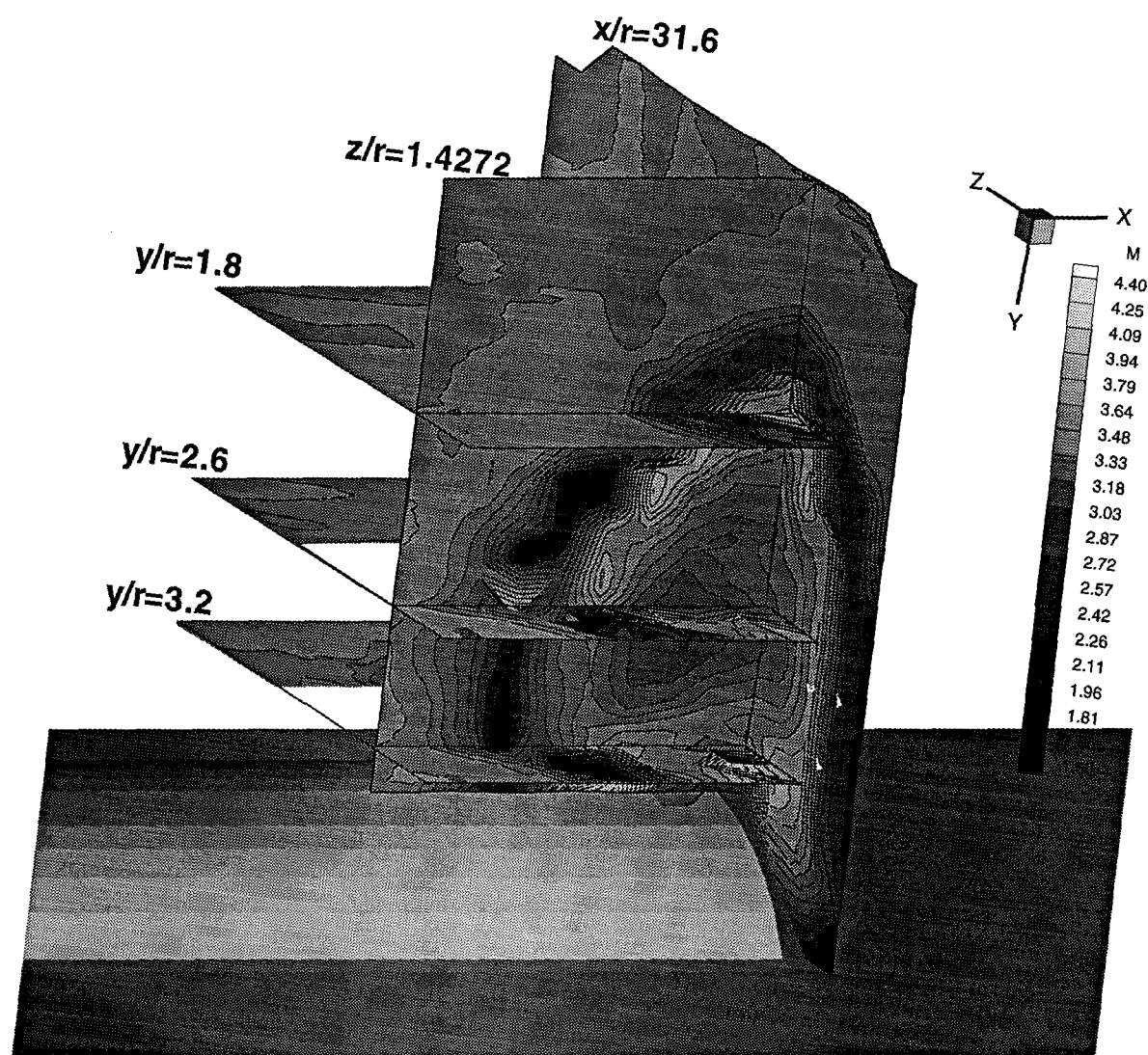


Figure 4.23 Convex Mach Contour Map



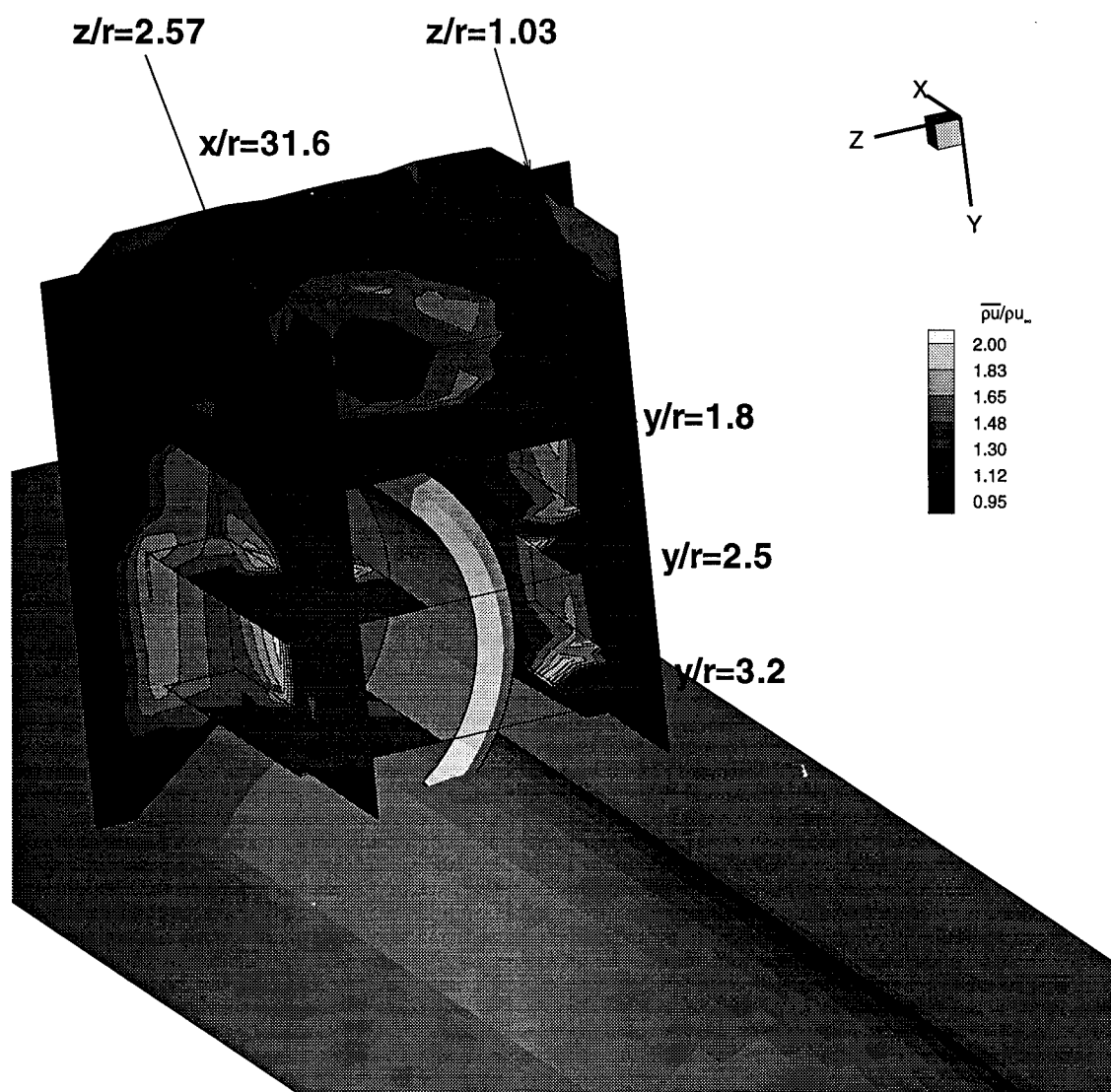


Figure 4.24 Mass-Flux Contour Map

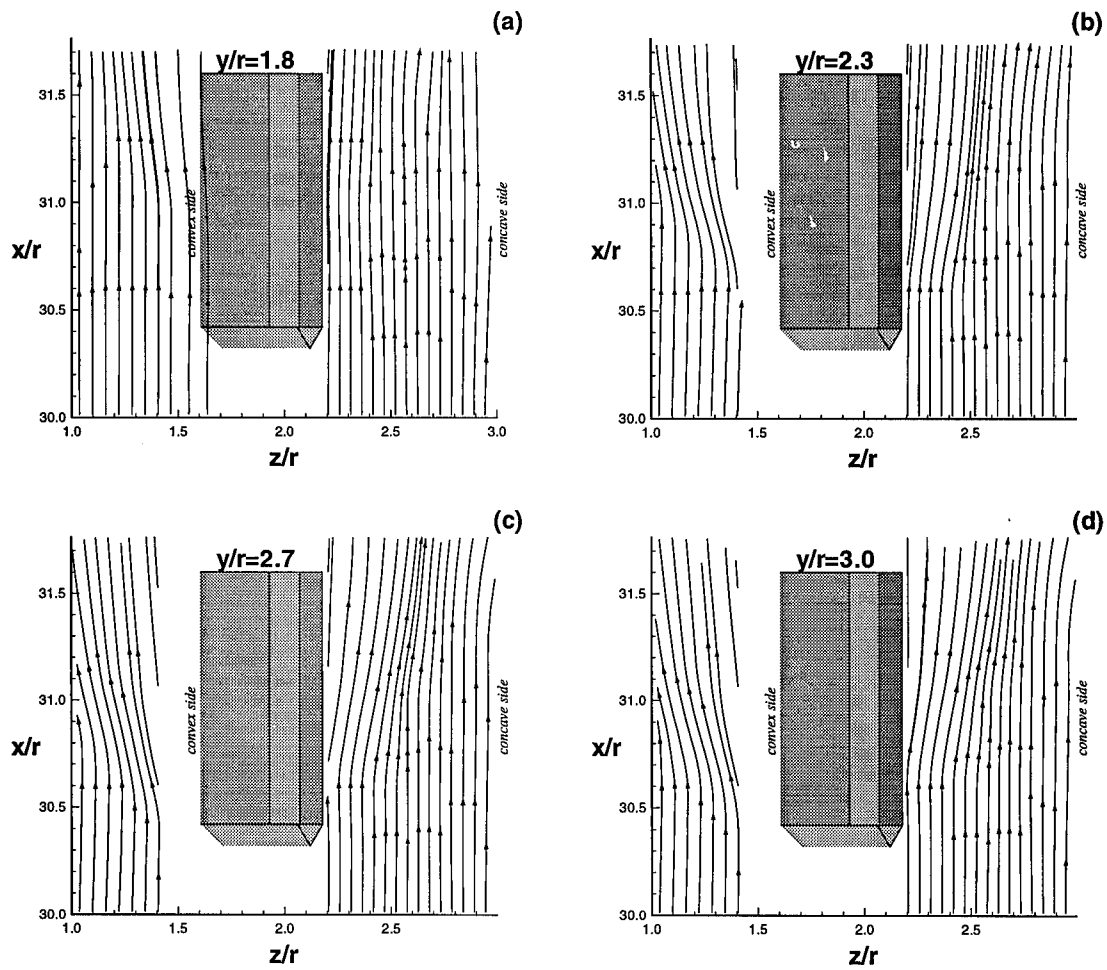


Figure 4.25 Streamlines About the WAF

side-by-side comparison of static pressure contours, showing identical flow structure. The agreement between the turbulent, viscous experiment of this thesis to the inviscid numerical simulation outside the boundary layer provides convincing evidence that the bow-shock structure is an inviscid phenomenon.

*4.3.3 Tip Region.* The bow shock which forms on the beveled face of the fin curves abruptly and travels over the tip of the fin. The tip region is marked by an expansion that forms to realign the flow interior to the bow shock. Figure 4.26 shows the expansion region outboard to the WAF tip, where the static pressure is relieved through the shock. Moran observed a tip bleeding effect in numerical analysis of the Hypersonic Applied Research Technology (HART) missile (54). The secondary-flow streamlines in Figure 4.28 do not show similar trends. No bleeding effect is evident in the secondary-flow mass-flux vector plots presented in Figure 4.29. Bleeding effects are also absent from the measured flow angles about the y and z axes, shown in Figures 4.30 and 4.31. However, it is important to note the research of Moran was conducted on a missile model with two straight fins at an angle-of-attack (symmetry conditions applied). Conversely, the WAF experimental research conducted is on a single fin with no angle-of-attack. It is expected that a bleeding effect would be achieved by a WAF at an angle-of-attack.

#### *4.4 Turbulence Measurements*

Even though the present study was unable to resolve the turbulent boundary layers about the fin, freestream turbulence information was obtained. Presented in this section are the directly measured compressible turbulent kinetic energy (TKE) and an estimate to the conventional incompressible TKE. These data may prove useful for CFD. Especially important are the effects of the “inviscid” flow phenomenon on the local freestream TKE. These effects are important because the freestream turbulence levels significantly influence the wall boundary layer and vis-versa. Figure 4.32 presents the incompressible and compressible turbulent kinetic energy. The

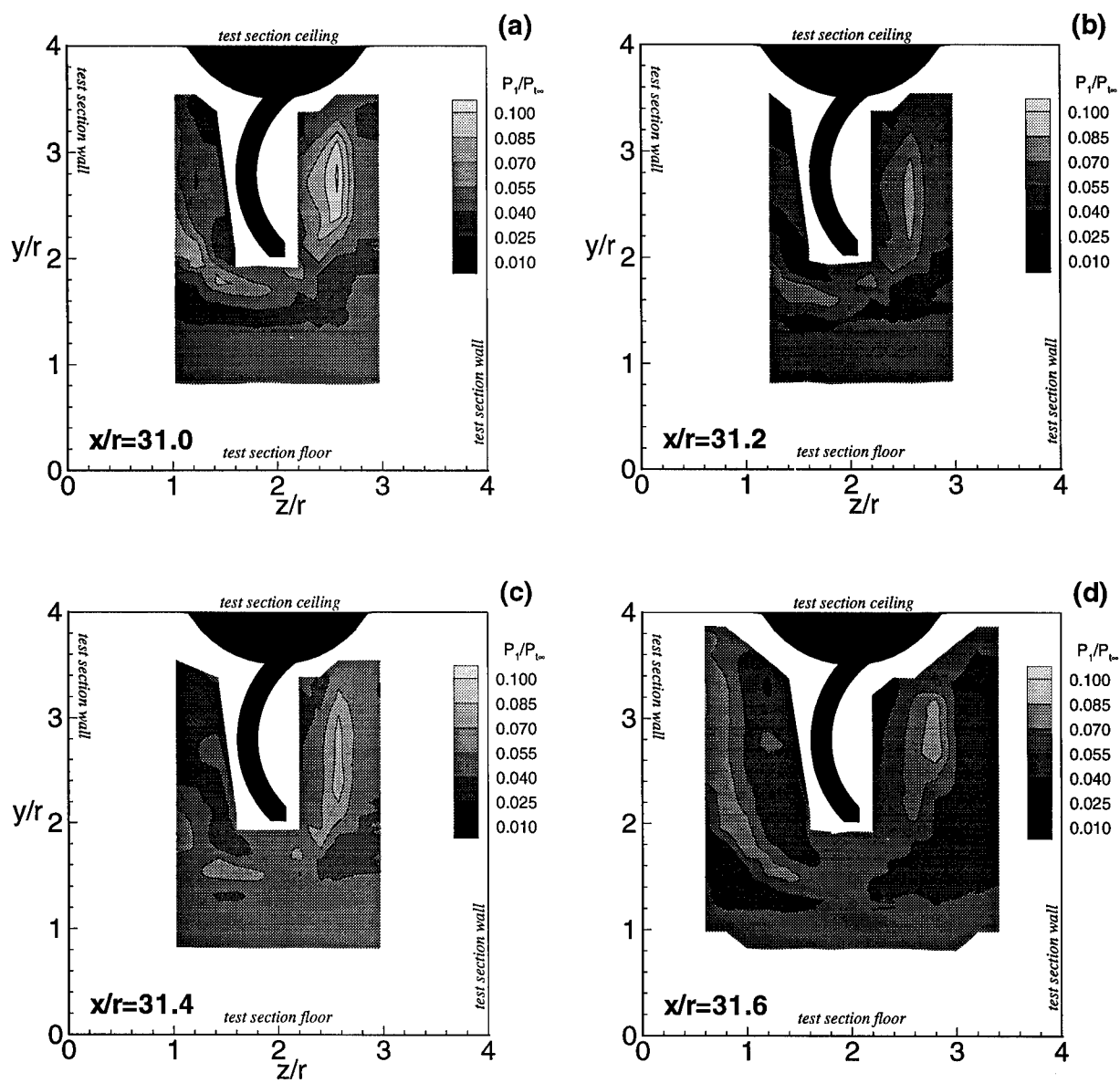


Figure 4.26 Static Pressure Contours

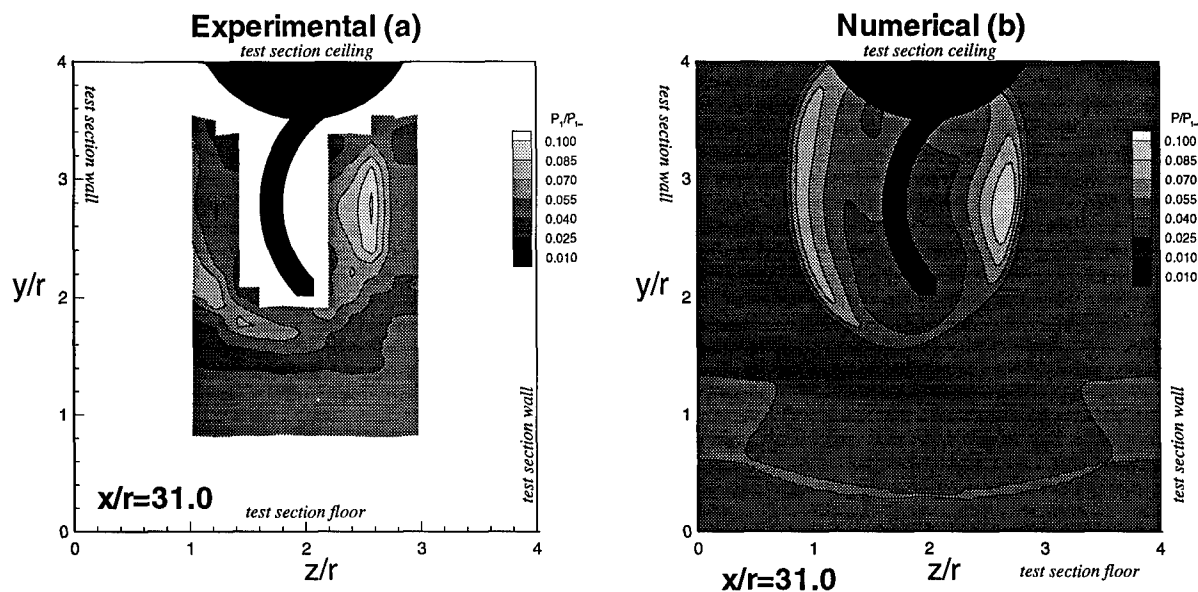


Figure 4.27 Comparison with Inviscid Numerical Solution (AIAA 96-0190)

contour plot on the left is the incompressible TKE, while compressible TKE is on the right. The TKE plots are almost identical in the region near the bow shock and near solid boundaries.

The information in this chapter is a summary of the information included in Reference (38). This reference provides a detailed summary for every variable available, presented as cutting plane contours.

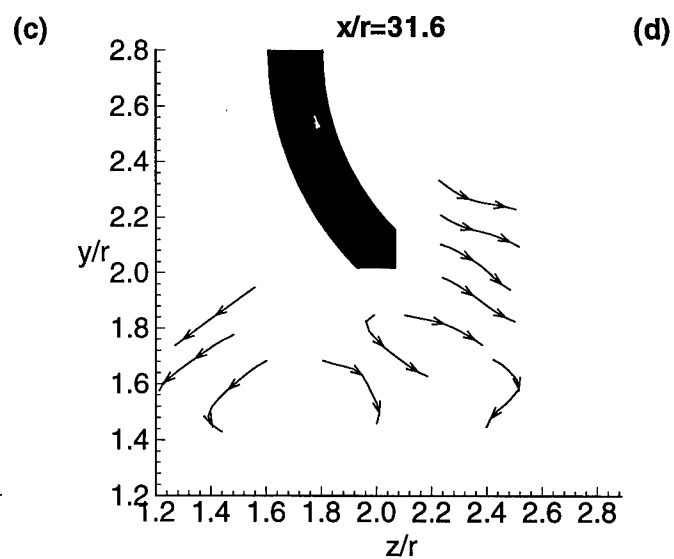
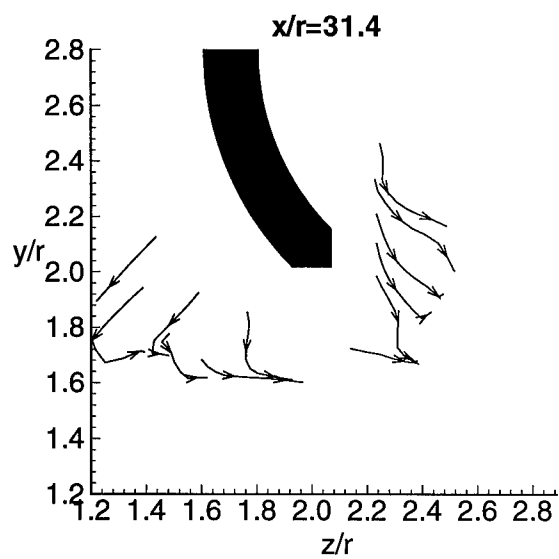
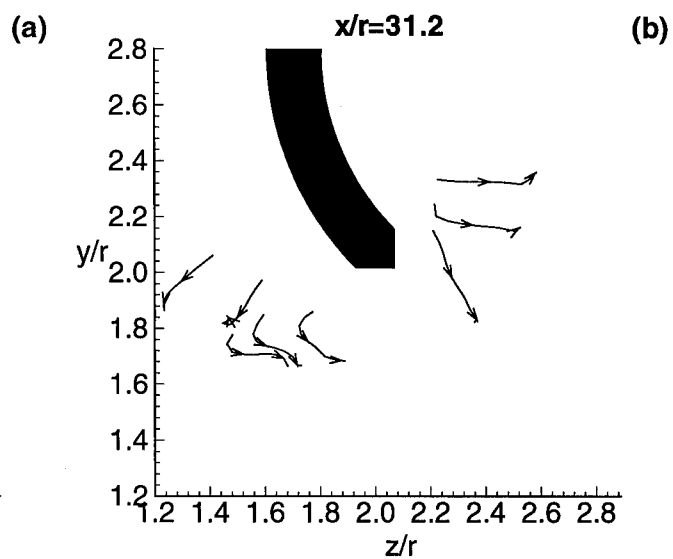
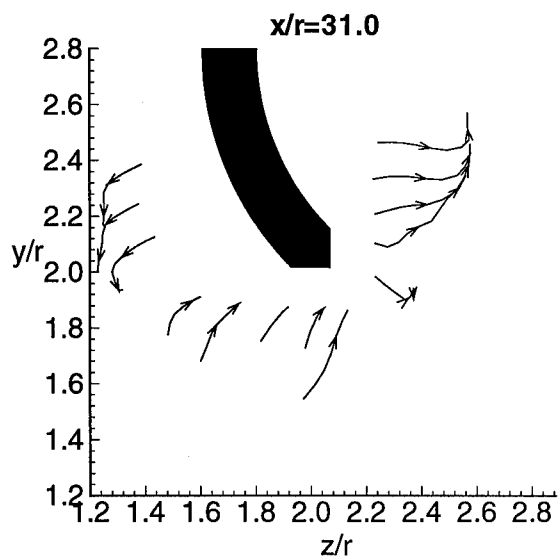


Figure 4.28 Secondary-Flow Streamlines at WAF Tip

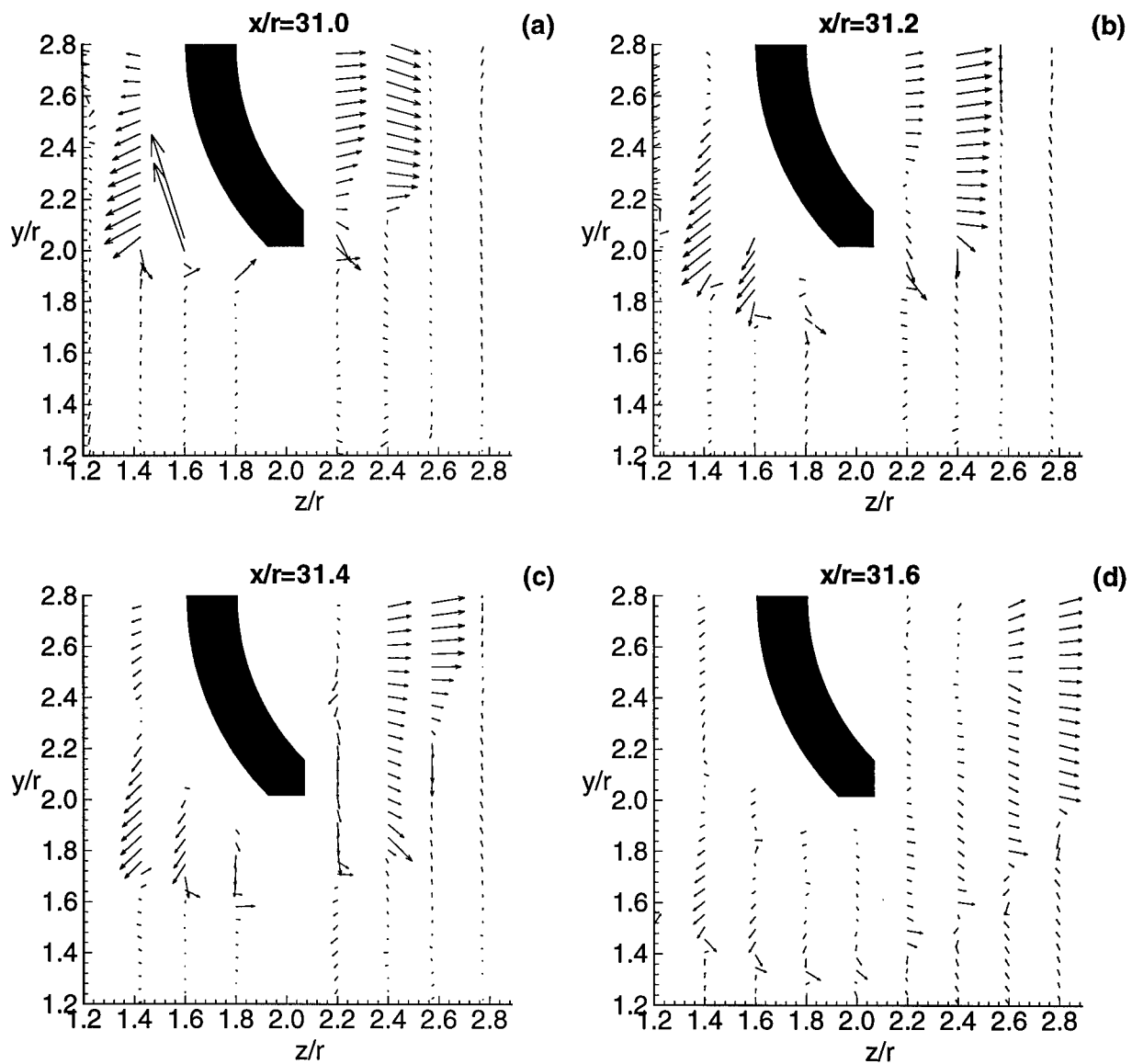


Figure 4.29 Secondary-Flow Mass-Flux Vectors at WAF Tip

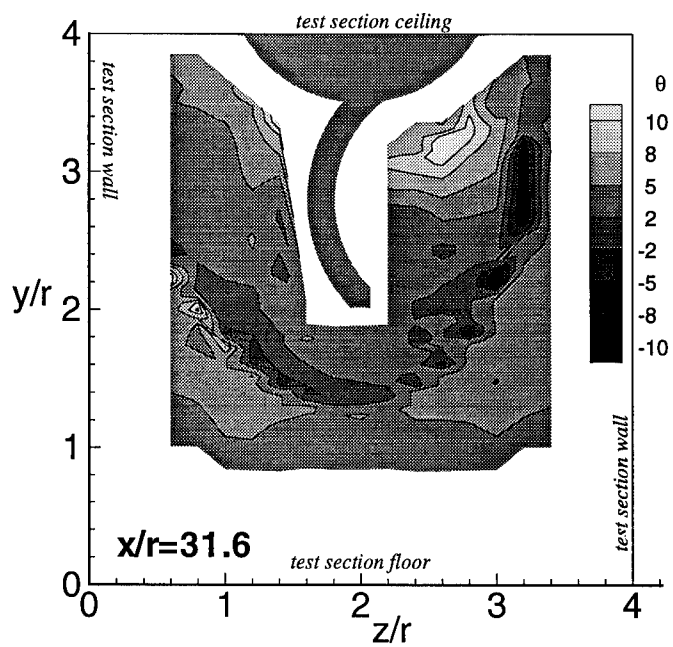


Figure 4.30 Flow Angle About Y-Axis

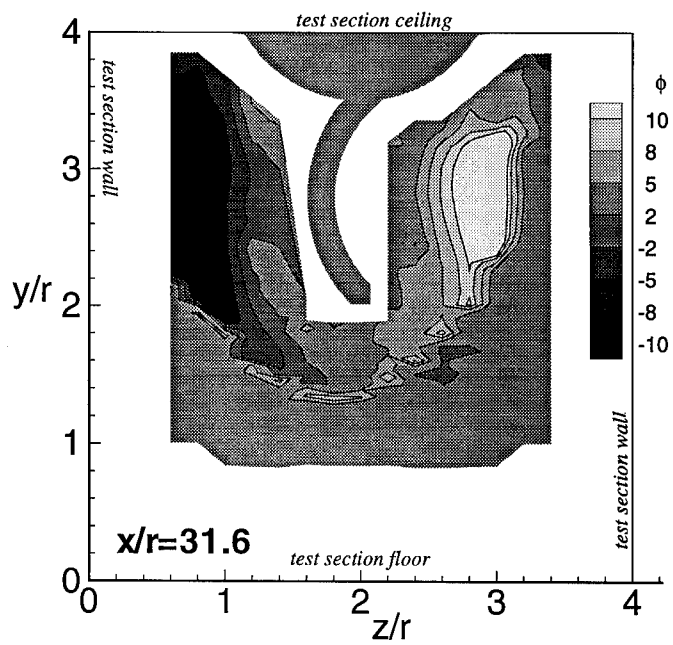


Figure 4.31 Flow Angle About Z-Axis



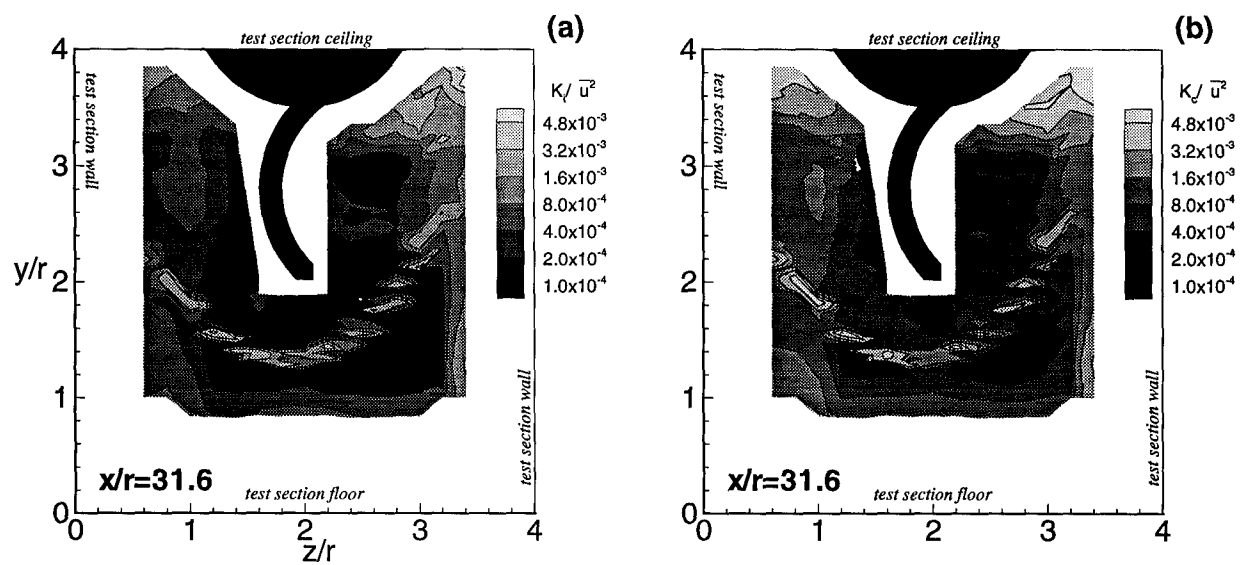


Figure 4.32 Turbulent Kinetic Energy Comparisons

## V. Conclusions and Recommendations

The following section summarizes the significant conclusions following the analysis of the flowfield in the vicinity of a wrap-around fin (WAF).

### 5.1 Conclusions

1. *A high quality dataset was created for numerical validation.* All of the applicable criteria set forth by Settles and Dodson (61) have been met. The tunnel inlet conditions are documented for use as numerical boundary conditions. Mean flow and turbulent fluctuations are presented in a high-resolution mesh in the vicinity of the wrap-around fin. These mean and turbulent measurements are outside of the fin boundary layer, therefore the measurements will not validate numerical turbulence models. However, the measurements are excellent for inviscid numerical comparisons and freestream turbulence information. The results also include a detailed uncertainty analysis to provide a reasonable bound on the information provided in this effort.
2. *The bow-shock structure present in the vicinity on a WAF is an inviscid phenomenon.* The experimental results of this work were compared to a companion study, wherein the Euler equations were solved numerically. The measured and computed pressure contours were in excellent agreement. This suggests the Euler calculations may be sufficient to capture the shock structure associated with a full WAF missile.
3. *The bow-shock is asymmetric about the WAF with stronger shock structure on the concave side.* Mean flow measurements were analyzed for differences between the concave and convex sides of the WAF. Mach number and static pressure contours show that the bow-shock is much stronger on the concave side than the convex side. A compression of the flow occurred on the concave side of the fin, while the flow was expanded on the convex side. From oil-flow

streakline visualization, it is evident that the bow-shock is located farther away from the convex side of the fin than from the concave side.

4. *The bow-shock dissipates over the fin tip.* Through comparison of Mach number and pressure contours, the shock disappears outboard of the WAF tip. The structure in this region is dominated by the expansion coming from the tip and realigning the flow downstream of the initial bow-shock.
5. *A  $\lambda$ -shock forms at the fin-body juncture.* Similar supersonic studies of fins and struts show a shock “foot” which is pushed upstream of the fin-body juncture in the body’s boundary-layer. The result of this structure is a coalescing series of shocks, shaped like the Greek symbol  $\lambda$ .
6. *A single vortex structure at the fin base is proposed.* Visualization of the surface flow revealed a separation line and a re-attachment line at the body, near the WAF. The structure in the separated region was postulated to be consisting of a single vortex which stays near the body.

## 5.2 Recommendations

The author believes the current effort to be only the first step in a series of experiments aimed at characterizing supersonic and hypersonic curved body flow. The current work was based on a DoD need to understand the flow structure about curved geometries applied to WAFs. However, the general issue is much larger than missile applications. As construction techniques advance, the mating of curved surfaces with other curved surfaces will become more aggressive on high speed vehicles for the benefits of stealthiness, aerodynamics and stowability. To reach these goals, the author suggests the following as “next-steps.”

1. *Continue further study on the current WAF model.* This study was only the first look at a geometry of this type. Further research needs to be accomplished in definition of the structures close to the WAF and the fin-body juncture. To

this end, the model could be mounted on the side wall of the tunnel, as shown in Figure 5.1. A side-mounting of the model is the easiest way to reach the recesses of the WAF with the AFIT Mach 2.9 test facility. The arrows shown in the figure show the necessary probe locations which will produce better definition of the boundary layer and fin recesses. In addition to investigating model in this arrangement, the boundary layer on the side walls must be examined. The effect of a different boundary layer development could limit the utility of comparisons to the current effort.

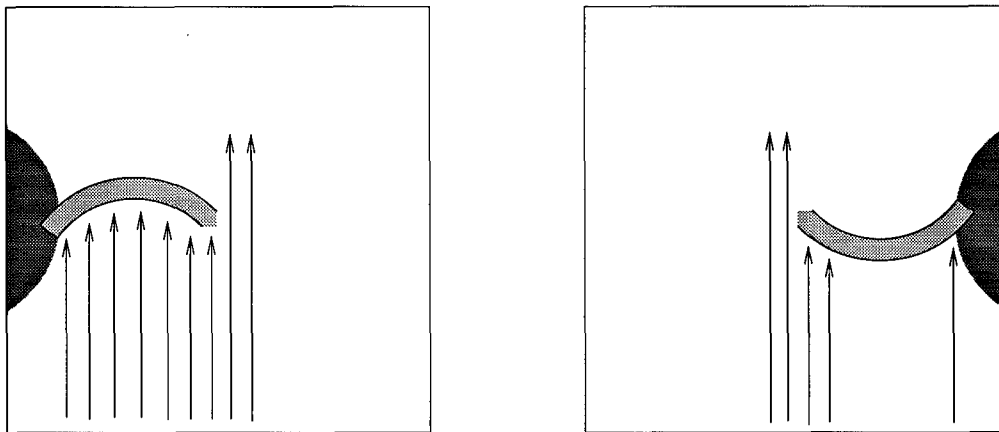


Figure 5.1 Side-Mounted WAF Model and Probe Stations of Interest

Another research effort should be conducted using a normal-wire. Figure 5.2 identifies probe stations which will add value to the current effort. The normal-wire probe can get much closer to the solid boundaries than a cross-wire probe. This probe can better define the boundary layer on the body, just before the juncture with the fin, and look at the  $\lambda$ -shock in detail.

Additionally, measurements of surface pressure should be made on the WAF. Static pressure taps can be drilled at positions from 10% to 100% of the fin's chord length along the entire span of the WAF. Two extra fins will be required since the fin is not thick enough to run tubing through the center of the WAF.

The flexible tubing will have to be recessed into the side opposite the pressure taps. Disturbances created from the tubing will limit the taps to one side of the fin.

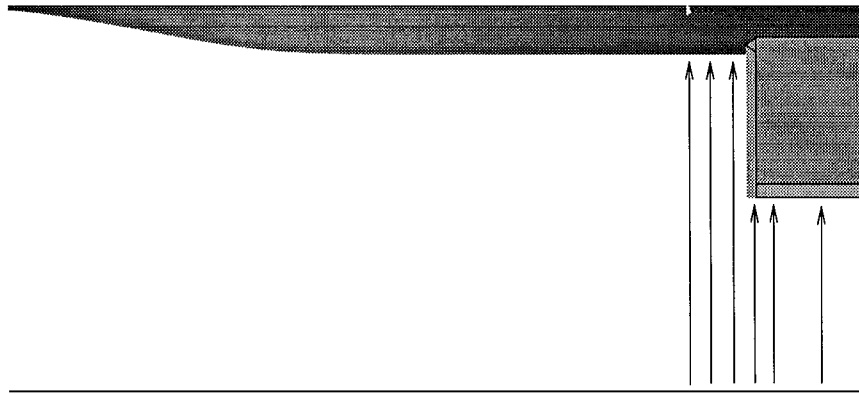


Figure 5.2 Normal Wire Probe Stations

2. *Study variations of this model.* A baseline case for the blending body and cylinder is required. Then an intermediate step between the baseline and the current effort suggests a look at the current body with a straight fin. These exercises will add to numerical validation by providing steps for a numerical analyst to follow while building their model.

After baselining this effort, extended research on the WAF should be aimed at eliminating the author's simplifications. The current work looked at only one fin, with no angle-of-attack or cant angle, on a partial body with single overheat reduction techniques. The first effort might eliminate the question of total-temperature fluctuations by providing a cursory look using multiple-overheat normal-wire reduction. Multiple fin effects would best be studied using a semi-cylindrical model and two WAFs. Another variation would put a fin at varying angles-of-attack. Finally, comparisons need to be made with

full missile mock-ups using four WAFs to ensure the simplifications did not eliminate any structures.

3. *Apply numerical simulation.* One of the goals of this experimental research is to provide field data which can be compared to numerical developments. Then the envelope of information can be drastically expanded by perturbations in Mach number, angle-of-attack, fin thickness, fin sweep and orientation and missile spin.

## *Appendix A. Error Analysis*

This section focuses on the known errors in all measurements during the experiment. The effect of measurement errors is then propagated through the data reduction process. Equations used in data reduction were linearized to provide approximate error bounds on the processed data for this experiment.

The  $l_2$  norm is utilized to combine errors. The  $l_2$  norm is defined by

$$\epsilon_x = \|\epsilon_i\|_2 = \sqrt{\sum_i \epsilon_i^2} \quad (\text{A.1})$$

The  $L_1$  norm (a summation of the absolute error values) has been found to be too conservative an estimate when compared to a perturbation analysis of the data reduction equations.

### *A.1 Measurement Errors*

Every measurement made has an associated error with it. It is assumed all measurement errors are random, with a Gaussian distribution. The assumption of random errors precludes the existence of biased errors or blunders.

Pressure was measured by pressure transducers, which measure gauge pressure. An error of  $\pm 0.0017\text{atm}$  was accrued in measurement of ambient pressure, determined to be one-half of the smallest gauge increment. Additionally, the manufacturer of the pressure transducers has advertised an error for Pitot, cone-static and plenum pressure to be 0.4%, 0.4% and 0.5%, respectively (5). Errors in pressure measurements due to calibration were determined to be one standard deviation off their respective calibration curves. The standard deviation of the calibrations are 0.2% (plenum) and 0.9% (Pitot, cone-static). Finally, digital conversion of the pressure data for storage and processing adds digitization error. All data was digitized with a 12 bit word length (4). Pressure measurements were sampled with a 12.0V

range, resulting in an error of  $\pm 0.003V$ . Multiplication of this voltage error by the slope of each calibration produces an error in pressure measurement. This error corresponds to an error of  $\pm 0.0041\text{atm}$  in plenum pressure and  $\pm 0.00046\text{atm}$  in Pitot and cone-static pressure.

The temperature in the plenum was measured during a run at the beginning of a test period. This total temperature was found to vary no more than  $\pm 2.36K$  during subsequent tunnel runs in that test period. Also, by multiple overheat (MOH) hot-wire anemometry in this test facility, McCann (51) and Miller (52) both found boundary layer total temperature root mean square (RMS) fluctuations of 2.0%. The RMS fluctuations are included as errors in this analysis as they provide a definitive bound of measurement uncertainty from large data samples.

The location of the various probes in the tunnel was determined by aligning two grids onto the Plexiglas plates to measure x and y position. This measurement determined flexing of each type of probe during tunnel operation. The flex angle and position were then determined as a function of measured position. The measurement of x and y position was accurate to  $\pm 0.00127m$ .

Without Plexiglas windows on the top and bottom of the tunnel, it was more difficult to determine the z position of each probe. The error in z position was assumed to be twice the error in x or y. An additional error from digitization occurred in the measurement of y position - as y position was recorded using a linear displacement voltage transducer, LDVT. Since the LDVT was sampled with a 12.0V range, the above error in digitization voltage was multiplied by the calibration slope. This manipulation resulted in an error in y position from digitization of  $\pm 0.000015m$ . Errors in position were compounded by the flexing of the probes during tunnel operation. Though the flex effect was accounted for, errors in y measurement produced an additional error in x.

Hot-wire measurements have shown 1.0% root mean square fluctuation in voltage for freestream flow. Additionally, a digitization error of  $\pm 0.003V$  was accounted



for in the 12.0V sampling range. The errors in pressure, temperature, position and voltage have been summarized in Table A.1.

Table A.1 Measured Error Bounds

Normalized Error	Value
$\epsilon_x$	0.4%
$\epsilon_y$	4.1%
$\epsilon_z$	8.0%
$\epsilon_{T_{t1}}$	2.1%
$\epsilon_{P_{t1}}$	0.5%
$\epsilon_{P_{t2}}$	1.1%
$\epsilon_{P_{cs}}$	2.1%
$\epsilon_{\mathcal{E}_w}$	1.0%

## A.2 Error Propagation

The errors listed in Table A.1 have an influence on all subsequent data reduction. To determine the influence on calculations, the equations used are linearized about freestream conditions. Table A.2 lists the freestream conditions for analysis. These freestream conditions were also used to normalize the results.

*A.2.1 Mean Flow.* The majority of mean flow calculations are based on the local Mach number. The Mach number is calculated from a curve fit to experimental data. The curve fit is based on the ratio of pressures from a Pitot probe and a 10° cone static probe. The variable  $\xi$  is introduced as the curve fit variable and takes the following form

$$\xi = \frac{P_{cs}}{P_{t1cs}} \cdot \frac{P_{t1t2}}{P_{t2}} \quad (\text{A.2})$$

The plenum pressures ( $P_{t1cs}, P_{t1t2}$ ) were introduced to minimize errors caused by the differences between the two separate tunnel runs, one for each probe. Since  $\xi$  was a combination of pressure measurements, the errors combine with the  $l_2$  norm

$$\epsilon_{\xi} = \|2\epsilon_{P_{t1}}, \epsilon_{P_{t2}}, \epsilon_{P_{cs}}\|_2 \quad (\text{A.3})$$

Table A.2 Freestream Conditions

Condition	Value
$x$	0.5m
$y$	0.03175m
$z$	0.03175m
$T_{t1}$	297.04K
$P_{t1}$	2.068atm
$P_{t2}$	0.7701atm
$P_{cs}$	0.0871atm
$\xi$	0.1131
$M$	2.853
$\gamma$	1.4
$R_{air}$	$287.1 \frac{\text{m}^2}{\text{s}^2\text{K}}$
$T$	113.03K
$\alpha$	$213.15 \frac{\text{m}}{\text{s}}$
$P_1$	0.065atm
$\rho_1$	$0.2195 \frac{\text{Kg}}{\text{m}^3}$
$u$	$608.1 \frac{\text{m}}{\text{s}}$
$\rho_1 u$	$133.5 \frac{\text{Kg}}{\text{m}^2\text{s}}$
$\text{Re}_\infty$	$1.700 \frac{1}{\text{m}}$
$\mathcal{E}_w$	5.0V
$T_w$	700.0K
$T_e$	297.04K
$R_w$	6.0 $\Omega$
$R_s$	50.0 $\Omega$
$R_l$	0.0 $\Omega$
$a$	0.15
$b$	-0.4
$d$	$5.1 \cdot 10^{-5}\text{m}$
$L$	0.001m
$f$	0.25
$\text{Re}_e$	$1.78 \cdot 10^4$
Nu	15.6

The curve fit (Equation 3.4) is linearized and provides an error in Mach number of

$$\epsilon_M = \|M(C_1\xi + 2C_2\xi^2 + 3C_3\xi^3 + 4C_4\xi^4)\epsilon_\xi\|_2 = 0.735\epsilon_\xi \quad (\text{A.4})$$

The Mach number and plenum temperature were used to derive the local tunnel temperature,  $T_1$ . The underlying assumption to this analysis was isentropic flow. Although isentropic flow was violated as shocks and turbulence were encountered, no method for measuring local temperature was readily available. The additional assumption of an ideal gas and the equation of state allowed for the determination of density and speed. Table A.3 has summarized the propagation errors in mean flow data analysis.

Table A.3 Mean Flow Error Bounds

Normalized Error	Derivation	Value
$\epsilon_\xi$	$\ 2\epsilon_{P_{t1}}, \epsilon_{P_{t2}}, \epsilon_{P_{cs}}\ _2$	2.4%
$\epsilon_M$	$0.735\epsilon_\xi$	1.8%
$\epsilon_{T_1}$	$\ \epsilon_{T_{t1}}, 1.254\epsilon_M\ _2$	3.1%
$\epsilon_\alpha$	$0.5\epsilon_{T_1}$	1.6%
$\epsilon_{P_1}$	$\ \epsilon_{P_{t2}}, 1.914\epsilon_M\ _2$	3.6%
$\epsilon_{\rho_1}$	$\ \epsilon_{P_1}, \epsilon_{T_1}\ _2$	4.8%
$\epsilon_u$	$\ \epsilon_M, \epsilon_\alpha\ _2$	2.4%
$\epsilon_v$	$\epsilon_u$	2.4%
$\epsilon_w$	$\epsilon_u$	2.4%

*A.2.2 Turbulent Flow.* Single overheat (SOH) hot-film anemometry was used to measure mass-flux mean flow and RMS fluctuations (SOH analysis assumes negligible total temperature fluctuations and has proved to be valid for this experimental facility (52, 24). Additionally, cross-wire measurements provided directional information. A detailed explanation of hot-film data reduction techniques is presented in Chapter III. Due to the complicated structure of hot-film data reduction, a logarithmic/derivative technique was applied to the hot-film data reduction equations to estimate the propagation of errors throughout hot-film analysis.

The Nusselt number (a measure of heat transfer from an infinite cylinder),  $Nu$ , was determined from the power consumption required to maintain a constant wire temperature (Equation 3.6). The error in  $Nu$  was a function of the measured voltage error and total temperature error.

The effective Reynolds number,  $Re_e$ , was determined by a curve fit of  $Nu$  (Kings Law, Equation 3.7). Additionally, the fluctuation in  $Re_e$  was a function of RMS voltage. These errors were combined under the  $l_2$  norm.

Table A.4 Turbulent Flow Error Bounds

Normalized Error	Derivation	Value
$\epsilon_{Nu}$	$\ 2.0\epsilon_{\varepsilon_w}, \epsilon_{T_{t1}}\ _2$	2.3%
$\epsilon_{Re_e}$	$\ 2.0\epsilon_{Nu}, \epsilon_{\varepsilon_w}\ _2$	4.7%
$\epsilon_f$	$0.5\epsilon_{Re_e}$	2.4%
$\epsilon_{Re_e^2}$	$2.0\epsilon_{Re_e}$	9.4%
$\epsilon_{Re_x^2}$	$\ \epsilon_{Re_{e1}^2}, \epsilon_{Re_{e1}Re_{e2}}, \epsilon_{Re_{e2}^2}\ _2$	16.3%
$\epsilon_{Re_xRe_y}$	$\epsilon_{Re_x^2}$	16.3%
$\epsilon_{Re_xRe_z}$	$\epsilon_{Re_x^2}$	16.3%
$\epsilon_{Re_x}$	$0.5\epsilon_{Re_x^2}$	8.1%
$\epsilon_{Re_y}$	$\epsilon_{Re_x}$	8.1%
$\epsilon_{Re_z}$	$\epsilon_{Re_x}$	8.1%

*A.2.3 Separation of Variables.* In separating the primitive variables from hot-wire data, the error in Reynolds number equates to an error in mass-flux. It was assumed that errors in off-axial velocities (ie.  $v$  and  $w$ ) were the same as the associated error in  $u$ . The separation equations were linearized about the reference conditions of Table A.2. The results of variable separation error analysis are summarized in Table A.5.

Table A.5 Variable Separation Error Bounds

Normalized Error	Derivation	Value
$\epsilon_{(\rho u)'}'$	$\epsilon_{\text{Re}_x}$	8.1%
$\epsilon_{(\rho v)'}'$	$\epsilon_{\text{Re}_y}$	8.1%
$\epsilon_{(\rho w)'}'$	$\epsilon_{\text{Re}_z}$	8.1%
$\epsilon_{(\rho u)'(\rho v)'}'$	$\epsilon_{\text{Re}_x \text{Re}_y}$	16.3%
$\epsilon_{(\rho u)'(\rho w)'}'$	$\epsilon_{\text{Re}_x \text{Re}_z}$	16.3%
$\epsilon_{\rho'}$	$\ 0.458\epsilon_M, 0.771\epsilon_{(\rho u)'}'\ _2$	6.3%
$\epsilon_{u'}$	$\ \epsilon_{\rho'}, \epsilon_{(\rho u)'}'\ _2$	10.3%
$\epsilon_{v'}$	$\epsilon_{u'}$	10.3%
$\epsilon_{w'}$	$\epsilon_{u'}$	10.3%

## *Appendix B. Nozzle Coordinates*

Tables B.1 and B.2 detail the coordinates of the nozzle of AFIT's Mach 2.9 test facility. Note the nozzle is two dimensional and has a width ( $z$ ) of 6.35cm. The origin is located on the floor at the throat. The coordinates extend from upstream of the convergent section to the beginning of the first removable test section. Figure B.1 is a plot of the data.

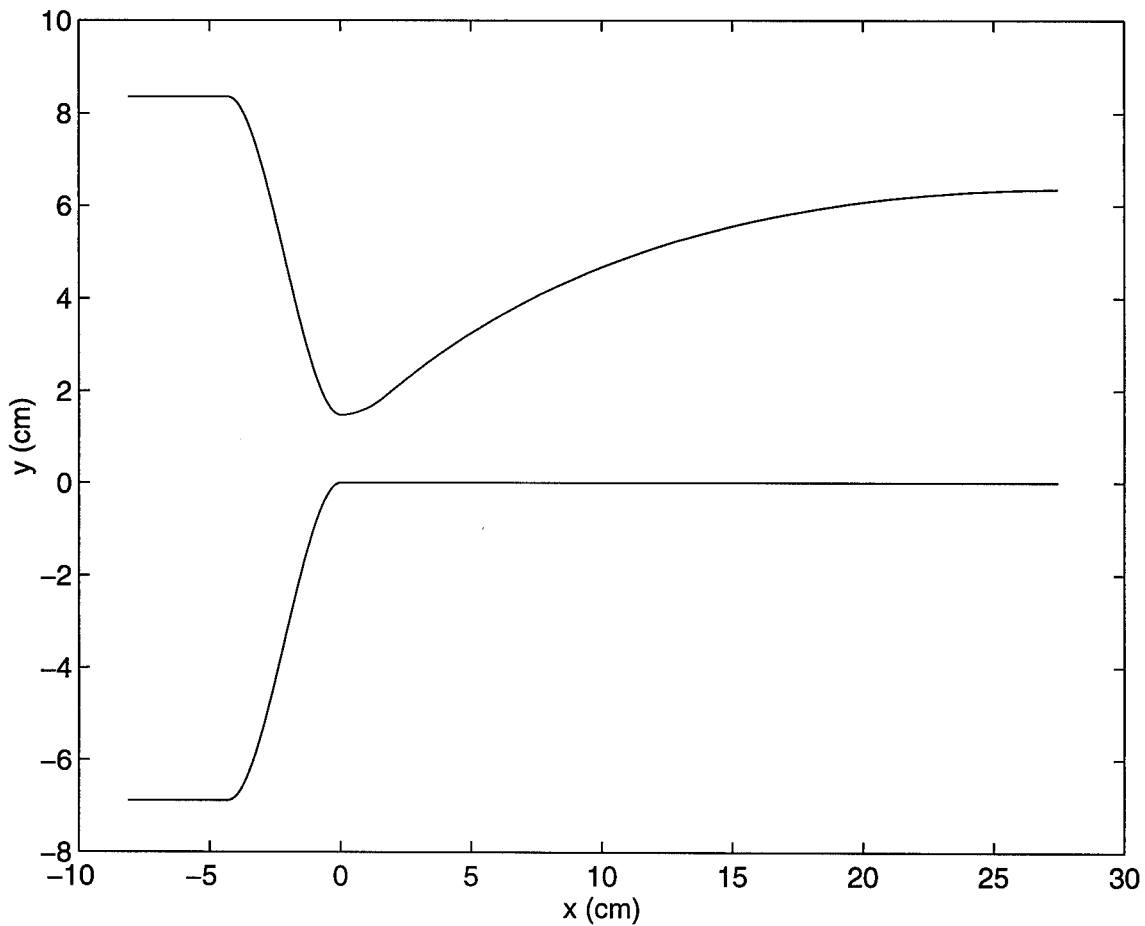


Figure B.1 Mach 2.9 Nozzle Coordinates

Table B.1 Nozzle Coordinates (Top)

$x$ (cm)	$y$ (cm)	$x$ (cm)	$y$ (cm)	$x$ (cm)	$y$ (cm)
-8.102600	8.359140	-1.663700	3.776980	1.452880	1.772920
-4.292600	8.359140	-1.577340	3.578860	1.579880	1.826260
-4.206240	8.348980	-1.488440	3.385820	1.645920	1.855216
-4.117340	8.323580	-1.402080	3.197860	2.275840	2.151126
-4.030980	8.282940	-1.313180	3.014980	3.345180	2.621280
-3.942080	8.227060	-1.226820	2.839720	3.848100	2.824480
-3.855720	8.158480	-1.137920	2.672080	4.348480	3.014980
-3.766820	8.074660	-1.051560	2.511806	4.851400	3.200400
-3.680460	7.975600	-0.962660	2.360422	5.367020	3.380740
-3.591560	7.866380	-0.876300	2.218690	5.897880	3.558540
-3.505200	7.747000	-0.787400	2.086864	6.449060	3.733800
-3.416300	7.614920	-0.701040	1.966214	7.025640	3.909060
-3.329940	7.472680	-0.612140	1.856994	7.630160	4.081780
-3.241040	7.322820	-0.525780	1.759966	8.265160	4.251960
-3.154680	7.162800	-0.436880	1.676146	8.933180	4.422140
-3.065780	6.992620	-0.350520	1.605788	9.636760	4.589780
-2.979420	6.817360	-0.261620	1.549908	10.38098	4.754880
-2.890520	6.634480	-0.175260	1.509268	11.17092	4.917440
-2.804160	6.446520	-0.086360	1.484122	12.00658	5.080000
-2.715260	6.253480	0.000000	1.475740	12.89304	5.237480
-2.628900	6.055360	0.182880	1.482344	13.83538	5.387340
-2.540000	5.854700	0.292100	1.490472	14.83614	5.532120
-2.453640	5.648960	0.403860	1.501648	15.90294	5.674360
-2.364740	5.440680	0.513080	1.516380	17.03832	5.803900
-2.278380	5.232400	0.624840	1.534414	18.23720	5.925820
-2.189480	5.021580	0.739140	1.556004	19.53260	6.037580
-2.103120	4.810760	0.853440	1.581404	20.92960	6.136640
-2.014220	4.599940	0.967740	1.610868	22.40280	6.217920
-1.927860	4.391660	1.087120	1.644396	23.97760	6.283960
-1.838960	4.183380	1.206500	1.682496	25.65400	6.329680
-1.752600	3.980180	1.328420	1.725168	27.45740	6.350000

Table B.2 Nozzle Coordinates (Bottom)

$x$ (cm)	$y$ (cm)	$x$ (cm)	$y$ (cm)
-8.10260	-6.883400	-2.10312	-3.335020
-4.29260	-6.883400	-2.01422	-3.124200
-4.20624	-6.873240	-1.92786	-2.915920
-4.11734	-6.847840	-1.83896	-2.707640
-4.03098	-6.807200	-1.75260	-2.503678
-3.94208	-6.751320	-1.66370	-2.301748
-3.85572	-6.682740	-1.57734	-2.103882
-3.76682	-6.598920	-1.48844	-1.910334
-3.68046	-6.499860	-1.40208	-1.722120
-3.59156	-6.390640	-1.31318	-1.540002
-3.50520	-6.271260	-1.22682	-1.364488
-3.41630	-6.139180	-1.13792	-1.196086
-3.32994	-5.996940	-1.05156	-1.036066
-3.24104	-5.847080	-0.96266	-0.884682
-3.15468	-5.687060	-0.87630	-0.742950
-3.06578	-5.516880	-0.78740	-0.611124
-2.97942	-5.341620	-0.70104	-0.490474
-2.89052	-5.158740	-0.61214	-0.381254
-2.80416	-4.970780	-0.52578	-0.284226
-2.71526	-4.777740	-0.43688	-0.200355
-2.62890	-4.579620	-0.35052	-0.130100
-2.54000	-4.378960	-0.26162	-0.074244
-2.45364	-4.173220	-0.17526	-0.033452
-2.36474	-3.964940	-0.08636	-0.008481
-2.27838	-3.756660	0.00000	0.000000
-2.18948	-3.545840	27.4574	0.000000



## *Bibliography*

1. "Owners Manual: Omega's Digital Temperature Indicators." Stamford, Connecticut: Omega Engineering Inc., 1979.
2. "IFA 100 System: Instruction Manual." St. Paul, Minnesota: TSI Incorporated, 1987.
3. "Contact HeNe Laser Instruction Manual." Stratford, Connecticut: Oriel Instruments, 1990.
4. "Nicolet MultiPro Systems Operation Manual: Data Acquisition Systems." Madison, Wisconsin: Nicolet Instrument Corporation, 1991.
5. "General Catalog Binder." San Juan Capistrano, California: Endevco Corporation, 1992.
6. "Installation, Operation and Maintenance Manual." Woburn, Massachusetts: Xenon Corporation, 1994.
7. Abate, G.. *Aerodynamic Research of Wrap Around Fin Missile Configurations and Alternative Wrap Around Fin Designs*. Technical Report WL-TR-94-7015, USAF Wright Laboratories, 1994.
8. Abate, G. and C. Berner. "Wind Tunnel Measurements of Wrap Around Fins at Mach 2.06," *AIAA Paper*, (94-3499) (1994).
9. Abate, G. and T. Cook. "Analysis of Missile Configurations with Wrap-Around Fins Using Computational Fluid Dynamics," *AIAA Paper*, (93-3631) (1993).
10. Abate, G. and W. Hathaway. "Aerodynamics of Missiles with Offset Fin Configurations," *AIAA Paper*, (89-3367) (1989).
11. Abate, G. and W. Hathaway. "Aerodynamic Test and Analysis of Wrap Around Fins with Base Cavities," *AIAA Paper*, (94-0051) (1994).
12. Abate, G. and G. Winchenbach. "Aerodynamics of Missiles with Slotted Fin Configurations," *AIAA Paper*, (91-0676) (1991).
13. Anderson, D., et al. *Computational Fluid Mechanics and Heat Transfer*. Series in Computational Methods in Mechanics and Thermal Sciences, New York: Hemisphere Publishing Corporation, 1984.
14. Anderson, J. *Modern Compressible Flow; with Historical Perspective*. New York: McGraw-Hill, Inc., 1982.
15. Anderson, J. *Hypersonic and High Temperature Gas Dynamics*. New York: McGraw-Hill, Inc., 1989.
16. Anderson, J. *Fundamentals of Aerodynamics* (Second Edition). New York: McGraw-Hill, Inc., 1991.

17. Bowersox, R. *Compressible Turbulence Measurements in a High-Speed High Reynolds Number Mixing Layer*. PhD dissertation, Virginia Polytechnic Institute and State University, Blacksburg, Virginia, September 1992.
18. Bowersox, R. "Thermal Anemometry." *Handbook of Fluid Dynamics and Fluid Machinery*, edited by J. Schetz and W. Fuhs. John Wiley, 1995.
19. Bowersox, R. and J. Schetz. "Compressible Turbulence Measurements in a High-Speed High Reynolds Number Mixing Layer," *AIAA Paper*, (93-0660) (1993).
20. Bowersox, R. and J. Schetz. "Compressible Turbulence Measurements in a High-Speed High Reynolds Number Mixing Layer," *AIAA Journal*, 32(4) (1994).
21. Chou, J. and M. Childs. "Aerodynamic Test and Analysis of a Missile Configuration with Curved Fins," *AIAA Paper*, (83-1672) (1983).
22. Donovan, J. and E. Spina. "An Improved Analysis Method for Cross-Wire Signals Obtained in Supersonic flow," *Experiments in Fluids*, 12:359-368 (1992).
23. Donovan, J., et al. "The Structure of a Supersonic Turbulent Boundary Layer Subjected to Concave Surface Curvature," *Journal of Fluid Mechanics*, 259:1-24 (1994).
24. Dotter, J. *Compressible Turbulence Measurements in a Supersonic Boundary Layer Including Adverse Pressure Gradient Effects*. MS thesis, Air Force Institute of Technology, Wright-Patterson Air Force Base, Ohio, December 1994.
25. Edge, H. "Computation of Roll Moment for a Projectile with Wrap-Around Fins," *Journal of Spacecraft and Rockets*, 31(4):615-620 (1994).
26. Fernando, E. and A. Smits. "A Supersonic Turbulent Boundary Layer in an Adverse Pressure Gradient," *Journal of Fluid Mechanics*, 211:285-307 (1990).
27. Fernholz, H. and M. Finley. "A Critical Commentary on Mean Flow Data for Two-Dimensional Compressible Turbulent Boundary Layers." *AGARDograph* Number 253, chapter 2,3, Paris: NATO, 1980.
28. Fernholz, H., et al. "A Further Compilation of Compressible Boundary Layer Data with a Survey of Turbulence Data." *AGARDograph* Number 263, chapter 2,4,5, Paris: NATO, 1981.
29. Fomison, N. *The Effects of Sweep and Bluntness on Glancing Shock Wave Turbulent Boundary Layer Interaction*. PhD dissertation, Cranfield Institute of Technology, England, September 1986.
30. Garrison, T. and G. Settles. "Structure of Crossing-Shock Wave/Turbulent Boundary-Layer Interactions," *AIAA Paper*, (92-3670) (1992).
31. Garrison, T. and G. Settles. "Laser Interferometer Skin-Friction Measurements of Crossing-Shock Wave/Turbulent Boundary-Layer Interactions," *AIAA Paper*, (93-3072) (1993).

32. Goldstein, R. *Fluid Mechanics Measurements*. New York: Hemisphere Publishing Corporation, 1983.
33. Green, J. "Interactions Between Shock Waves and Turbulent Boundary Layers," *Progress in Aerospace Sciences*, 11:235-340 (1970).
34. Hayakawa, K., et al. "Hot-Wire Investigation of an Unseparated Shock-Wave/Turbulent Boundary-Layer Transition," *AIAA Journal*, 22(5):579-585 (May 1984).
35. Hayakawa, K., et al. "Turbulence Measurements in a Compressible Reattaching Shear Layer," *AIAA Journal*, 22(7):889-895 (July 1984).
36. Horstman, C. and F. Owen. "Turbulent Properties of a Compressible Boundary Layer," *AIAA Journal*, 10(11):1418-1424 (November 1972).
37. Hsu, J. and G. Settles. "Holographic Flowfield Density Measurements in Swept Shock Wave/Boundary-Layer Interactions," *AIAA Paper*, (92-0746) (1992).
38. Huffman, R. "Wrap-Around Fin Data Synopsis." AFIT Report 96-01, Air Force Institute of Technology, Wright-Patterson Air Force Base, Ohio, December 1995.
39. Jayaram, M., et al. "The Response of a Compressible Turbulent Boundary Layer to Short Regions of Concave Surface Curvature," *Journal of Fluid Mechanics*, 175:343-362 (1987).
40. Kim, K., et al. "Laser Skin Friction Measurements and CFD Comparison of Weak-to-Strong Swept Shock Boundary-Layer Interactions," *AIAA Paper*, (90-0378) (1990).
41. Kim, Y. and G. Winchenbach. "The Roll Motion of a Wraparound Fin Configuration at Subsonic and Transonic Mach Numbers," *AIAA Paper*, (85-1777) (1985).
42. Kistler, A. "Fluctuation Measurements in a Supersonic Turbulent Boundary-Layer," *Physics of Fluids*, 2(3):290-296 (1959).
43. Knight, D., et al. "The Flowfield Structure of the 3-D Shock Wave - Boundary Layer Interaction Generated by a 20 deg Sharp Fin at Mach 3," *AIAA Paper*, (86-0343) (1986).
44. Kopal, Z. *Tables of Supersonic Flow Around Cones*. Cambridge, MA: Murray Printing Company, 1947. MIT Center of Analysis Technical Report Number 1.
45. Kováshay, L. "The Hot-Wire Anemometer in Supersonic Flow," *Journal of the Aeronautical Sciences*, 17(9):565-572,584 (September 1950).
46. Kováshay, L. "Turbulence in Supersonic Flow," *Journal of the Aeronautical Sciences*, 20(10):657-674,682 (October 1953).
47. Kretschmar, R., et al. "Aerodynamic Characteristics of Wrap Around Fins on a Tube Launched Tactical Missile," *AIAA Paper*, (95-1897) (1995).

48. Laderman, A. "Adverse Pressure Gradient Effects on Supersonic Boundary-Layer Turbulence," *AIAA Journal*, 18(10):1186-1195 (October 1980).
49. Lee, Y., et al. "Heat Transfer Measurements and CFD Comparison of Swept Shock Wave/Boundary-Layer Interactions," *AIAA Paper*, (92-3665) (1992).
50. Lomas, C. *Fundamentals of Hot Wire Anemometry*. Cambridge, MA: Cambridge University Press, 1986.
51. McCann, G. *Compressible Turbulence Measurement in Low-Angle Injection into a Supersonic Flow*. MS thesis, Air Force Institute of Technology, Wright-Patterson Air Force Base, Ohio, March 1995.
52. Miller, R. *Compressible Turbulence Measurements in a Supersonic Boundary Layer Including Favorable Pressure Gradient Effects*. MS thesis, Air Force Institute of Technology, Wright-Patterson Air Force Base, Ohio, December 1994.
53. Miller, R., et al. "Compressible Turbulence Measurements in Supersonic Boundary Layers with Favorable and Adverse Pressure Gradients," *Transactions of the ASME, Journal of Fluids Engineering* (August 1995).
54. Moran, K. *An Aerodynamic and Static-Stability Analysis of the Hypersonic Applied Research Technology (HART) Missile*. PhD dissertation, Air Force Institute of Technology, Wright-Patterson Air Force Base, Ohio, April 1994.
55. Morkovin, M. "Effects of High Acceleration on a Turbulent Supersonic Shear Layer," *Proceedings of the Heat Transfer and Fluid Mechanics Institute*, 4:1-17 (1955).
56. Morkovin, M. "Fluctuations and Hot-Wire Anemometry in Compressible Flow." *AGARDograph* Number 24, Paris: NATO, 1956.
57. Morkovin, M. "Effects of Compressibility on Turbulent Flows," *AGARD*, 4:368-380 (1961).
58. Morkovin, M. "Effects of Compressibility on Turbulent Flow." *The Mechanics of Turbulence* edited by A. Favré, New York: Gordon and Beach, 1964.
59. Pope, A. and K. Goin. *High-Speed Wind Tunnel Testing*. New York: John Wiley and Sons, Inc., 1965.
60. Rose, W. and D. Johnson. "Turbulence in a Shock-Wave Boundary-Layer Transition," *AIAA Journal*, 13(7):884-889 (July 1975).
61. Settles, G. and L. Dodson. "Supersonic and Hypersonic Shock/Boundary-Layer Interaction Database," *AIAA Journal*, 32(7) (July 1994).
62. Smits, A. and J. Dussauge. "Hot-Wire Anemometry in Supersonic Flow." *AGARDograph* Number 315, chapter 5, Paris: NATO, 1989.
63. Smits, A., et al. "Constant Temperature Hot-Wire Anemometer Practice in Supersonic Flows," *Experiments in Fluids*, 1:83-92 (1983). Part 1: The Normal Wire.

64. Smits, A. and K. Muck. "Constant Temperature Hot-Wire Anemometer Practice in Supersonic Flows," *Experiments in Fluids*, 2:33-41 (1984). Part 2: The Inclined Wire.
65. Smits, J. and K. Muck. "Experimental Study of Three Shock Wave/Turbulent Boundary Layer Interactions," *Journal of Fluid Mechanics*, 182:291-314 (1987).
66. Spangenberg, W. *Heat-Loss Characteristics of Hot-Wire Anemometers at Various Densities in Transonic and Supersonic Flow*. Technical Report TN 3381, NACA, 1955.
67. Spina, E., et al. "The Physics of Supersonic Turbulent Boundary Layers," *The Annual Review of Fluid Mechanics*, 26:287-319 (1994).
68. Swenson, M., et al. "Aerodynamic Test and Analysis of Wrap-Around Fins at Supersonic Mach Numbers Utilizing Design of Experiments," *AIAA Paper*, (94-0200) (1994).
69. Tilmann, C. "Numerical and Experimental Investigation of the Turbulent Shock/Boundary-Layer Interaction on a Wrap-Around Fin Configuration." PhD prospectus, Air Force Institute of Technology, Wright-Patterson Air Force Base, Ohio, December 1994.
70. Tilmann, C., et al. "Characterization of the Flow Structure in the Vicinity of a Wrap-Around Fin at Supersonic Speeds," *AIAA Paper*, (96-0190) (1996).
71. Vitale, R., et al. "Aerodynamic Test and Analysis of a Missile Configuration with Curved Fins," *AIAA Paper*, (92-4495) (1992).
72. Volluz, R. *Handbook of Supersonic Aerodynamics*. Technical Report, NAVORD Report 1988, 1961.
73. Walker, D., et al. "Experimental Comparison of Two Hot-Wire Techniques in Supersonic Flow," *AIAA Journal*, 27(8):1074-1080 (August 1989).
74. White, F. *Viscous Fluid Flow* (Second Edition). New York: McGraw-Hill, Inc., 1991.
75. Whyte, R. and W. Hathaway. "Subsonic and Transonic Aerodynamics of a Wraparound Fin Configuration," *AIAA Paper*, (85-0106) (1985).
76. Wilcox, D. *Turbulence Modeling for CFD*. Glendale, CA: DCW Industries, Inc., 1993.
77. Williams, K., et al. "Investigation of Supersonic Flow About Strut/Endwall Intersections in an Annular Duct," *AIAA Journal*, 33(4):586-594 (April 1995).

### *Vita*

Second Lieutenant Richard Edwin Huffman, Jr., who is the son of Richard and Dolores Huffman, [REDACTED] He graduated from Randolph High School in Randolph, Wisconsin, and enrolled at Purdue University. While attending college, Richard had the distinction of being the only student at Purdue jointly enrolled in the Reserve Officers Training Corps and the Engineering Cooperative Education program - alternating between semesters of classes and work at the National Aerospace Intelligence Center. Richard graduated from Purdue with a Bachelor of Science in Aeronautical and Astronautical Engineering and was commissioned in the Air Force on Friday the thirteenth of May, 1994. He was acquired by the Air Force Institute of Technology just one week later, graduating with a Masters of Science in Aeronautical Engineering in December, 1995.

Lt Huffman married Second Lieutenant Michelle Lynne Hartman of Liberty, Indiana in March 1994.

Permanent address: N9084 Cty Hwy FW  
Randolph, Wisconsin 53956-9639

December 1995

Master's Thesis

MACH 2.9 INVESTIGATION INTO THE FLOW STRUCTURE IN THE  
VICINITY OF A WRAP-AROUND FIN

Richard E. Huffman

Air Force Institute of Technology, WPAFB OH 45433-6583

AFIT/GAE/ENY/95D-13

Greg Abate  
WL/MNAA, Eglin AFB FL

Distribution Unlimited

Abstract

A ceiling-mounted semi-cylindrical model containing a single wrap-around fin (WAF) was tested in the AFIT Mach 2.9 test facility. Flow visualization using oil-flow streaklines, schlieren images and shadowgraph photography revealed a  $\lambda$ -shock at the fin-body juncture and the development of an asymmetric bow-shock about the fin. Quantitative measurements were taken with a  $10^\circ$  cone-static pressure probe, a Pitot pressure probe and two cross-wire hot-film probes (u-v and u-w components, respectively). Measurements were made at cutting-planes from the inlet of the test section to aft of the model, with emphasis placed in the vicinity of the WAF. Results include cutting-plane profiles and contours of mean and turbulent fluctuations of the primitive and conserved flow variables. It was found that the incompressible turbulent fluctuating quantities are equally as descriptive of the flow structure in the fin's vicinity as the compressible turbulence fluctuations. The asymmetric bow-shock was found to be an inviscid phenomenon which was stronger on the concave side than the convex side and of diminishing strength at the tip with no bleeding effects over the tip.

Wrap-Around Fins, Supersonic, Wind Tunnel, Turbulence, Hot-Wire Anemometry

103

UNCLASSIFIED

UNCLASSIFIED

UNCLASSIFIED

UL